

Dopant Contrast Imaging of InP Using Scanning Electron Microscopy

(走査電子顕微鏡を用いた InP の
ドーパント二次元分布観察)

February 2015

Daisuke Tsurumi

(鶴見 大輔)

Abstract

In modern society, compound semiconductor devices play important roles in high-speed large-capacity communication systems, energy-saving technology, etc. During the manufacture of such devices, control of the two-dimensional (2D) dopant profile is critically important as it significantly affects device performance. However, an effective dopant profiling technique has not been established for industrial use.

In this study, we focused on a dopant profiling technique using scanning electron microscopy (SEM). SEM is the most attractive method that can meet industrial demand for rapid data measurement and high spatial resolution. However, some problems with sensitivity, reproducibility, and image interpretation exist. Thus, the purpose of this thesis is to solve these problems and establish a practical profiling technique for the compound semiconductor device industry.

The first problem, insensitivity, is due to ion milling during sample preparation. In this study, we confirmed that the insensitivity was caused by the generated amorphous layer. Then, highly sensitive dopant profiling was demonstrated for a sample prepared using low-energy ion milling, which generates a thin amorphous layer. The second issue, poor reproducibility, was observed during the SEM imaging process. We determined that the electron irradiation induced positive charging that led to the reduction of the low-energy secondary electron (SE) emission. In order to remove this effect, high-pass SE energy-filtered imaging was applied and highly reproducible dopant profiling was achieved. The third problem encountered with SEM, contrast interpretation, was particularly significant for devices with a heterojunction, which affects the SEM contrast because of the potential variation. We determined the influence of the heterojunction on the contrast using potential calculations, and clearly determined the dependence of the SEM contrast on dopant diffusion length. Hence, an accurate contrast interpretation method across the interface was established.

Thus, the three major problems affecting the 2D dopant profiling technique using SEM have been solved. The successfully established profiling technique is expected to be practically used, and will make a significant contribution to the compound semiconductor device industry.

Acknowledgements

My first and most earnest acknowledgement must go to my advisor, Prof. Yoshikazu Homma, for his kindly support, advice, and encouragement. Without his helpful support, this thesis would not have been possible.

I am deeply grateful to my advisory committee, Prof. Kazuyuki Watanabe, Prof. Takashi Meguro, Prof. Xinwei Zhao, and Prof. Yasuyuki Nagashima. The time taken by the committee members and their suggestions to improve the thesis are all very much appreciated.

I would like to thank Dr. Akira Yamaguchi, Director of the Analysis Technology Research Center; Mr. Masayuki Nishimura, Director of the R&D General Planning Division; Mr. Mitsutaka Nishie, Fellow, Mr. Kotaro Hamada, Senior Manager, and Mr. Shinji Matsukawa, Senior Manager, at Sumitomo Electric Industries, Ltd.; and Akira Urano in the Department of the New Energy and Industrial Technology Development Organization (NEDO), for providing me with the opportunity to conduct this research.

I would like to express my gratitude to Dr. Yasuo Namikawa, Senior Manager; Dr. Yoshihiro Saito, Senior Manager; Mr. Kenichiro Takahashi, Senior Manager; Mr. Takumi Yonemura; Mr. Yoshihiro Tsukuda; and Mr. Tomohiro Doi at Sumitomo Electric Industries, Ltd., for their insightful comments, suggestions, and warm encouragement.

I wish to thank Mr. Yuji Kawasaki and Mr. Koichi Sasaki, Team Leader, for their generous technical assistance.

Special thanks is also due to Dr. Yasuo Shimizu, Assistant Professor at Tohoku University, for his constructive comments and suggestions regarding improvements to this thesis.

I would like to thank Dr. Kentaro Okamoto at Sumitomo Electric Industries, Ltd., for introducing me to the Mendeley reference manager software at Toriken of Commercial street in Suzhou, China. This software dramatically improved the efficiency of the work presented in this thesis.

I am also indebted to Mr. Yuhei Nakajima, Mr. Masateru Shibata, and Mr. Toshiaki Suzuki at JEOL Ltd., for their experiments and fruitful discussion regarding the Ar⁺ ion milling using the Cryo Ion Slicer (IB-09060CIS).

I would also like to thank Mr. Shuichi Takeuchi of Hitachi High-Technologies Corporation for discussion of the SEM observation technique and interpretation using S-4800, in particular regarding energy-filtered imaging.

I would like to express the deepest appreciation to Dr. Susumu Nagayama at the Nano Science Corporation for his helpful advice regarding SIMS measurement and interpretation.

I would like to offer special thanks to Prof. Takashi Sekiguchi at the University of Tsukuba and the National Institute for Materials Science (NIMS), and Dr. Kazuhiro Kumagai at Advanced Industrial Science and Technology (AIST), for their insightful comments and suggestions regarding the dopant contrast mechanism.

My final, and most heartfelt, acknowledgment must go to my family. I am deeply grateful to parents, Hajime and Etsuko, and my sisters, Yuko and Hiroko, for their continuous support and warm encouragement. I wish to express my love and gratitude to my wife, Erika, and children, Ryotaro and Tomoka, for their unconditional support and heartwarming encouragement.

Contents

1. Introduction	1
1.1 Role of compound semiconductor devices in modern society	1
1.2 Role of and problems in compound semiconductor device analysis technology.....	4
1.3 2D dopant profiling methods for compound semiconductors	7
1.4 Current status of and problems in 2D dopant profiling using SEM.....	9
1.5 Purpose	11
1.6 Thesis outline	12
1.7 References.....	13
2. Experimental Details	22
2.1 Sample description.....	22
2.2 Sample preparation.....	24
2.2.1 Manual cleavage	24
2.2.2 Ion milling.....	25
2.3 Sample fixation for SEM observation	27
2.4 SEM observation	28
2.4.1 SEM observation mechanism.....	29
2.4.2 Dopant contrast mechanism in SEM.....	32
2.4.3 Employed SEM and SE energy-filtering method	36
2.4.4 SE energy distribution observation method.....	38
2.5 Dopant contrast quantification method	41
2.6 Summary	42

2.7 References.....	42
3. Development of Sample Preparation Technique	47
3.1 Introduction.....	47
3.1.1 Significance of 2D dopant profiling of surfaces prepared through ion milling	48
3.1.2 Problems in 2D dopant profiling of ion-milled surfaces using SEM	49
3.2 Purpose	50
3.3 Experimental Method	51
3.3.1 Sample.....	51
3.3.2 Sample preparation method.....	51
3.3.3 SEM observation conditions.....	52
3.4 Surface roughness results and discussion	53
3.5 Dopant contrast results and discussion	53
3.5.1 Results (SEM acceleration voltage: 1 kV).....	55
3.5.2 Calculation of amorphous thickness.....	57
3.5.3 Relationship between dopant contrast and amorphous layer thickness	58
3.5.4 Contrast dependence on acceleration voltage	60
3.6 Discussion of dopant contrast mechanism.....	62
3.7 Conclusions.....	62
3.8 References.....	64
4. Development of Observation Technique.....	68
4.1 Introduction.....	68
4.2 Purpose	70
4.3 Method.....	70
4.3.1 Samples	71

4.3.2 Observation method	71
4.4 Energy-filtering results and discussion	73
4.4.1 Observation of SE energy distribution	73
4.4.2 Discussion of electron-beam-irradiation-induced SE intensity reduction mechanism	76
4.4.3 Energy-filtering effect on electron beam irradiation	83
4.5 Application of energy-filtered imaging to reduce effects of electron beam irradiation.....	85
4.6 Effect of reverse-bias voltage application	89
4.6.1 Imaging demands at high magnification.....	89
4.6.2 Image quality improvement method.....	90
4.6.3 Reverse-bias voltage application results	92
4.6.4 Discussion using SE energy distribution observation	96
4.7 Discussion of dopant contrast mechanism.....	98
4.8 Conclusions.....	98
4.9 References.....	100
5. Establishment of Contrast Interpretation Method at Heterojunction Interfaces	103
5.1 Introduction.....	103
5.2 Purpose	105
5.3 Experimental method	105
5.3.1 Sample structure and SEM observation conditions.....	105
5.3.2 SIMS measurement method	106
5.3.3 Potential calculation method	106
5.4 Results and discussion.....	106
5.4.1 SEM observation and SIMS measurement	107

5.4.2 SEM electrostatic potential sensitivity.....	110
5.4.3 SEM contrast dependence on Zn diffusion length across the interface	113
5.5 Discussion of dopant contrast mechanism	116
5.6 Conclusions.....	117
5.7 References.....	118
6. Conclusions	120
6.1 Conclusions.....	120
6.2 Remaining issues	124
List of symbols and abbreviations	125
Publications	127

Chapter 1

Introduction

This chapter begins with a description of the role of compound semiconductor devices in modern society. Then, the importance of analysis technology in relation to device manufacturing is described, focusing particularly on the significance of the dopant profiling technique. Subsequently, it is shown that the dopant profiling method using SEM has advantages over other profiling techniques in regards to compound semiconductor devices. Finally, the existing problems with the SEM profiling technique are examined, in order to clarify the purpose of the research presented in this thesis.

1.1 Role of compound semiconductor devices in modern society

In the last half-century, improvements in semiconductor device technology have contributed significantly to the development of modern society. These devices have been used in various fields, such as in

information-communication systems, manufacturing equipment, consumer electronics, automobiles, and medical instruments. The development of the such device technology has dramatically changed both social structure and human lifestyles. Recently, the modern world has begun to move toward the realization of an interconnected network and energy-saving society. These changes have generated a stronger demand for advanced semiconductor devices with higher speed, power, luminance efficiency, etc.

Some devices that meet the above requirements are composed of compound semiconductors. Because compound semiconductors have the physical properties of higher electron mobility, higher breakdown voltage, and direct transition devices using these components have higher speed, power, and luminance efficiency than silicon-based devices. Therefore, compound semiconductor devices are used in a wide range of fields, as shown in Fig. 1-1.

Optical devices such as laser diodes (LD) and photo diodes (PD) are used for high-speed and large-capacity communication systems. Light emitting diodes (LED) are used as backlights for liquid crystal displays, office lights, etc., in order to conserve energy. Further, electronic devices composed of high-electron-mobility transistors are used as power amplifiers in mobile base stations, mobile phones and wireless communication equipment, on-vehicle radar, etc., so as to facilitate large-capacity wireless communication among heterogeneous terminals. Finally, compound-semiconductor-based power devices are gradually becoming used as inverters in air conditioners, in motor controls for railroad vehicles, etc.; also to conserve energy.

Thus, compound semiconductor devices are becoming increasingly important in modern society, and further development of compound semiconductor device fields is desirable. The five-year compound annual growth rate (CAGR) of the semiconductor and compound semiconductor market shown in Table 1-1 provides quantitative evidence of this [1–4].

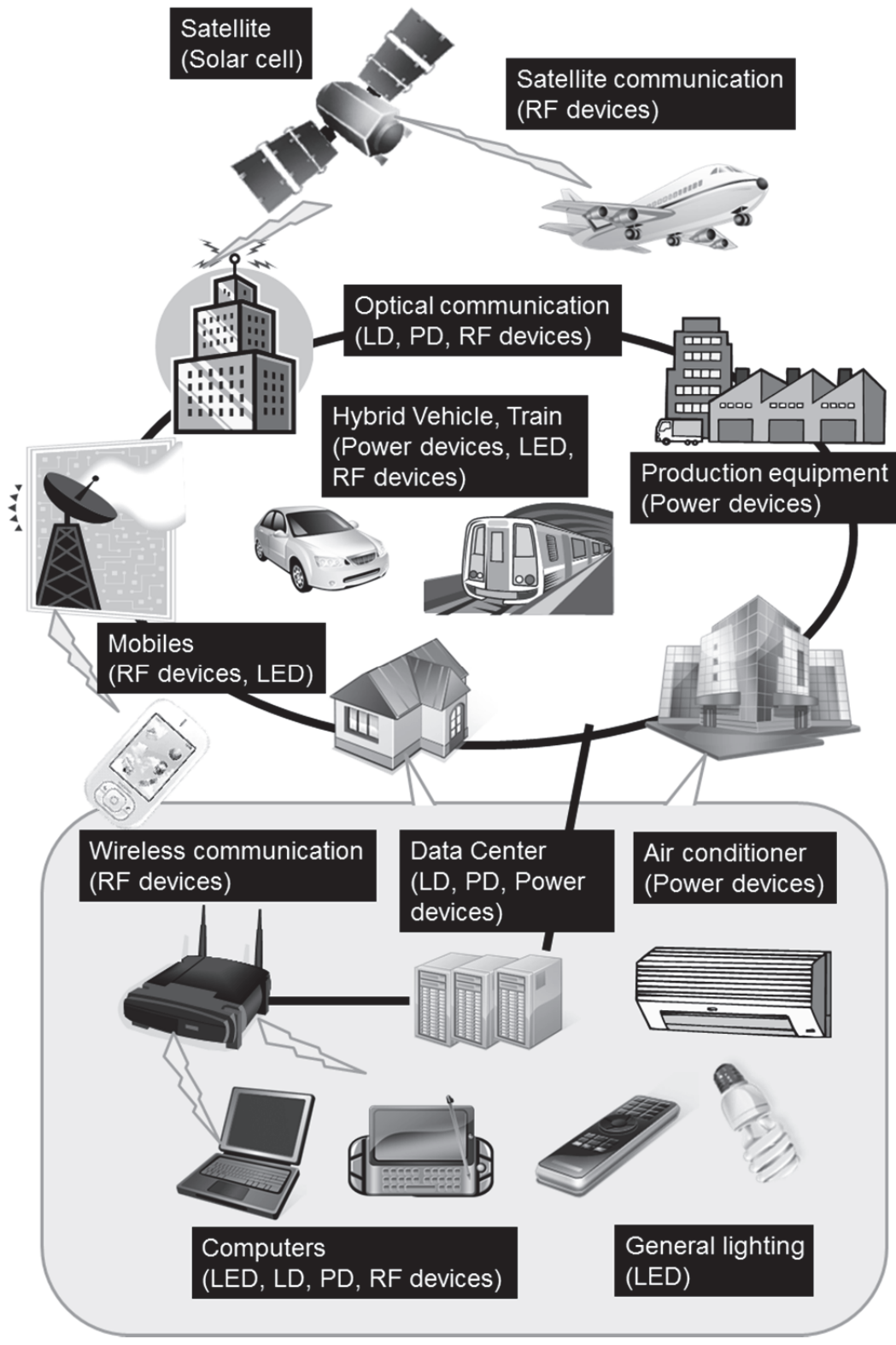


Fig. 1-1. Compound semiconductor device applications.

Table 1-1. Five-year CAGR of semiconductors and the compound semiconductor market [1–4].

Year	2008–2012	2013–2017 (forecast)
Compound semiconductor market	11.1 %	11.9 %
Semiconductor market	2.5 %	6.7 %

From 2008 to 2012, the CAGR of the semiconductor market was only 2.5%, because of the recession triggered by the subprime mortgage crisis. In contrast, the compound semiconductor market was not affected by the recession and achieved a 4–5 times higher growth rate (11.1 %/year). Furthermore, the CAGR from 2013–2017 is expected to reach 11.9 %, and the global sales from compound semiconductor components are expected to increase to almost \$47.5 billion [2] In contrast, the semiconductor market is expected to grow by 6.7 %. As indicated by the CAGR, the compound semiconductor devices are expected to exhibit strong growth in the overall semiconductor market. This is because compound semiconductor devices have higher performance than silicon-based devices as regards speed, power, and luminance efficiency and therefore meet the demands of the modern society.

Thus, higher-performance and lower-cost devices incorporating compound semiconductors are strongly required in order to meet industry and social demands.

1.2 Role of and problems in compound semiconductor device analysis technology

In order to improve the performance of compound semiconductor devices, progress in many technological fields is essential. These areas are shown in Table 1-2 [5] and include crystal growth, device manufacturing, assembly and packaging, and process and device simulation technology.

Another of these areas is analysis technology, as this form of research is necessary for the process characterization, failure analysis, etc., of compound semiconductor devices. The major characterization methods for compound semiconductor devices are shown in Table 1-3.

Table 1-2. Technological fields involved in compound-semiconductor-device development [5].

No	Field
1	Crystal growth technology
2	Device manufacturing technology
3	Assembly and packaging technology
4	Monolithic microwave integrated circuit and integration technology
5	Test and analysis technology
6	Reliability characterization technology
7	Process and device simulation technology

As shown in Table 1-3, over twenty analytical methods are available. The first step of a typical major analysis procedure is (A) the identification of the failure location [6–9]. Then, the cross-section of the failure location is prepared using (B) sample preparation methods [10,11]. Next, (C) configuration analysis [12–15], (D) composition analysis [16,17], (F) two dimensional (2D) dopant profiling [18–20], and (H) stress measurement methods [21] are used. All of the methods, including (E) surface composition analysis [22] and (G) chemical states analysis [23–25], are typically used for process characterization.

Of these methods, one of the most important techniques that has not yet attained the level required for industrial use is (F) 2D dopant profiling.

Table 1-3. Typical characterization methods for compound semiconductor devices.

Purpose		Method
(A) Identification of failure location		1. X-CT (X-ray computed tomography)
		2. Photo/thermal emission microscopy
		3. IR-OBIRCH (Infrared-optical beam induced resistance change)
(B) Sample preparation method		4. Mechanical polishing
		5. Wet etching
		6. IP (Ion polishing)
		7. FIB (Focused ion beam)
(C) Configuration analysis		8. SEM (Scanning electron microscopy)
		9. AFM (Atomic force microscopy)
		10. STEM (Scanning transmission electron microscopy)
(D) Composition analysis		11. EDX (Energy dispersive x-ray spectrometer)
		12. EPMA (Electron probe microanalyser)
(E) Surface composition analysis		13. TRXF (Total reflection X-ray fluorescence)
		14. AES (Auger electron spectroscopy)
		15. XPS (X-ray photoelectron spectroscopy)
		16. ToF-SIMS (Time-of-flight secondary ion mass spectrometry)
(F) Dopant profiling	1D	17. D-SIMS (Dynamic secondary ion mass spectrometry)
	2D	8. SEM
		18. CL (Cathode luminescence), PL (Photo luminescence)
		19. SSRM (Scanning spread resistance microscopy)
		20. Electron holography
(G) Chemical states analysis		21. FT-IR (Fourier transform Infrared spectroscopy)
		22. EELS (Electron energy loss spectroscopy)
		15. XPS
		23. HAXPES (Hard X-ray photoelectron spectroscopy)
(H) Stress measurement		24. XRD (X-ray diffraction)
		25. Raman spectroscopy
		26. CBED (Convergent beam electron diffraction)
		18. CL, PL

1.3 2D dopant profiling methods for compound semiconductors

Dopants are impurities that are intentionally introduced into an intrinsic semiconductor for the purpose of controlling its electrical properties. Dopants generate carriers (electrons or holes) and electric fields inside the devices. Therefore, the dopant concentration and distribution strongly affect the device properties and, thus, precise dopant control is required. Clearly, a 2D dopant profiling method with high spatial resolution and sensitivity is essential for device development and production.

As an example, Fig. 1-2 is a schematic drawing of the indium phosphide (InP) LD cross-section. It is composed of an n-InP (1×10^{18} Si atoms cm^{-3}) clad layer, a GaInAsP active layer, and a p-InP (1×10^{18} Zn atoms cm^{-3}) clad layer [26–28]. This structure enables an increase of stimulated emission efficiency through high-efficiency injection of electrons and holes into an active layer. In addition, this structure makes it possible to confine photons generated by radiative recombination inside the active layer. To achieve high emission efficiency and reliability, precise dopant distribution in the compound semiconductor devices is important, and a 2D dopant profiling method with high spatial resolution and sensitivity is essential in order to control this distribution. Furthermore, semiconductor fabrication plants require data measurement speed, reproducibility, and accurate interpretation of measurement results.

Thus, a large number of dopant profiling techniques have been developed, and the major methods are shown in Table 1-4. Of these methods, the most attractive technique is SEM, as this analysis tool can meet the industrial demands for rapid data measurement and quick sample preparation. In most cases, the SEM spatial resolution and sensitivity is sufficiently high for industrial use. However, SEM application has encountered some problems and has not yet reached the level necessary for industrial use. Therefore, in this study, the remaining problems faced by 2D dopant profiling using SEM are examined.

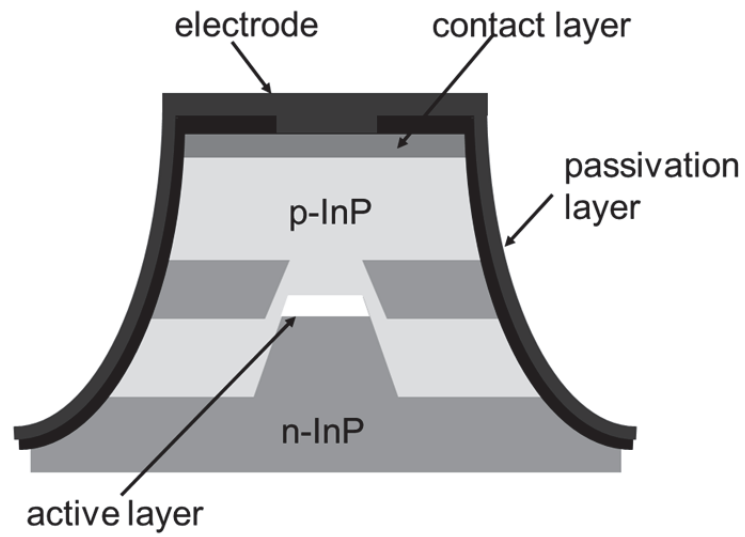


Fig. 1-2. Schematic drawing of LD cross-section for optical communication.

Table 1-4. Major 2D dopant profiling methods.

Method	SEM [18]	CL [29]	SSRM [19]	Electron Holography [20]
Spatial resolution (nm)	10–	100–	1–	1–
Sensitivity (atoms/cm ³)	10 ¹⁶ –	10 ¹⁴ –	10 ¹⁵ –	10 ¹⁷ –
Data measurement speed	0.5 h	3 h	1 h	1 week
Reproducibility	Medium	Low	Extremely low	Medium
Interpretation of results	Medium	Medium	Medium	Difficult

1.4 Current status of and problems in 2D dopant profiling using SEM

Although the idea of SEM was originally conceived by M. Knoll in 1935 [30] and M. von Ardenne for the transmission mode in 1938 [31], [32], the first commercial SEM based on the work of C. W. Oatley and coworkers at Cambridge University started in 1965. Since that time, SEM has grown to become an established surface imaging technique. However, dopant profiling using SEM was only minimally reported until the 1990's. This was primarily because of electron gun and detector properties. In the 1980's, Schottky-emission electron guns and field-emission guns became common, enabling low-voltage primary electron beam imaging at, for example, 1 or 2 kV. In addition, through-the-lens (TTL) detectors became widely used and dramatically improved the detection sensitivity for low-energy secondary electron (SE) emissions. As the so-called dopant contrast is increased by low-voltage primary electron beams and the ability to detect low-energy SE emission, developments in electron guns and detection systems allowed substantial progress to be made in dopant profiling from the 1990's onwards [18,33–57].

In 1995, Perovic *et al.* demonstrated that the contrast in the observed SE intensity was not only dependent on the doping type, but was also sensitive to the doping concentration levels [33]. This report strongly promoted research on the topic of dopant contrast. In 1998, linear dependence between the observed contrast and the dopant concentration logarithm in p-type silicon was reported [35], and this was confirmed for dopant concentrations ranging from 10^{16} – 10^{20} atoms/cm³ by Elliott *et al.* [38]. In addition, Venables *et al.* reported that the spatial resolution of this method was 19 nm [35], and Kazemian *et al.* indicated that a resolution of <6 nm could be expected for favorable specimens [43]. Furthermore, in 2006, it was demonstrated by Kazemian *et al.* that dopant contrast could be observed even from focused ion beam (FIB)-prepared silicon p-n junctions [49].

Thus, dopant profiling using SEM is not only used for rapid data measurements, but is also sufficiently sensitive for industrial use. In addition, the spatial resolution is also sufficiently high. Therefore, it has

potential for practical use. However, a review of the previous studies on this topic reveals three critical problems limiting the efficacy of the 2D dopant profiling of compound semiconductor devices.

The first problem is low sensitivity, which means a decrease in dopant contrast, and is due to sample preparation using ion milling. The dopant contrast value taken from cross-sections of silicon samples prepared using ion milling, which is a very popular method, has been found to be only half that of the cleaved surface [48]. In addition, compound semiconductor materials tend to be damaged more easily than silicon. For example, amorphous layer thickness generated by FIB milling is 21 nm for silicon [48] but 33 nm for InP [58]. Furthermore, the milling also generates surface roughness in compound semiconductors [59–61]. Thus, ion milling leads to a significant decrease in contrast and an increase in surface roughness, and results in insensitivity to low dopant concentrations. This makes it impossible to achieve sensitive dopant profiling of compound semiconductor devices. For advanced 2D dopant profiling, it is therefore essential to determine the dopant contrast mechanism so that the contrast from ion milled surfaces can be increased to the same level as that provided by cleaved surfaces.

The second problem is poor reproducibility. The dopant contrast decreases and disappears as a result of electron beam irradiation during SEM observation [43], leading to reproducibility issues. This is a common problem found in silicon and compound semiconductor devices. Without investigating the mechanism and overcoming this obstacle, SEM cannot be used in semiconductor fabrication plants.

The third problem is the interpretation of the obtained SEM images. The majority of compound semiconductor devices consist of more than two semiconductor materials. This is a remarkable feature that produces powerful devices and is unique to compound semiconductors. Thus, it is not found in silicon semiconductors [62]. In contrast, this feature makes 2D dopant profiling quite difficult. The interpretation of SEM contrast in III-V semiconductor devices, particularly at heterojunction interfaces, is more complicated than that for silicon homojunction devices. This is because SEM contrast arises not only from the dopant concentration, but also from the potential variation due to the heterojunction interfaces [42]. For accurate dopant profiling of compound semiconductor devices, it is essential to take an

influence of the heterojunction on SEM contrast into account, and to clearly determine the dependence of the SEM contrast on the dopant distribution across the interface.

Thus, 2D dopant profiling for compound semiconductor devices using SEM has three critical problems. Clearly, for compound semiconductor research and development (R&D) and production, solving these three problems is essential so that a practical 2D dopant profiling technique can be established.

In addition, a fundamental problem remains in that the dopant contrast mechanism itself is still unclear, although a number of models have been suggested [18,33,36,45,51–53]. In order to dramatically improve this dopant profiling technique in regard to spatial resolution, sensitivity, etc., the mechanism must be clarified.

1.5 Purpose

Thus, the purpose of this study is to address the abovementioned three major problems related to 2D dopant profiling using SEM, and to establish the profiling technique that achieves the requirements for compound semiconductor R&D and production. In addition, the dopant contrast mechanism is discussed using the data obtained through these studies.

The materials used in this research are InP-based. This is because InP is the most damage-labile candidate, and it is also difficult to observe dopant contrast in this substance because of the middle band gap, as shown in Table 1-5. As InP is one of the most difficult compound semiconductor materials to observe with the 2D dopant profiling using SEM, establishing the dopant profiling technique using InP-based materials indicates that this method can be widely applied to other compound semiconductor materials (GaAs, SiC, GaN, etc.).

Table 1-5. Silicon and typical compound semiconductor features.

Material	Si	InP	GaAs	SiC	GaN
Damage thickness due to ion milling (nm)	21 [48]	33 [58]	22 [58]	(-)	~30 [63]
Band gap (eV) (contrast)	1.12 (low)	1.34 (low)	1.43 (low)	3.26 (high)	3.39 (high)

1.6 Thesis outline

This section gives an outline of Chapters 2–6. Chapter 2 contains a description of the samples and instruments used in this study. The details of the 2D dopant profiling technique using SEM are described from a theoretical point of view, focusing on: the fundamental principles of SEM, the dopant contrast mechanism, the SE energy-filtering method, an SE energy distribution observation technique, and the dopant contrast quantification method.

Chapter 3 describes the development of the InP sample preparation technique for sensitive observation, which is essential for device analysis. It is indicated that the insensitivity is caused by the amorphous layer generated by ion milling. Then, highly sensitive 2D dopant profiling is demonstrated using SE imaging on an InP sample, which is prepared using low-energy Ar⁺ ion milling. In addition, the dopant contrast mechanism is discussed using the obtained data, and it is implied that the dopant contrast primarily arises from the local electric field, which is the built-in potential.

Chapter 4 presents the development of the observation technique for reproducible observation. It is revealed that the electron irradiation induces a positive charge and reduces low-energy SE emission, which leads to poor reproducibility. It is shown that this unfavorable irradiation effect can be substantially reduced through high-pass energy-filtered imaging, and a highly reproducible contrast is then achieved during continuous SEM

observation. In addition, the contrast is clearly observed even under high-magnification conditions, where the irradiation effect is typically increased, by simultaneously applying SE energy filtering and a reverse-bias voltage. Finally, effects of surface states on the dopant contrast are discussed.

Chapter 5 discusses the SEM contrast interpretation method across the heterojunction using an InP/InGaAs heterostructure sample. Based on SEM observations and potential calculations, the dependence on the dopant distribution across the interface is investigated, and it is then shown that SE imaging can be widely used for accurate 2D dopant profiling, even at heterojunctions. In addition, the reasons why dopant profiling using SEM is more insensitive to n-type than p-type semiconductors are discussed and the influence of carrier concentration on dopant contrast is suggested as a possible explanation.

Chapter 6 summarizes the results and concludes this study. Finally, any remaining issues are addressed.

1.7 References

- [1] “Global Market for Compound Semiconductors Worth \$33.7 Billion by 2012.” [Online]. Available:
[http://www.bccresearch.com/pressroom/smc/global-market-compound-semiconductors-worth-\\$33.7-billion-2012](http://www.bccresearch.com/pressroom/smc/global-market-compound-semiconductors-worth-$33.7-billion-2012). [Accessed: 03-Mar-2014].
- [2] “Global Markets and Technologies for Compound Semiconductors - SMC032D.” [Online]. Available:
<http://www.bccresearch.com/market-research/semiconductor-manufacturing/compound-semiconductors-technologies-global-markets-smc032d.html>. [Accessed: 03-Mar-2014].
- [3] “2012: A Year in Review — Semiconductor Equipment and Materials Market and Outlook | SEMI.ORG.” [Online]. Available:
<http://www.semi.org/en/node/45201>. [Accessed: 03-Mar-2014].

- [4] “Global Semiconductor Market Outlook to 2017 - market research report.” [Online]. Available: <http://www.reportlinker.com/p01360863-summary/Global-Semiconductor-Market-Outlook-to.html>. [Accessed: 03-Mar-2014].
- [5] *Compound Semiconductor Technology Outlook*. Tokyo: Electronic Journal, Inc., 2013.
- [6] E. Inuzuka and H. Suzuki, “Emission microscopy in semiconductor failure,” in *Instrumentation and Measurement Technology Conference, 1994. IMTC/94. Conference Proceedings. 10th Anniversary. Advanced Technologies in I & M., 1994 IEEE*, pp. 1492–1496, 1994.
- [7] N. Thierry-Jebali, J. Hassan, M. Lazar, D. Planson, E. Bano, A. Henry, E. Janzén, and P. Brosselard, “Observation of the generation of stacking faults and active degradation measurements on off-axis and on-axis 4H-SiC PiN diodes,” *Appl. Phys. Lett.*, vol. 101, no. 22, 222111, 2012.
- [8] K. Nikawa, C. Matsumoto, and S. Inoue, “Novel Method for Defect Detection in Al Stripes by Means of Laser Beam Heating and Detection of Changes in Electrical Resistance,” *Jpn. J. Appl. Phys.*, vol. 34, no. Part 1, No. 5A, pp. 2260–2265, 1995.
- [9] B. Lambert, N. Labat, D. Carisetti, S. Karboyan, J. G. Tartarin, J. Thorpe, L. Brunel, A. Curutchet, N. Malbert, E. Latu-Romain, and M. Mermoux, “Evidence of relationship between mechanical stress and leakage current in AlGaN/GaN transistor after storage test,” *Microelectron. Reliab.*, vol. 52, no. 9–10, pp. 2184–2187, 2012.
- [10] H. Takahashi, A. Sato, M. Takakura, N. Mori, J. Boerder, W. Knoll, and J. Critchell, “A New Method of Surface Preparation for High Spatial Resolution EPMA/SEM with an Argon Ion Beam,” *Microchim. Acta*, vol. 155, no. 1–2, pp. 295–300, 2006.
- [11] L. A. Giannuzzi and F. A. Stevie, Eds., *Introduction to Focused Ion Beams - Instrumentation, Theory, Techniques and Practice*. New York: Springer, 2005.

- [12] H. Seiler, "Secondary electron emission in the scanning electron microscope," *J. Appl. Phys.*, vol. 54, no. 11, pp. R1–R18, 1983.
- [13] L. Reimer, *Scanning Electron Microscopy: Physics of Image Formation and Microanalysis*. Verlag Berlin Heidelberg New York: Springer, 1998.
- [14] K. Ishizuka, "Prospects of atomic resolution imaging with an aberration-corrected STEM," *J. Electron Microsc. (Tokyo)*, vol. 50, no. 4, pp. 291–305, 2001.
- [15] A. Lotnyk, D. Poppitz, J. W. Gerlach, and B. Rauschenbach, "Direct imaging of light elements by annular dark-field aberration-corrected scanning transmission electron microscopy," *Appl. Phys. Lett.*, vol. 104, no. 7, 071908, 2014.
- [16] A. J. D'Alfonso, B. Freitag, D. Klenov, and L. J. Allen, "Atomic-resolution chemical mapping using energy-dispersive x-ray spectroscopy," *Phys. Rev. B*, vol. 81, no. 10, 100101, 2010.
- [17] L. J. Allen, A. J. D'Alfonso, B. Freitag, and D. O. Klenov, "Chemical mapping at atomic resolution using energy-dispersive x-ray spectroscopy," *MRS Bull.*, vol. 37, no. 01, pp. 47–52, 2012.
- [18] C. Sealy, M. Castell, and P. Wilshaw, "Mechanism for secondary electron dopant contrast in the SEM," *J. Electron Microsc. (Tokyo)*, vol. 49, no. 2, pp. 311–321, 2000.
- [19] P. De Wolf, M. Geva, T. Hantschel, W. Vandervorst, and R. B. Bylisma, "Two-dimensional carrier profiling of InP structures using scanning spreading resistance microscopy," *Appl. Phys. Lett.*, vol. 73, no. 15, pp. 2155–2157, 1998.
- [20] H. Sasaki, K. Yamamoto, T. Hirayama, S. Ootomo, T. Matsuda, F. Iwase, R. Nakasaki, and H. Ishii, "Mapping of dopant concentration in a GaAs semiconductor by off-axis phase-shifting electron holography," *Appl. Phys. Lett.*, vol. 89, no. 24, 244101, 2006.

- [21] L. Zhu, C. Georgi, M. Hecker, J. Rinderknecht, A. Mai, Y. Ritz, and E. Zschech, “Nano-Raman spectroscopy with metallized atomic force microscopy tips on strained silicon structures,” *J. Appl. Phys.*, vol. 101, no. 10, 104305, 2007.
- [22] R. P. Donovan, *Contamination-Free Manufacturing for Semiconductors and Other Precision Products*. New York: CRC Press, 2001.
- [23] C. Caspers, M. Müller, A. X. Gray, A. M. Kaiser, A. Gloskovskii, C. S. Fadley, W. Drube, and C. M. Schneider, “Chemical stability of the magnetic oxide EuO directly on silicon observed by hard x-ray photoemission spectroscopy,” *Phys. Rev. B*, vol. 84, no. 20, 205217, 2011.
- [24] T. Narita, D. Kikuta, N. Takahashi, K. Kataoka, Y. Kimoto, T. Uesugi, T. Kachi, and M. Sugimoto, “Study of etching-induced damage in GaN by hard X-ray photoelectron spectroscopy,” *Phys. status solidi*, vol. 208, no. 7, pp. 1541–1544, 2011.
- [25] M. Wimmer, D. Gerlach, R. G. Wilks, S. Scherf, R. Félix, C. Lupulescu, F. Ruske, G. Schondelmaier, K. Lips, J. Hüpkes, M. Gorgoi, W. Eberhardt, B. Rech, and M. Bär, “Chemical interaction at the buried silicon/zinc oxide thin-film solar cell interface as revealed by hard X-ray photoelectron spectroscopy,” *J. Electron Spectros. Relat. Phenomena*, vol. 190, pp. 309–313, 2013.
- [26] O. Ueda, *Reliability and Degradation of III-V Optical Devices*. London/Boston: Artech House Publishers, 1996.
- [27] R. Hull, F. A. Stevie, and D. Bahnck, “Observation of strong contrast from doping variations in transmission electron microscopy of InP-based semiconductor laser diodes,” *Appl. Phys. Lett.*, vol. 66, pp. 341–343, 1995.

- [28] H. Ichikawa, K. Sasaki, K. Hamada, and A. Yamaguchi, "Electroluminescence Analysis by Tilt Polish Technique of InP-Based Semiconductor Lasers," *Jpn. J. Appl. Phys.*, vol. 49, no. 3, 038005, 2010.
- [29] M. Yoshikawa, K. Iwagami, and H. Ishida, "Characterization of carrier concentration and stress in GaAs metal-semiconductor field-effect transistor by cathodoluminescence spectroscopy Characterization of carrier concentration and stress in GaAs metal-semiconductor field-effect transistor by cathod," *J. Appl. Phys.*, vol. 84, no. 3, pp. 1693-1696, 1998.
- [30] M. Knoll, "Aufladepotential und sekundäremission elektronenbestrahlter körper," *Z. tech. Phys.*, vol. 16, pp. 467-475, 1935.
- [31] M. von Ardenne, "Das Elektronen-Rastermikroskop. Praktische Ausführung.," *Z. tech. Phys.*, vol. 19, pp. 407-416, 1938.
- [32] M. von Ardenne, "Das Elektronen-Rastermikroskop. Theoretische Grundlagen.," *Z. Phys.*, vol. 109, no. 9-10, pp. 553-572, 1938.
- [33] D. D. Perovic, M. R. Castell, A. Howie, C. Lavoie, T. Tiedje, and J. S. W. Cole, "Field-emission SEM imaging of compositional and doping layer semiconductor superlattices," *Ultramicroscopy*, vol. 58, no. 1, pp. 104-113, 1995.
- [34] R. Turan and D. D. Perovic, "Mapping electrically active dopant profiles by field-emission scanning electron microscopy," *Appl. Phys. Lett.*, vol. 69, no. 11, pp. 1593-1595, 1996.
- [35] D. Venables, H. Jain, and D. C. Collins, "Secondary electron imaging as a two-dimensional dopant profiling technique: Review and update," *J. Vac. Sci. Technol. B*, vol. 16, pp. 362-366, 1998.
- [36] M. M. El-Gomati and T. C. R. Wells, "Very-low-energy electron microscopy of doped semiconductors," *Appl. Phys. Lett.*, vol. 79, no. 18, pp. 2931-2933, 2001.

- [37] P. G. Merli, F. Corticelli, and V. Morandi, “Images of dopant profiles in low-energy scanning transmission electron microscopy,” *Appl. Phys. Lett.*, vol. 81, no. 24, pp. 4535–4537, 2002.
- [38] S. L. Elliott, R. F. Broom, and C. J. Humphreys, “Dopant profiling with the scanning electron microscope—A study of Si,” *J. Appl. Phys.*, vol. 91, no. 11, pp. 9116–9122, 2002.
- [39] C. Schönjahn, C. J. Humphreys, and M. Glick, “Energy-filtered imaging in a field-emission scanning electron microscope for dopant mapping in semiconductors,” *J. Appl. Phys.*, vol. 92, no. 12, pp. 7667–7671, 2002.
- [40] M. R. Castell, D. a Muller, and P. M. Voyles, “Dopant mapping for the nanotechnology age,” *Nat. Mater.*, vol. 2, no. 3, pp. 129–131, 2003.
- [41] C. Schönjahn, R. F. Broom, C. J. Humphreys, A. Howie, and S. A. M. Mentink, “Optimizing and quantifying dopant mapping using a scanning electron microscope with a through-the-lens detector,” *Appl. Phys. Lett.*, vol. 83, no. 2, pp. 293–295, 2003.
- [42] B. Kaestner, C. Schönjahn, and C. J. Humphreys, “Mapping the potential within a nanoscale undoped GaAs region using a scanning electron microscope,” *Appl. Phys. Lett.*, vol. 84, no. 12, pp. 2109–2111, 2004.
- [43] P. Kazemian, C. Rodenburg, and C. J. Humphreys, “Effect of experimental parameters on doping contrast of Si p-n junctions in a FEG-SEM,” *Microelectron. Eng.*, vol. 73–74, pp. 948–953, 2004.
- [44] G. H. Jayakody, T. R. C. Wells, and M. M. El-Gomati, “Imaging of doped Si in low and very low voltage SEM: the contrast interpretation,” *J. Electron Spectros. Relat. Phenomena*, vol. 143, no. 2–3, pp. 233–239, 2005.

- [45] M. El-Gomati, F. Zaggout, H. Jayacody, S. Tear, and K. Wilson, "Why is it possible to detect doped regions of semiconductors in low voltage SEM: a review and update," *Surf. Interface Anal.*, vol. 37, no. 11, pp. 901–911, 2005.
- [46] B. L. Thiel and M. Toth, "Secondary electron contrast in low-vacuum/environmental scanning electron microscopy of dielectrics," *J. Appl. Phys.*, vol. 97, no. 5, 051101, 2005.
- [47] P. G. Merli, V. Morandi, G. Savini, M. Ferroni, and G. Sberveglieri, "Scanning electron microscopy of dopant distribution in semiconductors," *Appl. Phys. Lett.*, vol. 86, no. 10, 101916, 2005.
- [48] L. A. Giannuzzi, R. Geurts, and J. Ringnalda, "2 keV Ga⁺ FIB Milling for Reducing Amorphous Damage in Silicon," *Microsc. Microanal.*, vol. 11, no. S02, pp. 828–829, 2005.
- [49] P. Kazemian, A. C. Twitchett, C. J. Humphreys, and C. Rodenburg, "Site-specific dopant profiling in a scanning electron microscope using focused ion beam prepared specimens," *Appl. Phys. Lett.*, vol. 88, no. 21, 212110, 2006.
- [50] P. Kazemian, S. a. M. Mentink, C. Rodenburg, and C. J. Humphreys, "High resolution quantitative two-dimensional dopant mapping using energy-filtered secondary electron imaging," *J. Appl. Phys.*, vol. 100, no. 5, 054901, 2006.
- [51] Y. Chakk and D. Horvitz, "Contribution of dynamic charging effects into dopant contrast mechanisms in silicon," *J. Mater. Sci.*, vol. 41, no. 14, pp. 4554–4560, 2006.
- [52] C. G. H. Walker, F. Zaggout, and M. M. El-Gomati, "The role of oxygen in secondary electron contrast in doped semiconductors using low voltage scanning electron microscopy," *J. Appl. Phys.*, vol. 104, no. 12, 123713, 2008.

- [53] K. Kumagai, T. Sekiguchi, K. Fukuda, and T. Sasaki, "Secondary Electron Imaging of Monolayer Titania Nanosheets," *Appl. Phys. Express*, vol. 2, no. 10, 105504, 2009.
- [54] C. Rodenburg, M. A. E. Jepson, B. J. Inkson, E. Bosch, A. K. W. Chee, and C. J. Humphreys, "Energy filtered scanning electron microscopy: Applications to dopant contrast," *J. Phys. Conf. Ser.*, vol. 209, 012053, 2010.
- [55] D. Tsurumi, K. Hamada, and Y. Kawasaki, "Energy-filtered imaging in a scanning electron microscope for dopant contrast in InP.," *J. Electron Microsc. (Tokyo)*, vol. 59 Suppl 1, pp. S183–S187, 2010.
- [56] A. K. W. Chee, R. F. Broom, C. J. Humphreys, and E. G. T. Bosch, "A quantitative model for doping contrast in the scanning electron microscope using calculated potential distributions and Monte Carlo simulations," *J. Appl. Phys.*, vol. 109, no. 1, 013109, 2011.
- [57] S. Chung, V. Wheeler, R. Myers-Ward, L. O. Nyakiti, C. R. Eddy, D. K. Gaskill, M. Skowronski, and Y. N. Picard, "Secondary electron dopant contrast imaging of compound semiconductor junctions," *J. Appl. Phys.*, vol. 110, no. 1, 014902, 2011.
- [58] S. Rubanov and P. R. Munroe, "Damage in III – V Compounds during Focused Ion Beam Milling," *Microsc. Microanal.*, vol. 11, pp. 446–455, 2005.
- [59] O. Wada, "Ar ion-beam etching characteristics and damage production in InP," *J. Phys. D. Appl. Phys.*, vol. 17, no. 12, pp. 2429–2437, 1984.
- [60] J. Pearton, K. Chakrabarti, A. P. Perley, T. B. Laboratories, M. Hill, and K. S. Jones, "Ion milling damage in InP and GaAs," *J. Appl. Phys.*, vol. 68, no. T1a 20, pp. 2760–2768, 1990.
- [61] Y. Homma, "Formation mechanism of indium microcrystals on ion-bombarded InP surfaces," *J. Surf. Anal.*, vol. 3, no. 3, pp. 641–645, 1997.

- [62] H. Hayashi, “Development of Compound Semiconductor Devices — In Search of Immense Possibilities —,” *SEI Tech. Rev.*, vol. 72, pp. 4–16, 2011.
- [63] K. Tanabe, T. Matsuda, H. Sasaki, and F. Iwase, “TEM specimen preparation technique for III–V semiconductor devices by using a novel FIB-Ar ion milling method,” in *Microscopy of Semiconducting Materials: Proceedings of the 14th Conference, 2005*, vol. 107, pp. 417–422.

Chapter 2

Experimental Details

This chapter presents the sample structures, the sample preparation method, models that can explain dopant contrast imaging, the SEM observation method, and the evaluation method, all of which will be applied in Chapters 3–5.

2.1 Sample description

Three sample types shown in Fig. 2-1 were used in this study. In Chapters 3 and 4, two types of InP test structures, which were grown using metal-organic vapor phase epitaxy (MOVPE), are used. One sample, shown in Fig. 2-1 (a), consisted of a p-type layer (1×10^{18} Zn atoms cm^{-3}), an n-type layer (1×10^{18} Si atoms cm^{-3}), and a p-type layer (1×10^{18} Zn atoms cm^{-3}) on an n-type InP substrate (1×10^{18} Sn atoms cm^{-3}). The other sample, shown in Fig. 2-1 (b), consisted of a p-type layer (1×10^{18} Zn atoms cm^{-3}) on an n-type InP substrate (1×10^{18} Sn atoms cm^{-3}). In order to apply a reverse bias voltage across the p-n junction (Chapter 4), a p⁺-type InGaAs layer (1×10^{19} Zn atoms/ cm^3) was grown on the p-type InP layer. Here, this InGaAs layer was used as a contact layer to reduce the contact resistance [1,2]. This resistance can also be reduced by increasing the Zn concentration in the contact layer. However, the maximum Zn concentration in InP grown by

MOVPE is not sufficiently high ($\approx 1.5 \times 10^{18}$ atoms/cm³) to reduce the resistance [3]. Thus, an InGaAs layer was used to reduce the contact resistance instead, as it has a sufficiently high maximum Zn concentration ($\approx 2 \times 10^{19}$ atoms/cm³). Then, electrodes were deposited on both the p⁺-InGaAs layer (1×10^{19} Zn atoms/cm³) and the n-InP substrate.

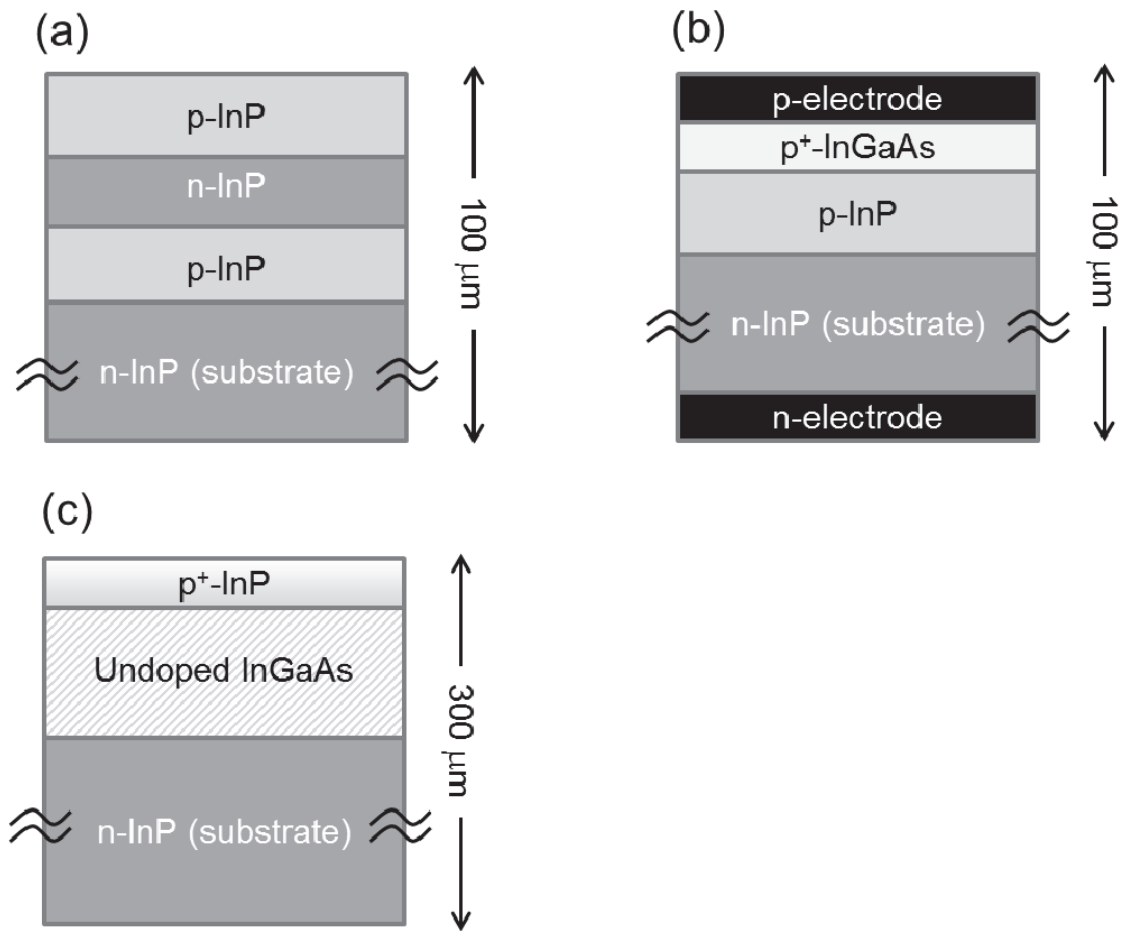


Fig. 2-1. Schematic drawing of samples used in this study.

The substrates of samples (a) and (b) were polished to a thickness of approximately 100 μm; both samples were polished for different reasons. Sample (a) was milled using argon (Ar⁺) ions, which will be discussed in

Chapter 3. For the ion milling, the sample was restricted to a 100- μm thickness, because of the limitations of the ion milling instruments used in this study. Therefore, polishing was required for the ion-milled sample. For sample (b), the electrodes were formed using a production line. In a normal InP device production line, the substrates are polished from 300–400 μm to approximately 100 μm in order to decrease the resistance of n-substrates and increase the cleaving yield. In this study, the same process was used so that the substrate was polished to a thickness of 100 μm , and the n-electrode was then formed on the back side of the wafer.

The third sample was a heterostructure composed of a p⁺-type InP layer (*ca.* 1×10^{19} Zn atoms/cm³) and an undoped InGaAs layer (n-type, 1×10^{16} atoms/cm³) on an n-type InP substrate (1×10^{18} Sn atoms/cm³), as shown in Fig. 2-1 (c). The undoped InGaAs and InP layers were first grown on n-type InP substrate using MOVPE. Then, Zn atoms were diffused from the surface of the undoped InP layer, resulting in a p⁺-InP layer. This sample is used in the experiments conducted in Chapter 5.

2.2 Sample preparation

Two methods were used for the sample preparation: cleaving and ion milling, the details of which are described in this section.

2.2.1 Manual cleavage

Sample cross-sections were prepared by manual cleaving. InP has a zinc blend structure and is easily cleaved. In this study, a two-inch InP wafer was scribed with a length of approximately 2 mm using a diamond scribe pen, and cleaved by separating both ends of the wafer using two pairs of tweezers. The sample sizes were cut to approximately 50–100 mm² by repeated cleavage. These dimensions were required for the samples to be fixed on a sample holder.

2.2.2 Ion milling

In Chapter 3, Ar⁺ ion beam milling instruments are used to prepare a cross-section in order to investigate the proposed sensitive and site-specific 2D dopant profiling method. The ion milling was conducted using a JEOL IB-09060CIS cryo ion slicer (CIS) [4] and, in order to prepare a cross-section using the CIS, the sample size was restricted to $3 \times 1 \times 0.1 \text{ mm}^3$. Because it is difficult to manually cleave an InP two-inch wafer with a thickness of 300 μm to such a small size, two instruments for mechanical polishing and wafer scribing were used to reduce the sample to less than $3 \times 1 \times 0.1 \text{ mm}^3$.

Figure 2-2 (a) shows the CIS apparatus, which consists of a cooling chamber and a sample chamber. A sample holder, Ar⁺ ion gun, masking plate, and cooling conductor are contained in the sample chamber. For this experiment, a small piece of silicon substrate was used as the masking plate. The cooling chamber has a liquid N₂ reservoir and a cooling conductor with a control knob. The sample temperature is controlled by moving the control knob, and was cooled to 150 K for the purposes of this study.

Figure 2-2 (b) is a schematic drawing of the ion gun, sample holder, masking plate and sample. Broad ion beam was irradiated from above the masking plate; this beam milled the unmasked portion of the sample to produce a cross-section parallel to the flat masking plate cross-section, as shown in Fig. 2-2 (c).

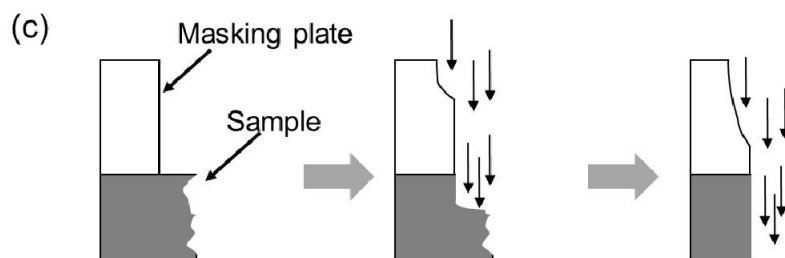
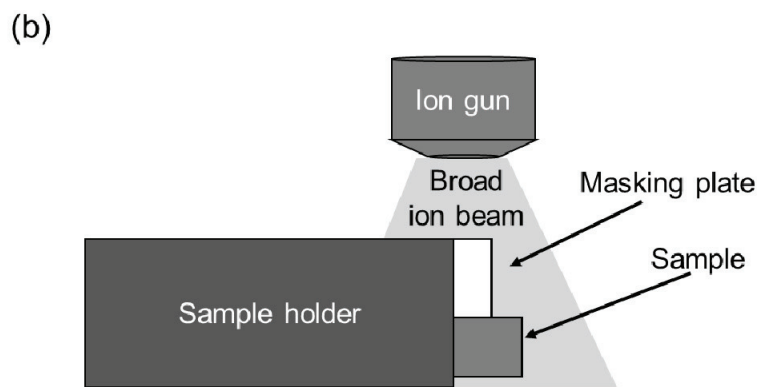
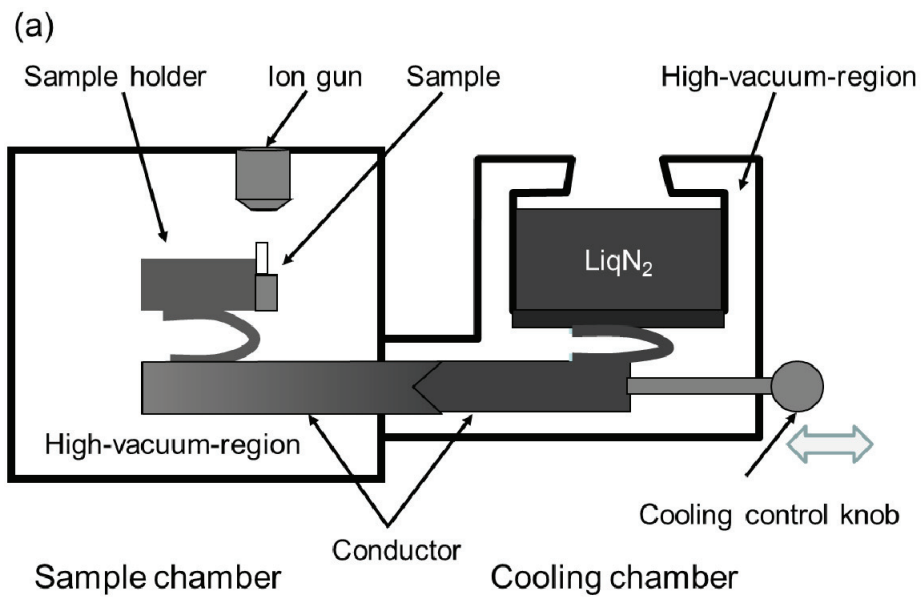


Fig.2-2. Schematic drawings of (a) the complete CIS system and (b) the ion gun. (c) Ion milling process [4,5].

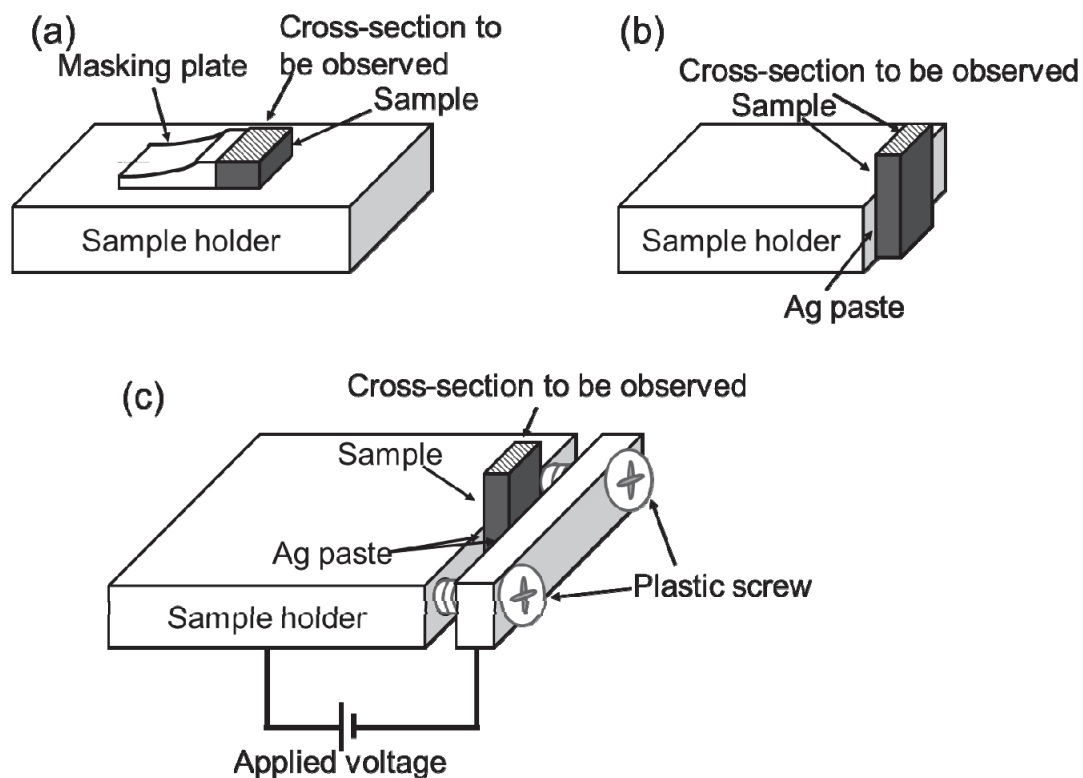


Fig.2-3. Illustrations of fixing methods used for (a) ion-milled, (b) manually cleaved, and (c) biased samples.

2.3 Sample fixation for SEM observation

The samples were fixed on an SEM sample stage using three methods, as shown in Fig. 2-3.

The ion-milled samples, which are discussed in Chapter 3, were fixed on the sample stage with a piece of a silicon substrate applied as a masking plate using silver (Ag) paste, as shown in Fig. 2-3 (a). The samples manually cleaved for use in the experiments conducted in Chapters 3–5 were fixed on the side of the sample stage using Ag paste, as illustrated in Fig. 2-3 (b). In Chapter 4, a reverse bias voltage is applied across the p-n junction of the InP in situ during SEM observation, using the sample shown in Fig. 2-1 (b). As shown in Fig. 2-3 (c), the sample was held between the sample stage and an

aluminum (Al) board connected to a voltage generator. In order to reduce the contact resistance, Ag paste was also used between the sample and the holder and the board. For the fixation of the Al board, plastic screws were used to prevent short-outs.

2.4 SEM observation

This section first presents the principles of SEM and the mechanism of dopant contrast. Then, the SEM apparatus structure and the secondary electron (SE) energy-filtering method used in this study are described. Finally, the process used for obtaining SE energy distributions and the contrast quantification method are described.

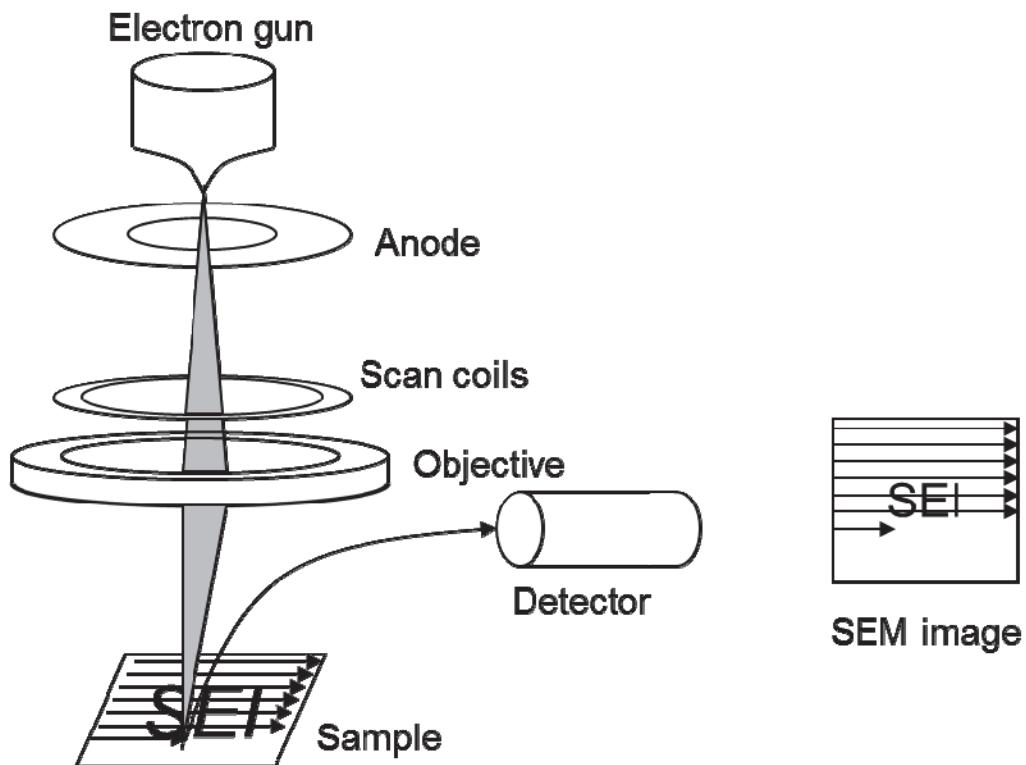


Fig. 2-4. SEM apparatus structure [6].

2.4.1 SEM observation mechanism

SEM (scanning electron microscopy) is a microscopy technique that obtains a magnified image using an electron beam. Figure 2-4 shows the schematic cross-section of the SEM apparatus [6]. A primary electron beam emitted from an electron gun is accelerated by an anode, focused on the sample surface using an objective lens, and two-dimensionally scanned. SEs and back scattered electrons (BSEs) are emitted from the scanned area because of the incident electron beam energy and detected by a detector. Images are then formed based on the number of SEs or BSEs.

In recent years, three types of electron guns and objective lenses, along with two types of detectors, have primarily been used.

The most commonly used electron guns are thermionic guns, Schottky-emission guns, and field-emission guns, as listed in Table 2-1. The spatial resolution is improved with smaller source size and energy spread. The spatial resolution of an SEM using a thermionic gun is relatively low, for example, it is 3.0 nm at an acceleration voltage of 30 kV [7]. Although this gun's lifetime is quite short compared to that of the other guns, it is very easy to exchange the gun and the SEM is inexpensive. Therefore the thermionic gun is used in a large number of companies, universities, and so on. An SEM with a Schottky-emission gun has a comparatively higher resolution. For instance, a resolution of 1.2 nm can be obtained with an acceleration voltage of 30 kV [8]. In addition, the probe current is higher and more stable and therefore, this gun is appropriate for element analysis using an energy dispersive X-ray spectrometer (EDX). Finally, a field-emission gun is used for ultra-high spatial resolution SEM. For example, the spatial resolution of a Hitachi SU9000 SEM is 0.4 nm at an acceleration voltage of 30 kV [9], although the probe current is lower and less stable than that of Schottky-emission guns.

Three types of objective lens are an out-lens, an in-lens, and a snorkel objective lens, as shown in Fig. 2-5 (a), (b), and (c) respectively.

An out-lens objective lens is the conventional objective lens. With this lens, the sample is located outside the magnetic field of the lens. In this case, the detector, called Everhart-Thornley (E-T) detector after its inventors, is placed in the sample chamber [10]–[13]. Because the sample is placed below

the objective lens, interference between the sample and the lens is prevented, even if a large sample is tilted. Thus, this lens allows the sample to be handled freely. However, the distance between the sample and the lens must be large, requiring a long focal length. Therefore, the aberration becomes large and a high resolution cannot be obtained.

Table 2-1. Characteristic parameters of electron guns [10]–[12].

Gun	Source size	Energy spread	Maximum probe current	Typical lifetime
Thermionic guns (Tungsten hairpin)	$> 10^4$ nm	2–4 eV	~ 300 nA	~ 200 h
Shottky-emission guns (thermal emission from ZrO/W tips)	≈15 nm	0.3–1.0 eV	~100 nA	> 1 year
Field-emission guns (tunneling from cold tungsten tips)	≈1 nm	0.2–0.5 eV	~ 10 nA	> 1 year

In contrast, in the case of the in-lens objective lens, the sample is inside the magnetic field of the lens. The through-the-lens (TTL) detector is placed above the objective lens. This geometry reduces the aberration of the electron beam and higher spatial resolution is therefore achieved, such as 1.2 nm at an acceleration voltage of 1 kV [9], despite the fact that an electron beam with a low acceleration voltage has a large aberration. However, this system has a drawback in that the sample size is limited to a few millimeters.

A system that compensates for this drawback and enables high spatial resolution imaging with low-acceleration voltage is the snorkel objective lens. This lens is designed to produce a lens magnetic field below the objective lens by leaking a strong magnetic field into this space. Therefore, although the sample is placed below the objective lens, it is inside

the magnetic field. Thus, a large sample can be handled freely and high spatial resolution can be obtained. For example, the spatial resolution of a Hitachi SU8000 is 1.3 nm at an acceleration voltage of 1 kV [14]. An SEM with this lens system typically has both E-T and TTL detectors.

Because dopant contrast can be clearly observed using a TTL detector with low acceleration voltage, the in-lens objective lens or the snorkel objective lens is appropriate for our purposes.

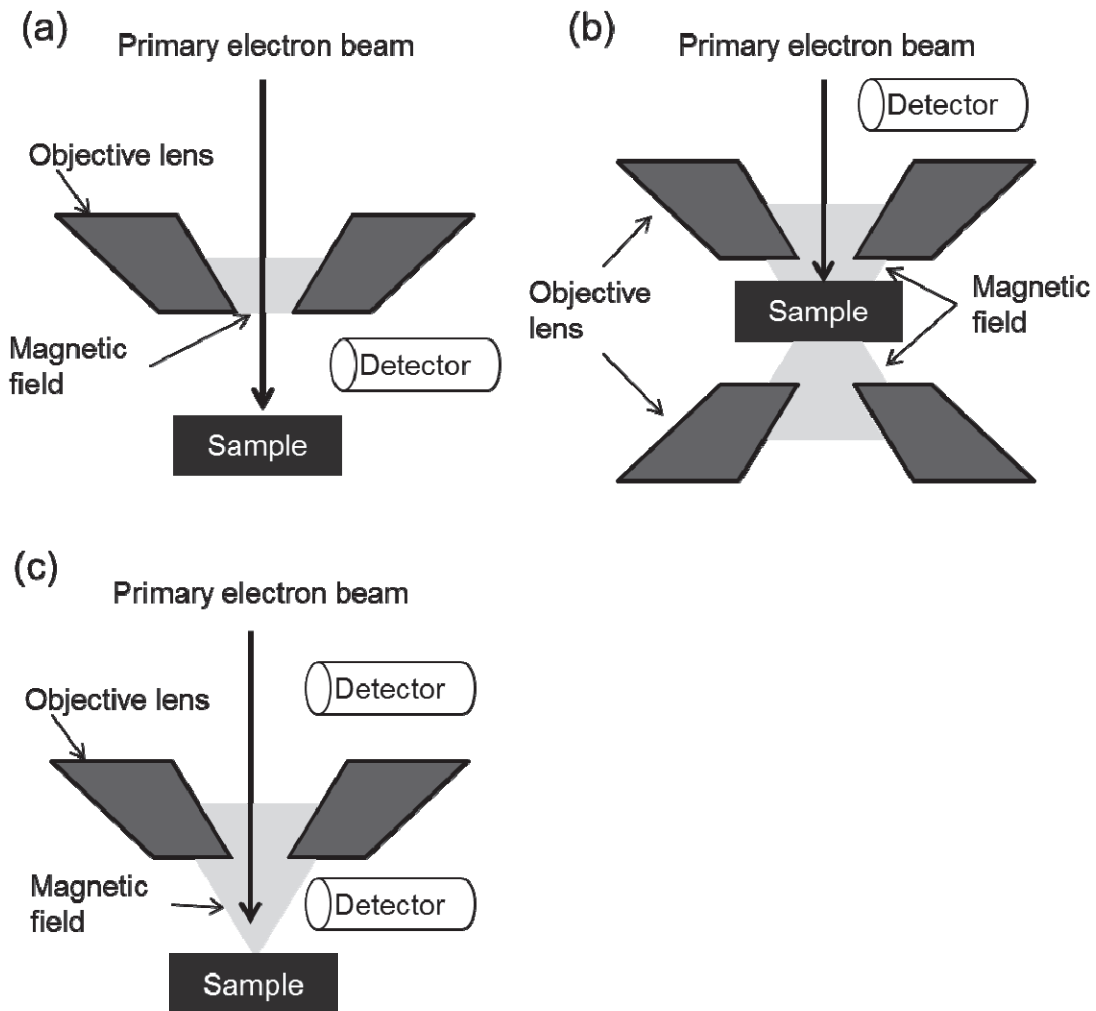


Fig. 2-5. Objective lens and detector types. (a) Out-lens objective lens and E-T detector. (b) In-lens objective lens and TTL detector. (c) Snorkel objective lens, E-T, and TTL detectors [12].

2.4.2 Dopant contrast mechanism in SEM

Contrast in SEM images can be categorized as topographic, material, voltage, or channeling. Although dopant contrast is considered to be caused by voltage contrast, the detailed mechanism is still unclear. This section introduces four proposed models.

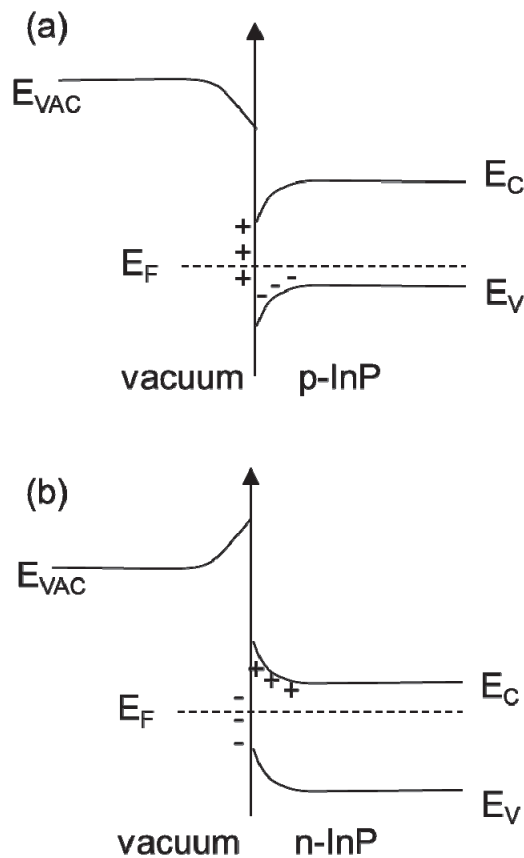


Fig. 2-6. Energy-band diagrams showing band bending due to the surface states of (a) p- and (b) n-type doped semiconductor surfaces [15,16].

The first model was suggested by Perovic *et al.* in 1995, when they demonstrated that the contrast of the observed SE intensity was not only dependent on the doping type, but was also sensitive to the doping

concentration levels. This model is based on the surface electric field theory [15,16]. Particular surface states caused by certain surface adsorbates and defects result in band bending near the surface, as shown in Fig. 2-6. Surface states are normally generated because of the disruption of the periodicity of the lattice at a surface and, theoretically, the surface state density for a surface is $\sim 10^{13} \text{ cm}^{-2}$. These surface states cause band bending close to the semiconductor surface, as shown in the band diagram. For p-doped materials, these surface bands bend downwards close to the surface, and for n-doped material the bands bend upwards. In addition, the shape of the surface barrier is modified by the surface states. This model suggests that electrons emitted into the vacuum from the valence band below the surface require higher energy in the case of n-type materials compared to p-type materials. This, in turn, increases the number of electrons escaping from the surfaces of the p-type doped regions in comparison with those emitted from the n-type regions. Hence, p-type regions appear brighter than n-type regions in the SE image.

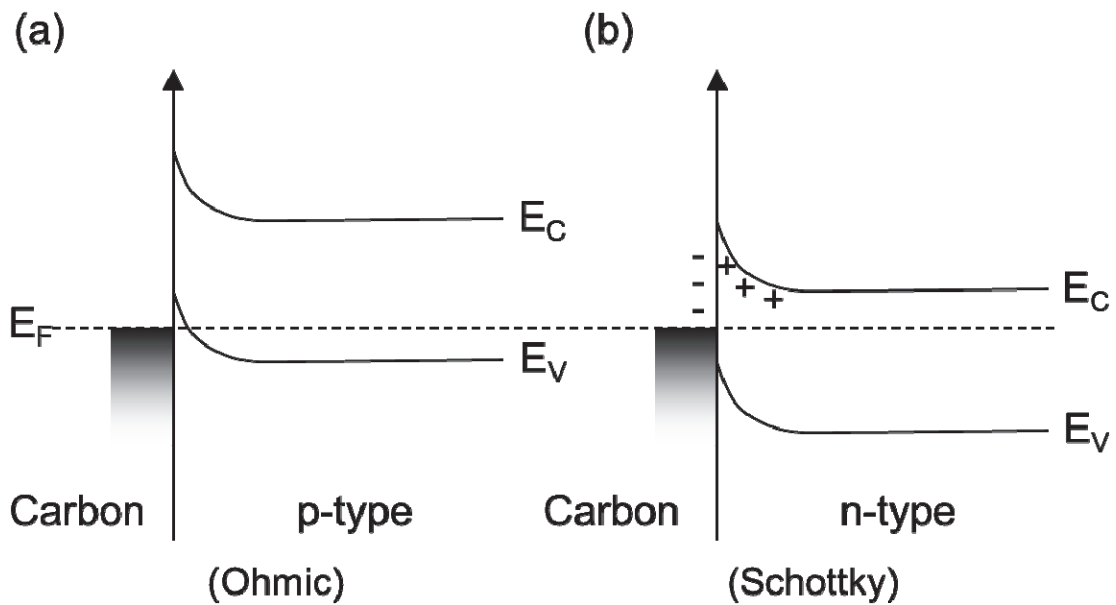


Fig. 2-7. Schematic diagram of graphite carbon with (a) p-type and (b) n-type semiconductor substrates producing ohmic and Schottky contacts [16,17].

A similar model, the metal-semiconductor charging theory (the so-called Schottky barrier theory) was suggested in 2001 by El-Gomati *et al* [16,17]. This model is applied when the surface is covered with a thin metallic layer. Since it is reported that hydro-carbon contamination is metallic, this model could be taken into account in the majority of cases. Figure 2-7 shows the band diagrams for (a) p-type and (b) n-type semiconductors when the surface is covered with graphite carbon [17]. Here, the work function of graphite is approximately 5.1 eV [17], while that of Si (InP) is approximately 4.9 eV [18] (4.6 eV [19]). This work function difference between the graphite carbon and doped semiconductors leads one to consider the possibility of metal-to-semiconductor contact formation between the carbon ad-layer and the semiconductors (Si or InP). A Schottky contact is formed for n-doped regions, while the contact is ohmic in p-doped regions. This theory suggests that the existence of a Schottky contact between n-doped regions and carbon would increase the potential barrier for SEs. As a result, the total SE yield from the n-doped regions would be reduced in comparison to that from the p-doped regions. This would result in two different SE yields and, hence, a contrast would exist between the two differently doped regions. In addition, the height of the Schottky barrier would be a function of the dopant concentration; thus, the SE yield would vary accordingly.

A widely-accepted model is the internal electric field theory, suggested by Sealy *et al.* in 2000 [16, 20–22]. According to this theory, dopant contrast is caused inside the sample because of band bending. Figure 2-8 is a schematic representation of the band structure of a p-n junction. In a p-n junction, the energy required to take an electron from the densely occupied valence band (E_v) to the local vacuum level (E_{VAC}) is independent of the dopant concentration, and can be shown to be unaffected by band bending at the surface. This theory's crucial parameter is the relative energy of an electron as far as the SEM chamber walls or detector (E_{SEM}), with respect to the local vacuum level just outside the sample. The position of E_{SEM} relative to the local vacuum level for p- and n-doped regions on either side of the junction lies mid-way between the local levels. Then, the ionization energy of the electrons in the p-type (E_p) regions is less than that in the n-type (E_n) regions, because of the internal electric field due to the built-in potential

associated with the p-n junction. This variation in energy gives rise to the collection of a different amount of SEs from each region, and these differences are observed in the form contrasts. Thus, a brighter p-type and darker n-type contrast is observed across the p-n junction in the SEM micrograph.

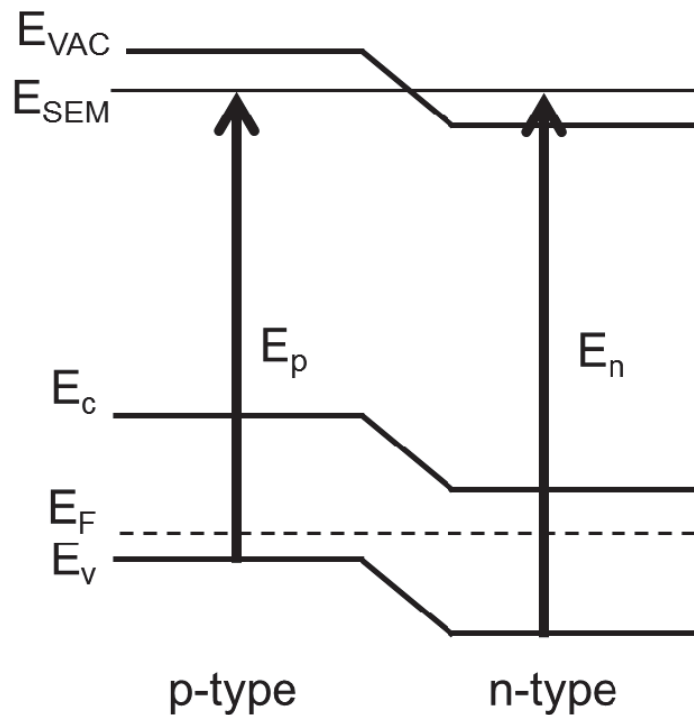


Fig. 2-8. Schematic representation of p-n junction band structure [20].

The fourth model is the external electric field theory described by Chee *et al* [22], [23]. Figure 2-9 shows a schematic drawing of the potential distribution for a p-n junction in an SEM chamber. The inherent potential of a p-n junction leads to an external electric field in the vacuum region above the sample surface. The electric field is positive and negative above the n-type and p-type regions, respectively. Hence, the SEs above the n-region experience acceleration toward the sample due to the electrostatic force, whereas those above the p-region are accelerated away from the sample, as

shown in Fig. 2-9. As a result, the collection efficiency of the SEs from the p-type regions increases and that from the n-type regions decreases, so that a brighter p-type and darker n-type contrast is observed across the p-n junction in the SEM micrograph.

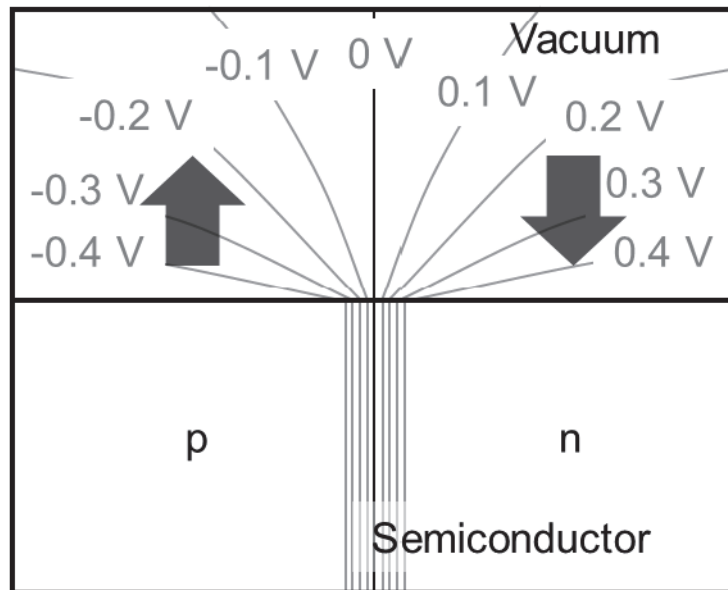


Fig. 2-9. Schematic diagram of potential distribution inside and outside a sample with a symmetric p-n junction [22].

2.4.3 Employed SEM and SE energy-filtering method

For the experiments conducted in Chapters 3–5, a Hitachi S-4800 FE-SEM (as shown in Fig. 2-10) is employed.

This SEM has a field-emission gun, a snorkel objective lens, and a TTL detector. The typical spatial resolutions are 1.0 and 2.0 nm at acceleration voltages of 15 and 1 kV, respectively. In these experiments, SE high-pass energy-filtered images are obtained using an $E \times B$ system comprising orthogonal electrostatic and magnetic fields [12,24].



Fig. 2-10. SEM apparatus employed in this research.

Figure 2-11 (a) shows the $E \times B$ detector system for high-pass energy-filtered images. In the energy-filtered images, detection of both SEs and BSEs is permitted and, for SE energy-filtering, a SE control electrode is used. By changing the voltage of the SE control electrode (V_c), the minimum energy of the SEs that are allowed to pass can be selected, thus forming high-pass energy-filtered images. The value of V_c can be set to values from 0–150 V at 1.5 V intervals. This control electrode functions as a conversion electrode to convert BSEs generated at low angles into SEs. These SEs carry information on the contrast characteristics of the BSEs. When $V_c = 0$ V, the BSE and SE signals are simply combined, as shown in Fig. 2-11 (b). Because the number of BSEs is generally much less than the number of SEs, the images of $V_c = 0$ V contain the SE characteristic contrast.

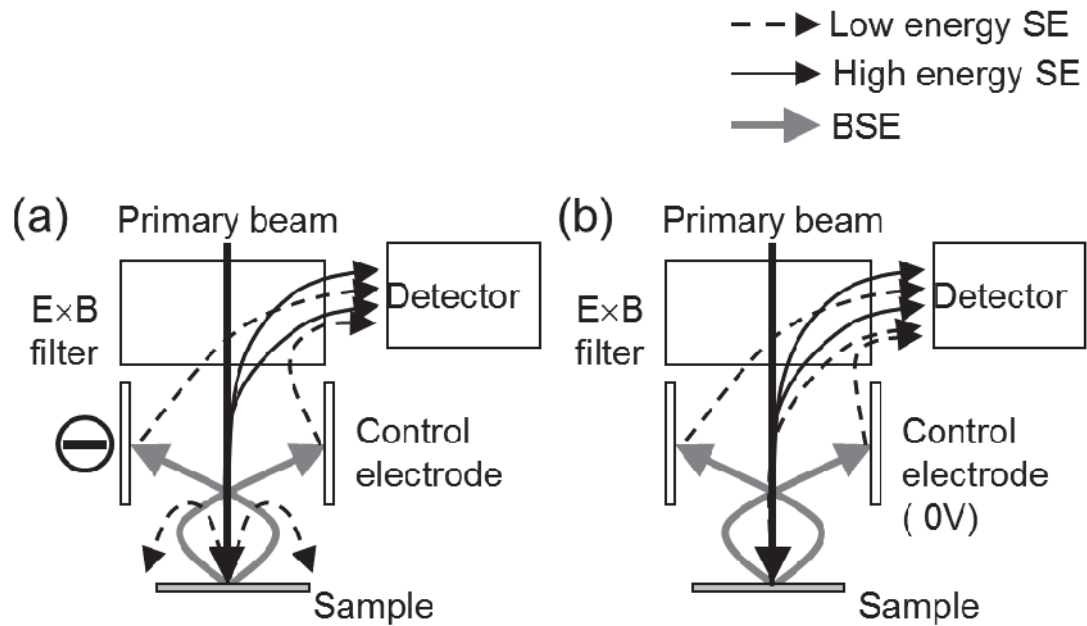


Fig. 2-11. Schematic drawing of Hitachi S-4800 SEM with TTL detector. (a) High-pass energy-filtering system. (b) Energy-filtering system at $V_c = 0$ V [12,24].

2.4.4 SE energy distribution observation method

In Chapter 4, SE energy distributions are obtained, and this section describes the method used to observe those distributions.

SEs are emitted from the area irradiated by the primary electron beam. These SEs are detected and SEM images are formed based on the difference in the SE emission yield. In order to investigate the dopant contrast behavior, SE emission energy distributions [12] similar to that shown in Fig. 2-12 are used in this study.

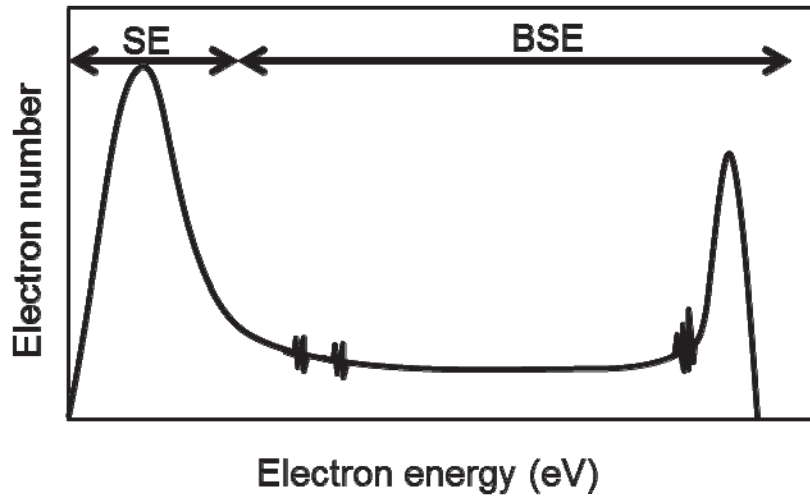


Fig. 2-12. SE and BSE energy distribution [12].

SE energy distribution was obtained using energy-filtering as follows [23,24]. First, a series of images were collected for energy-filtered images in the range of $0 \text{ V} \leq V_c \leq 15 \text{ V}$, as shown in Fig. 2-13 (a). The digital SE images were obtained with 256 gray levels, and the intensities were extracted from all the images using the Image J software package [26,27]. Figure 2-13 (b) shows an example. Then, $g(V_c)$, which is the total signal intensity as a function of V_c , was obtained as shown in Fig. 2-13 (c).

V_c is the voltage of the control electrodes and, therefore, it is equivalent to the SE energy threshold in the high-pass energy-filtering. That is, the total signal intensity, $g(V_c)$, is expressed as $g(V_c) = g(E)$, where E is SE energy. Here, the SE energy distribution, $f(E)$, can be expressed by the following equation:

$$f(E) = \frac{dg(E)}{dE} \dots\dots\dots (2-1)$$

This equation indicates that experimental SE distributions can be obtained by differentiating the total signal intensity, $g(E)$, with respect to E . Figure 2-14 shows an example of an SE energy distribution obtained using this method.

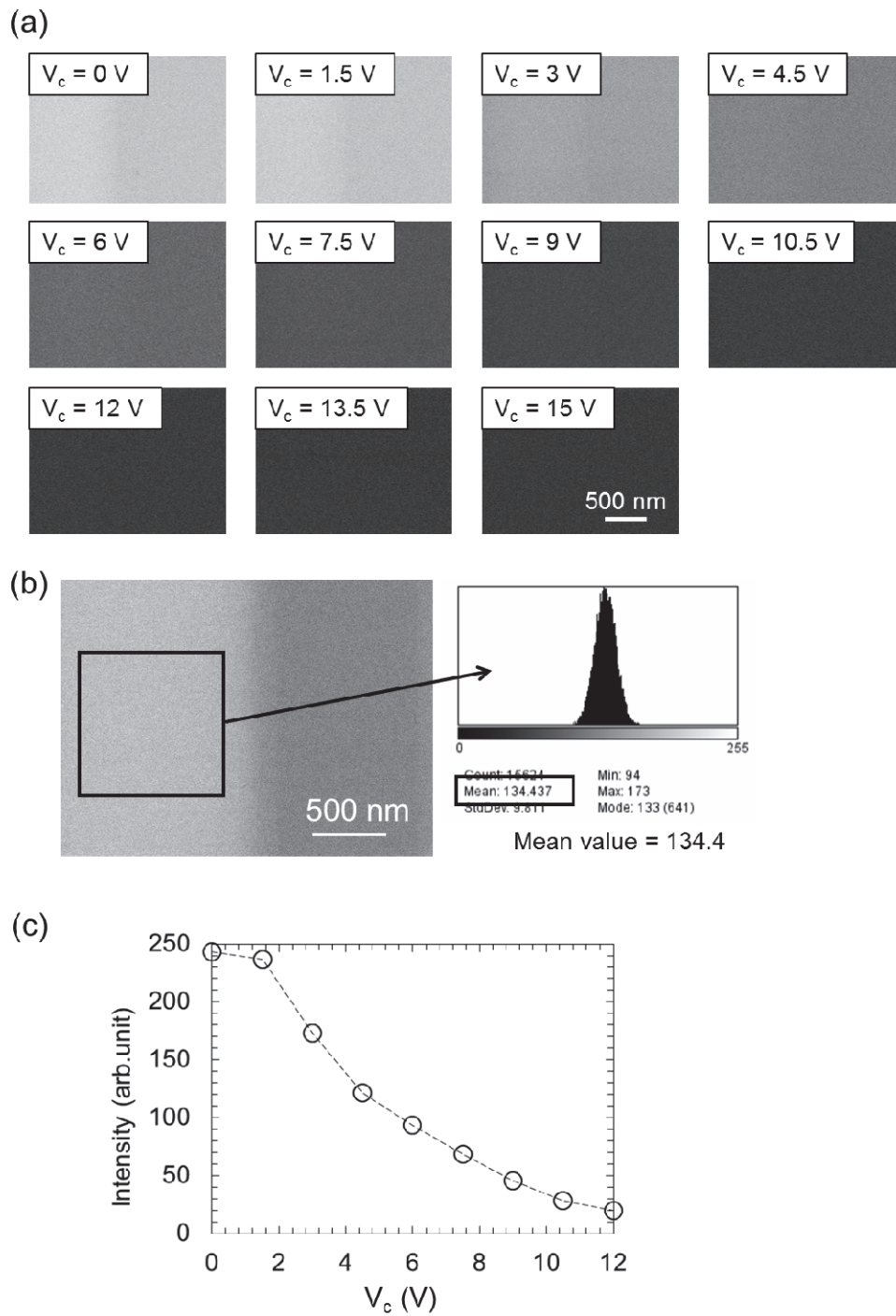


Fig. 2-13. (a) Energy-filtered images in the $0 \text{ V} \leq V_c \leq 15 \text{ V}$ range. (b) Method used to extract intensities from SEM images. (c) Total signal intensity as a function of V_c .

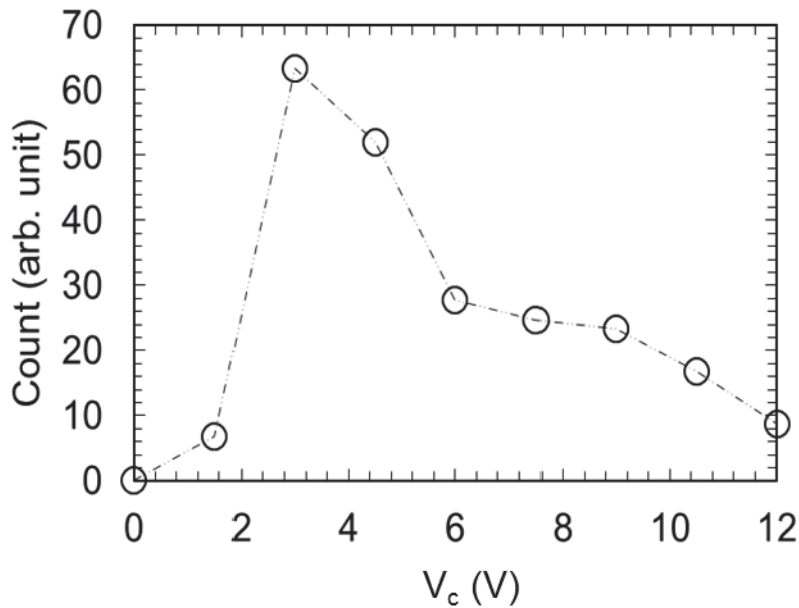


Fig. 2-14. Example of SE energy distribution obtained using this method.

2.5 Dopant contrast quantification method

The dopant contrast obtained in Chapters 3 and 4 is quantified for analysis and discussion. Although several methods exist through which to quantify the contrast [13,28–31], the following equation was used in this study, as derived by Seiler [13] and Schönjahn *et al.* [28]

$$C_{pn}(\%) = 100 \frac{I_p - I_n}{I_p + I_n}, \dots\dots\dots(2 - 2)$$

where I_p and I_n are the SEM image intensities from the p-type and n-type layers, respectively. I_p and I_n are extracted from the digital image by averaging the intensity as previously described (Fig. 2-12).

2.6 Summary

This chapter began by introducing the sample structures and the sample preparation methods, focusing in particular on ion milling. Then, the details of SEM, that is, the imaging principles, the concept of dopant contrast, and the SE energy-filtering theory and method, were described. Finally, the process used to obtain SE energy distributions and the dopant contrast quantification method were presented.

Chapters 3, 4, and 5 describe the respective investigations of the three major problems presented in Chapter 1, using the methods introduced in this chapter.

2.7 References

- [1] N. Ikoma, T. Kawahara, N. Kaida, M. Murata, A. Moto, and T. Nakabayashi, "Highly Reliable AlGaInAs Buried Heterostructure Lasers for Uncooled 10Gb/s Direct Modulation - Technical Digest (CD)," in *Optical Fiber Communication Conference and Exposition and The National Fiber Optic Engineers Conference*, 2005, p. OThU1.
- [2] H. Yano, M. Murata, G. Sasaki, and H. Hayashi, "A high-speed eight-channel optoelectronic integrated receiver array comprising GaInAs p-i-n PD's and AlInAs/GaInAs HEMTs," *J. Light. Technol.*, vol. 10, no. 7, pp. 933–937, 1992.
- [3] G. B. Stringfellow, *Organometallic Vapor-Phase Epitaxy: Theory and Practice*. San Diego / London: Academic Press, 1999.
- [4] Y. Nakajima, M. Shibata, H. Matsushima, T. Suzuki, and N. Erdman, "High Quality Cross Sections of Low Melting Point Samples Prepared with Cryo Ion Slicer - Broad Ar Ion Beam Milling Apparatus with a Newly Developed Specimen Cooling Unit," *Microsc. Microanal.*, vol. 17, no. S2, pp. 1194–1195, 2011.

- [5] H. Takahashi, A. Sato, M. Takakura, N. Mori, J. Boerder, W. Knoll, and J. Critchell, "A New Method of Surface Preparation for High Spatial Resolution EPMA/SEM with an Argon Ion Beam," *Microchim. Acta*, vol. 155, no. 1–2, pp. 295–300, 2006.
- [6] The surface Science Society of Japan, Ed., *ナノテクノロジーのための走査電子顕微鏡 (in Japanese)*. Tokyo: Maruzen Publishing Co. Ltd, 2004.
- [7] "Hitachi High Technologies America, Inc.; (2014); Scanning Electron Microscope SU1510." [Online]. Available: <http://www.hitachi-hitec.com/global/em/sem/su1510.html>. [Accessed: 15-Mar-2014].
- [8] "Hitachi High Technologies America, Inc.; (2014); Scanning Electron Microscope SU6600." [Online]. Available: <http://www.hitachi-hitec.com/global/em/fe/su6600.html>. [Accessed: 15-Mar-2014].
- [9] "SU9000 UHR FE-SEM | Hitachi High Technologies America, Inc." [Online]. Available: <http://www.hitachi-hita.com/products/electron-microscopes-and-focused-ion-beam/field-emission-sem/su9000-uhr-fe-sem>. [Accessed: 15-Mar-2014].
- [10] L. Reimer, *Image Formation in Low-voltage Scanning Electron Microscopy*. Bellingham, Washington: SPIE Press, 1993.
- [11] L. Reimer, *Scanning Electron Microscopy: Physics of Image Formation and Microanalysis*. Verlag Berlin Heidelberg New York: Springer, 1998.
- [12] The Japanese Society of Microscopy, *New Scanning Electron Microscopy (in Japanese)*. Tokyo: Kyoritsu Shuppan Co., Ltd., 2011.
- [13] H. Seiler, "Secondary electron emission in the scanning electron microscope," *J. Appl. Phys.*, vol. 54, no. 11, pp. R1–R18, 1983.

- [14] “Ultra-high Resolution Scanning Electron Microscope SU8000 : Hitachi High-Technologies Corporation.” [Online]. Available: <http://www.hitachi-hitec.com/global/em/fe/su8000.html>. [Accessed: 29-May-2014].
- [15] D. D. Perovic, M. R. Castell, A. Howie, C. Lavoie, T. Tiedje, and J. S. W. Cole, “Field-emission SEM imaging of compositional and doping layer semiconductor superlattices,” *Ultramicroscopy*, vol. 58, no. 1, pp. 104–113, 1995.
- [16] M. El-Gomati, F. Zaggout, H. Jayacody, S. Tear, and K. Wilson, “Why is it possible to detect doped regions of semiconductors in low voltage SEM: a review and update,” *Surf. Interface Anal.*, vol. 37, no. 11, pp. 901–911, 2005.
- [17] M. M. El-Gomati and T. C. R. Wells, “Very-low-energy electron microscopy of doped semiconductors,” *Appl. Phys. Lett.*, vol. 79, no. 18, pp. 2931–2933, 2001.
- [18] S. M. Sze, *Physics of Semiconductor Devices*, 2nd ed. New York: J. Wiley & Sons, 1981.
- [19] R. K. W. A. C. Beer, *Physics of III-V Compounds, Volume 2*. New York: Academic Press, 1966.
- [20] C. Sealy, M. Castell, and P. Wilshaw, “Mechanism for secondary electron dopant contrast in the SEM,” *J. Electron Microsc. (Tokyo)*, vol. 49, no. 2, pp. 311–321, 2000.
- [21] G. H. Jayakody, T. R. C. Wells, and M. M. El-Gomati, “Imaging of doped Si in low and very low voltage SEM: the contrast interpretation,” *J. Electron Spectros. Relat. Phenomena*, vol. 143, no. 2–3, pp. 233–239, 2005.
- [22] A. K. W. Chee, R. F. Broom, C. J. Humphreys, and E. G. T. Bosch, “A quantitative model for doping contrast in the scanning electron microscope using calculated potential distributions and Monte Carlo simulations,” *J. Appl. Phys.*, vol. 109, no. 1, 013109, 2011.

- [23] P. Kazemian, S. A. M. Mentink, C. Rodenburg, and C. J. Humphreys, “High resolution quantitative two-dimensional dopant mapping using energy-filtered secondary electron imaging,” *J. Appl. Phys.*, vol. 100, no. 5, 054901, 2006.
- [24] D. Tsurumi, K. Hamada, and Y. Kawasaki, “Energy-filtered imaging in a scanning electron microscope for dopant contrast in InP.,” *J. Electron Microsc. (Tokyo)*, vol. 59 Suppl 1, pp. S183–S187, 2010.
- [25] D. Tsurumi, K. Hamada, and Y. Kawasaki, “Highly Reproducible Secondary Electron Imaging under Electron Irradiation Using High-Pass Energy Filtering in Low-Voltage Scanning Electron Microscopy,” *Microsc. Microanal.*, vol. 18, no. 02, pp. 385–389, 2012.
- [26] M. D. Abràmoff, I. Hospitals, P. J. Magalhães, and M. Abràmoff, “Image Processing with ImageJ,” *Biophotonics Int.*, vol. 11, pp. 36–42, 2004.
- [27] C. A. Schneider, W. S. Rasband, and K. W. Eliceiri, “NIH Image to ImageJ: 25 years of image analysis,” *Nat. Methods*, vol. 9, no. 7, pp. 671–675, 2012.
- [28] C. Schönjahn, C. J. Humphreys, and M. Glick, “Energy-filtered imaging in a field-emission scanning electron microscope for dopant mapping in semiconductors,” *J. Appl. Phys.*, vol. 92, no. 12, pp. 7667–7671, 2002.
- [29] S. L. Elliott, R. F. Broom, and C. J. Humphreys, “Dopant profiling with the scanning electron microscope—A study of Si,” *J. Appl. Phys.*, vol. 91, no. 11, pp. 9116–9122, 2002.
- [30] C. Schönjahn, R. F. Broom, C. J. Humphreys, A. Howie, and S. A. M. Mentink, “Optimizing and quantifying dopant mapping using a scanning electron microscope with a through-the-lens detector,” *Appl. Phys. Lett.*, vol. 83, no. 2, pp. 293–295, 2003.

- [31] S. Chung, V. Wheeler, R. Myers-Ward, L. O. Nyakiti, C. R. Eddy, D. K. Gaskill, M. Skowronski, and Y. N. Picard, "Secondary electron dopant contrast imaging of compound semiconductor junctions," *J. Appl. Phys.*, vol. 110, no. 1, 014902, 2011.

Chapter 3

Development of Sample Preparation Technique

This chapter presents the development of an effective sample preparation technique [1]. Such a technique is necessary because low sensitivity due to poor sample preparation is one of the three problems impeding the industrial use of 2D dopant profiling using SEM, as explained in Chapter 1.

3.1 Introduction

This section discusses the problem of preparing a cross-section in order to observe 2D dopant profiles in compound semiconductor devices. First, it is shown that a site-specific cross-section is required for process characterization and failure analysis, and that ion milling is an appropriate technique to achieve this because of its positional precision. Then, previous studies related to the 2D dopant profiling using SEM of surfaces prepared through ion milling are reviewed, and the problematic issue is clarified.

3.1.1 Significance of 2D dopant profiling of surfaces prepared through ion milling

As described in Chapter 1, one of the major analysis methods for process characterization and failure analysis in R&D and production is 2D dopant profiling. For failure analysis dopant profiling, the failure location must be identified using systems such as IR-OBIRCH [2,3] and EMS [4–6], and the cross-section must be prepared. The failure location size is typically less than 1 μm ; therefore, positional precision of less than 1 μm is required for the cross-section preparation.

The cross-section preparation methods that have become widespread recently are primarily cleaving, mechanical polishing, and ion milling, as shown in Table 3-1. Of these methods, the only technique providing positional precision of less than 1 μm for any device containing mounted samples is ion milling; therefore, there is no choice but to use this method. Thus, 2D dopant profiling using ion-milled surfaces must inevitably be used for the failure analysis.

Table 3-1. Cross-section preparation methods that have become widespread recently.

Method	Cleaving	Mechanical Polishing	Ion milling
Positional precision	1 μm –	1 μm –	10 nm–
Observable area	Unlimited	25 mm	10–500 μm
Turnaround time	1 h	1 day	1 day
Surface damage [7]	Low	High	High
Mounted sample	Impossible	Possible	Possible

3.1.2 Problems in 2D dopant profiling of ion-milled surfaces using SEM

The 2D dopant profiling using SEM of ion-milled surfaces has two problems: decreased contrast and the surface roughness generated by ion milling.

First, a decrease in dopant contrast will be discussed. The first observation of dopant contrast on an ion-milled surface was performed by Kazemian *et al.* in 2006 [7]. They prepared a cross-section of a silicon p-n junction using focused ion beam (FIB) milling and demonstrated the observation of the dopant contrast, although the contrast was only 1/10 that of the cleaved surface. They explained that this decrease in contrast is due to the generation of a surface amorphous layer. Further, this significant decrease in contrast leads to insensitivity to low dopant concentrations, which makes it impossible to achieve sensitive 2D dopant profiling. With the aim of improving the contrast, a study was conducted in which the dopant contrast dependence on the amorphous layer thickness was investigated using a silicon p-n junction and varying the Ga⁺ ion-milling energy [8]. However, the obtained contrast was only half that of the cleaved surface. In addition, although experiments using final Ar⁺ ion polishing, which is often used to further reduce the amorphous layer thickness to approximately 1 nm (for transmission electron microscopy (TEM)) [9], were conducted, the contrast was also half that of the cleaved surface [10]. Thus, although a certain effect can be seen by removing the ion-milling-generated amorphous layer, the contrast is still lower than that of cleaved surfaces.

In addition, compound semiconductor materials, especially InP, are more damage-labile than silicon. For example, the amorphous layer thickness generated through Ga⁺ ion-milling is 21 nm for silicon [11] but 33 nm for InP [12]. Therefore, the generation of an amorphous layer during cross-section preparation using ion milling is a serious problem.

The second issue connected with ion milling is surface roughness. It is well known that surface roughness is generated by ion milling for InP, GaInN, etc. [13–16], and Fig. 3-1 shows an example of roughness generated

on an InP surface. This roughness becomes an obstacle to fine 2D dopant profiling and therefore, it must be removed.

Thus, the cross-section preparation using ion milling for the 2D dopant profiling of a compound semiconductor has two serious problems; namely, insensitivity and surface roughness.

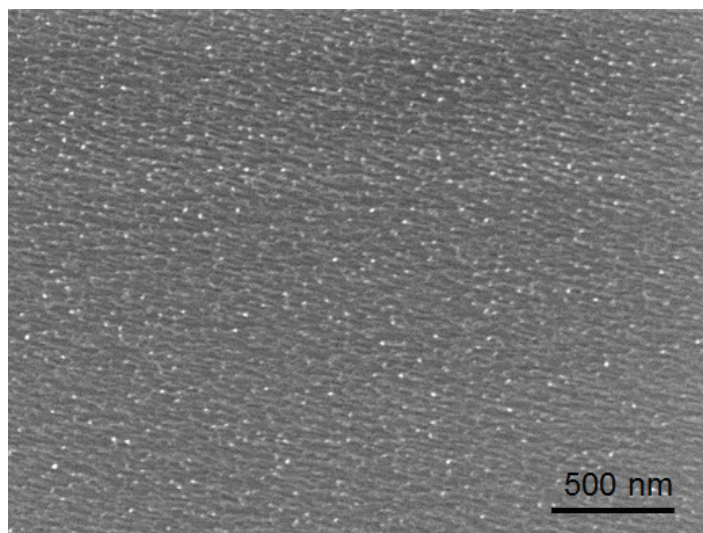


Fig. 3-1. InP surface prepared by ion milling.

3.2 Purpose

Motivated by the discussion given above, the purpose of this chapter is to investigate the cross-section preparation method and to increase the dopant contrast from ion-milled surfaces. The aims are to increase the contrast to the same level as that of cleaved surfaces and, also, to remove the surface roughness.

3.3 Experimental Method

This section presents the cross-section preparation method used in this study, providing an explanation of the technique and outlining the difference between the methods used in this and previous studies.

3.3.1 Sample

The sample investigated here was an InP test structure grown using chemical vapor deposition, as shown in Fig.2-1 (a). The structure consisted of a p-type layer (1×10^{18} Zn atoms/cm³) on an n-type layer (1×10^{18} Si atoms/cm³).

3.3.2 Sample preparation method

Ar⁺ ion milling with cooling was employed for the sample preparation. As mentioned above, a previous study demonstrated the application of Ar⁺ ion milling in order to remove the amorphous layer produced during previous ion milling. However, the ion-milling involved 1-keV Ar⁺ ions after an initial 30-keV Ga⁺ ion treatment. Theoretically, 1-keV ion milling generates an amorphous layer of approximately only 1 nm in thickness. However, the milling rate of 1-keV ions is generally low, and it was therefore possible that the 1-keV ion milling would not be sufficiently strong to remove the >20-nm-thick amorphous layer generated by the 30-keV ions. In order to effectively remove the amorphous layer, it is in fact necessary to gradually reduce the milling energy. Using this approach, this study found that the amorphous layer was then gently removed.

In order to suppress the surface roughness, ion milling with sample cooling was demonstrated based on previous studies involving Auger electron spectroscopy (AES) sputtering and TEM sample preparation [17,18]. The effectiveness of the sample cooling is described as follows.

For InP, the preferential sputtering of phosphorous atoms leads to the enrichment of indium (In) atoms on the surface, which then diffuse and form In cones. The sputtering yield of In is less than that of InP; therefore, the InP surface is sputtered faster than the metallic In regions, which leads to surface roughness [19,20]. To suppress the formation of surface roughness, a milling method using the liquid nitrogen (LN₂) sample holder has been employed in previous studies [17,18], so that the In atoms did not diffuse at the cooled sample surface and In cone formation and surface roughness was prevented.

Thus, the method of cooling the sample during ion milling was applied to the 2D dopant profiling using SEM technique. Ion milling was conducted using a JEOL IB-09060CIS, as introduced in Section 2.2.2. The finishing Ar⁺ ion milling was performed at 1.5, 2.5, 4.0, and 6.0 keV with an incidence angle of ~3.5° providing ion currents of 40, 65, 120, and 260 μA, respectively. The milling process stages are shown in table 3-2. The samples were milled using a LN₂ cooled sample holder that had a temperature of approximately 150 K.

Table 3-2. Ar⁺ ion milling process.

Finishing Ar ⁺ ion energy	Process
1.5 keV	4.0 keV → 2.0 keV → 1.5 keV
2.5 keV	4.0 keV → 2.5 keV
4.0 keV	4.0 keV
6.0 keV	6.0 keV

3.3.3 SEM observation conditions

SEM images were collected using a through-the-lens (TTL) detector in a Hitachi S-4800 FE-SEM microscope, as described in Section 2.4. Experimental images were obtained with $V_c = 3$ V to reduce the influence of electron beam irradiation [21,22], while the working distance was 2 mm.

The same contrast and brightness settings were used for a series of images. A contrast value, C_{pn} , was obtained as described in Section 2.5.

3.4 Surface roughness results and discussion

Figure 3-2 shows the surface roughness of the cleaved and ion-milled samples for a primary electron beam acceleration voltage of 1 kV. As well as the AES results [17], smooth mirror-like surfaces were observed for the samples prepared using 1.5 and 2.5 keV milling, which suggests that the samples were sufficiently cooled to prevent In atom diffusion at the sample surfaces. The nanometric surface roughness in the sample prepared with 6.0-keV ion milling implies that the surface temperature during milling was increased because of the high Ar^+ ion energy and current. The dappled contrast in the sample prepared with 4.0-keV ion milling may also be due to a temperature increase, although such a surface state (dappled contrast) has not been previously reported. Such unfavorable surface problems could be solved by decreasing the milling ion current, even though the milling ion energy is 4.0 or 6.0 keV, because the sample temperature plays an important role in determining the result surface structure [18].

3.5 Dopant contrast results and discussion

This section first shows the observed results for a primary electron beam acceleration voltage of 1 kV. The amorphous layer thickness of each sample is calculated and the relationship between dopant contrast and the amorphous layer thickness is then discussed. Subsequently, the contrast dependence on the acceleration voltage is shown, and the relationship between the dopant contrast, amorphous layer thickness, and electron beam penetration depth is discussed.



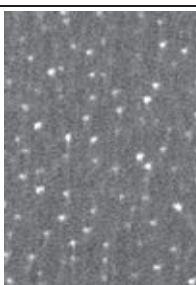
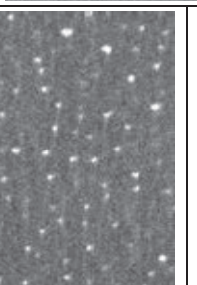
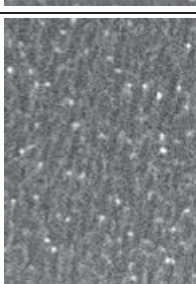
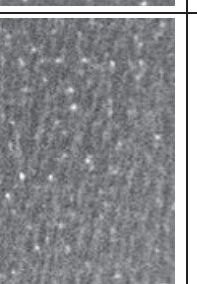
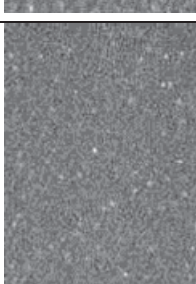
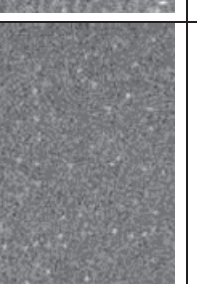
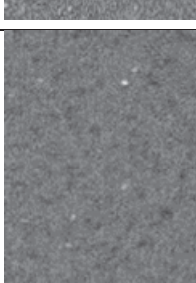
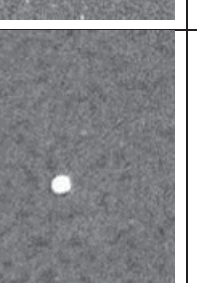
		Temperature	
		Room Temp.	150 K
Ar ⁺ ion energy (keV)	0 (as-cleaved)		
	1.5		
	2.5		
	4.0		
	6.0		

Fig. 3-2. Surface roughness of cleaved and ion-milled samples.

3.5.1 Results (SEM acceleration voltage: 1 kV)

Figure 3-3 shows the dopant contrast of the (a) cleaved and (b-e) 150-K-milled samples. The acceleration voltage of the primary electron beam was set to 1 kV in order to increase the dopant contrast [23].

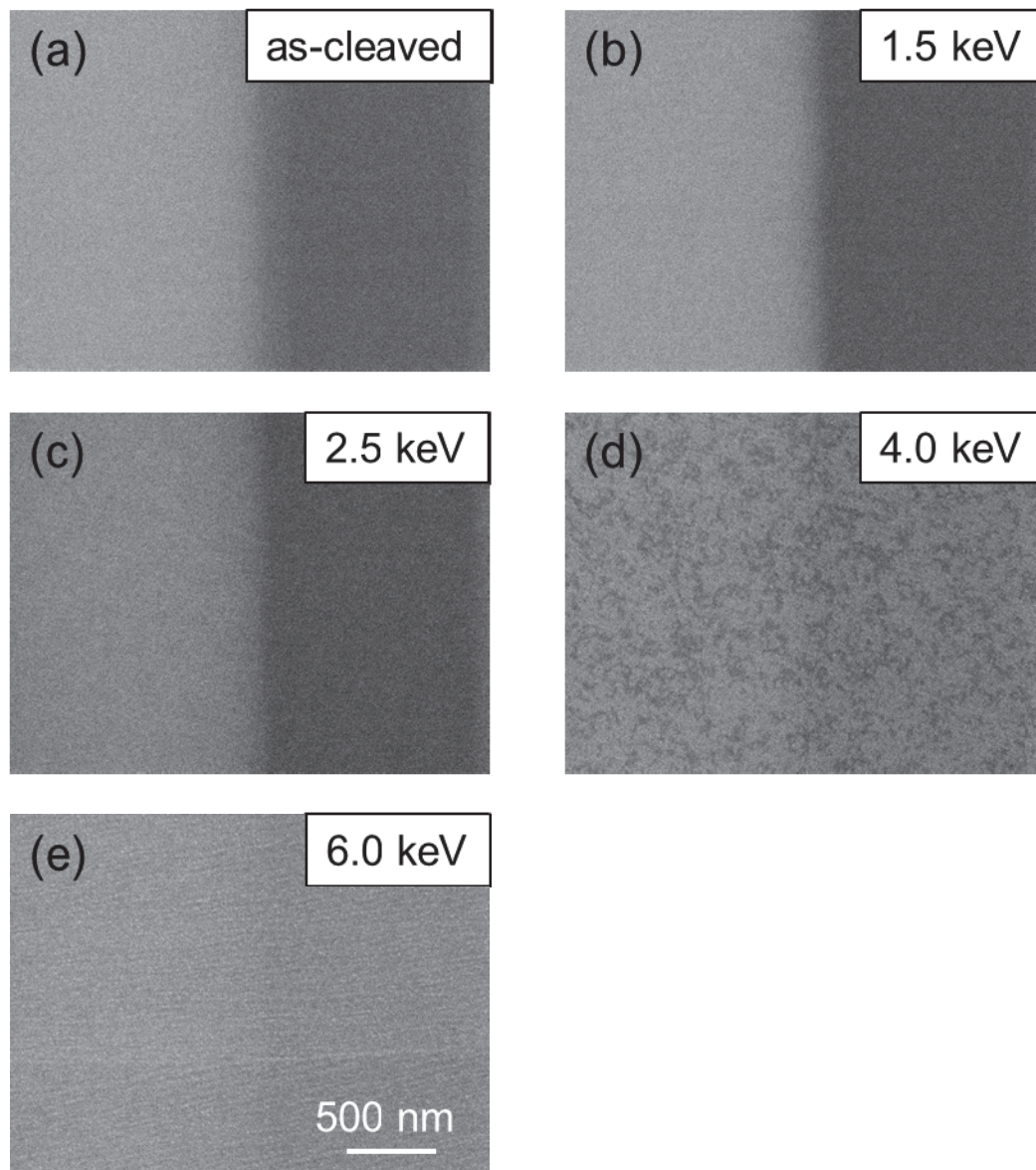


Fig. 3-3. Dopant contrast of (a) cleaved and (b-e) 150-K-milled samples [1].

The contrast of the surface prepared using 1.5-keV milling [Fig.3-3 (b)] was almost the same as that of the cleaved surface [Fig. 3-3 (a)] and, as the ion beam energy was increased, the contrast decreased [Fig. 3-3 (b-e)]. Almost no contrast was visible from the surface prepared using 6.0-keV milling [Fig.3-3 (e)]

For the quantitative discussion, the intensities from the p-type and n-type regions (as shown in Fig. 3-4) were substituted into equation (2-2), and C_{pn} was derived. The value of C_{pn} for the surface prepared using 1.5-keV milling [Fig.3-3 (b)] was 20%, which was almost identical to that of the cleaved surface (19%) [Fig. 3-3 (a)]. This indicates that low-energy Ar^+ ion milling generates little damaged surfaces that are suitable for site-specific 2D dopant profiling. As the ion beam energy was increased from 1.5 keV [Fig. 3-3 (b)] to 2.5, 4.0, and 6.0 keV [Fig. 3-3 (c), (d), and (e), respectively], C_{pn} decreased from 20% to 16, 6, and 4%, respectively.

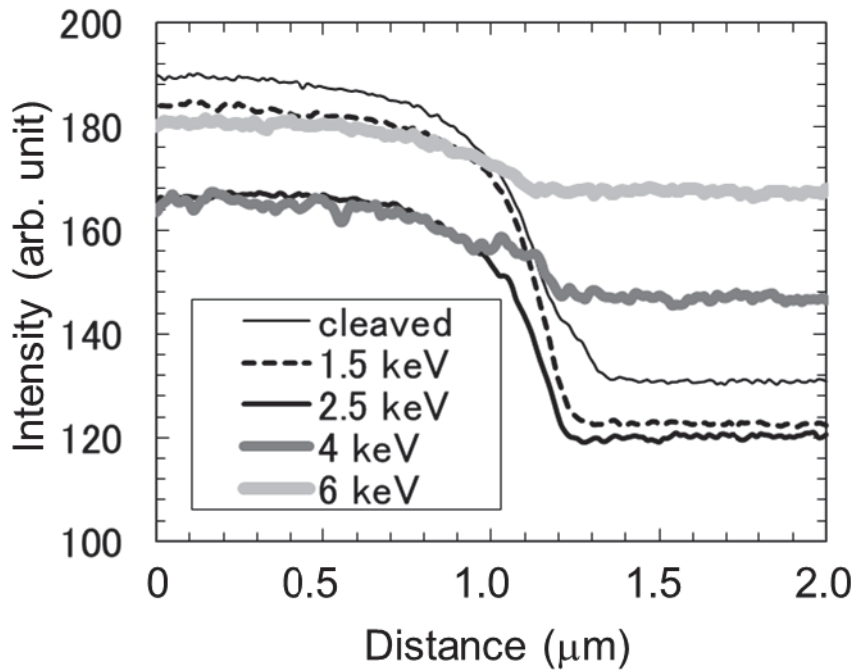


Fig. 3-4. SE intensity as a function of distance across InP p-n junction. The derived C_{pn} values of the cleaved samples and those milled at 1.5, 2.5, 4.0, and 6.0 keV are 19, 20, 16, 6, and 4%, respectively [1].

3.5.2 Calculation of amorphous thickness

The main reason why the C_{pn} for the surface milled using low-energy Ar^+ ions was as high as that from a cleaved surface was that the amorphous layer generated by ion milling was still sufficiently thin to allow contrast in the SEM to be successfully observed.

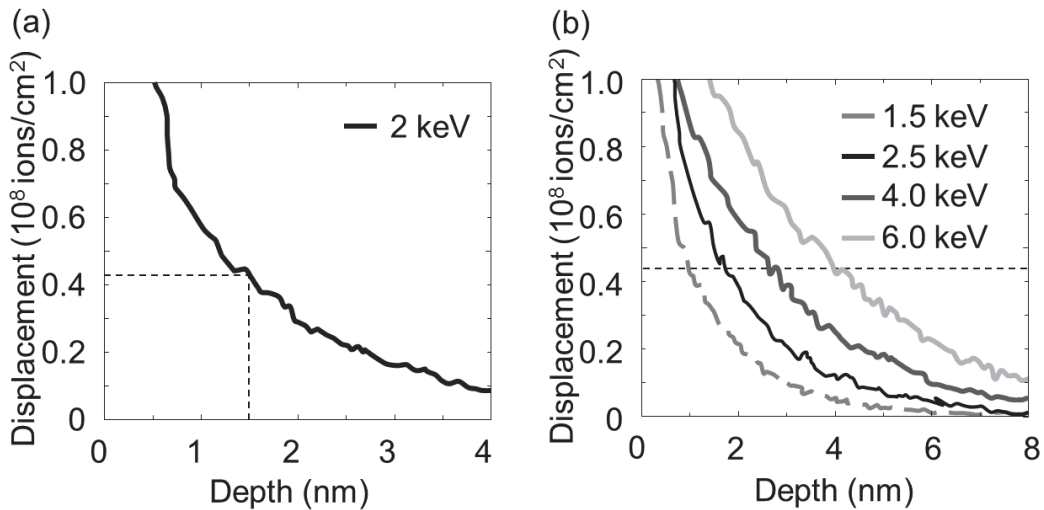


Figure 3-5. Results of Monte Carlo simulation to estimate amorphous thickness. The number of displacements generated by (a) 2.0-keV Ar^+ ion milling, and (b) 1.5, 2.5, 4.0, and 6.0 Ar^+ keV milling.

In the amorphous layer, many defects that strongly affect the electrical properties are created and the majority of dopants become electrically inactive [7]. As dopant contrast is produced by electrically active dopants [24], [25], dopants in the amorphous layer make little contribution to the contrast. For the quantitative discussion, the thickness of the ion-milling-generated amorphous layer was calculated using the Monte Carlo simulation package SRIM-2008 (Stopping and Range of Ions in Matter, ver. 2008), developed by J. F. Ziegler [26]. Figure 3-5 shows the results. The calculation conditions were optimized so that the calculation could replicate the TEM experimental results, i.e., an amorphous layer in

2.0-keV Ar⁺-ion-milling-prepared InP with a thickness of 1.5 nm [27]. Specifically, when the depth was 1.5 nm, the displacements were 0.43×10^8 ions/cm² (as shown in Fig. 3-5 (a)); therefore, the layer that included more displacements than 0.43×10^8 ions/cm² was defined as the amorphous layer. Then, the thicknesses of the amorphous layers generated by 1.5, 2.5, 4.0 and 6.0 keV milling were estimated to be 1.3, 1.7, 2.7, and 4.0 nm, respectively. These results indicate that the amorphous layer thickness can be controlled to an accuracy of approximately 1 nm using low-energy Ar⁺ ion milling.

3.5.3 Relationship between dopant contrast and amorphous layer thickness

Figure 3-6 shows the dependence of the dopant contrast on the calculated thickness of the amorphous layer generated by ion milling. From Fig. 3-6, a 1.3-nm-thick amorphous layer leads to contrast comparable to that of cleaved surfaces, even though the surface has been ion milled. This result indicates that the decrease in dopant contrast is caused by the generated amorphous layer, and dopant contrast equal to that of a cleaved surface can be obtained even when the surface is prepared using ion milling. In addition, the region from the surface to a depth of approximately 1 nm with a cleaved surface does not give rise to dopant contrast. This is attributed to surface oxidation and defects on the semiconductor surface.

The contrast values decreased from 20% to 16, 6, and 4% as the amorphous layer thickness was increased from 1.3 to 1.7, 2.7, and 4.0 nm, respectively. Therefore, when the amorphous layer thickness was at 4.0 nm, 16% of the contrast was lost compared to that from the surface with a 1.3-nm-thick amorphous layer. This indicates that 16% of the contrast was obtained within a depth range of 1.3–4.0 nm. Thus, the amorphous layer thickness should be reduced to approximately 1 nm if high-sensitivity 2D dopant profiling is to be achieved. However, 4% of the contrast was obtained from a depth of more than 4.0 nm, which suggests that both the primary electron beam penetration depth and the SE maximum escape depths are over 4.0 nm. This corresponds well with previous reports on the primary

electron beam penetration depth for an energy of 1 keV (19 nm) based on the equation [28]

$$R = \frac{0.0276 \times A E_0^{\frac{5}{3}}}{Z^9 \rho}, \dots \dots (3-1)$$

where R is the penetration depth, A is the atomic weight, E_0 is the primary beam energy, Z is the atomic number, and ρ is the density. Although there is no reference in the accurate maximum escape depth from InP, the maximum escape depths in metals and insulators are estimated to be 5 and 75 nm [29], respectively, which implies the depth from InP is also longer than 4.0 nm.

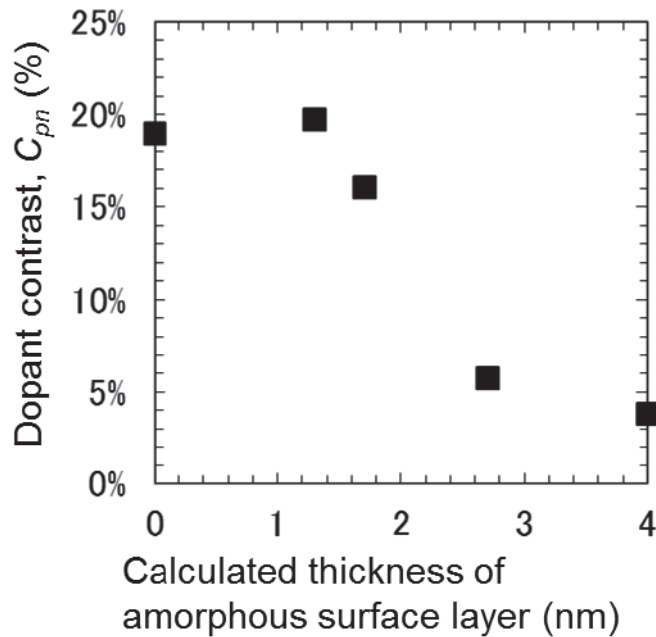


Fig. 3-6. Dependence of dopant contrast on calculated thickness of amorphous surface layer [1].

3.5.4 Contrast dependence on acceleration voltage

The discussion of Section 3.5.3 indicates that dopant contrast corresponding to that of a cleaved surface can be obtained from a sample milled under a high-energy ion beam, provided the primary electron beam penetrates to a sufficient depth. Then, the acceleration voltage of the primary beam is varied in the 0.6–3.0-kV range, and the effect on the contrast in each sample is observed. The penetration depths of an electron beam with energies of 0.6, 1, 2, and 3 kV are 8.2, 19, 61, and 120 nm, respectively. Figure 3-7 shows the obtained images.

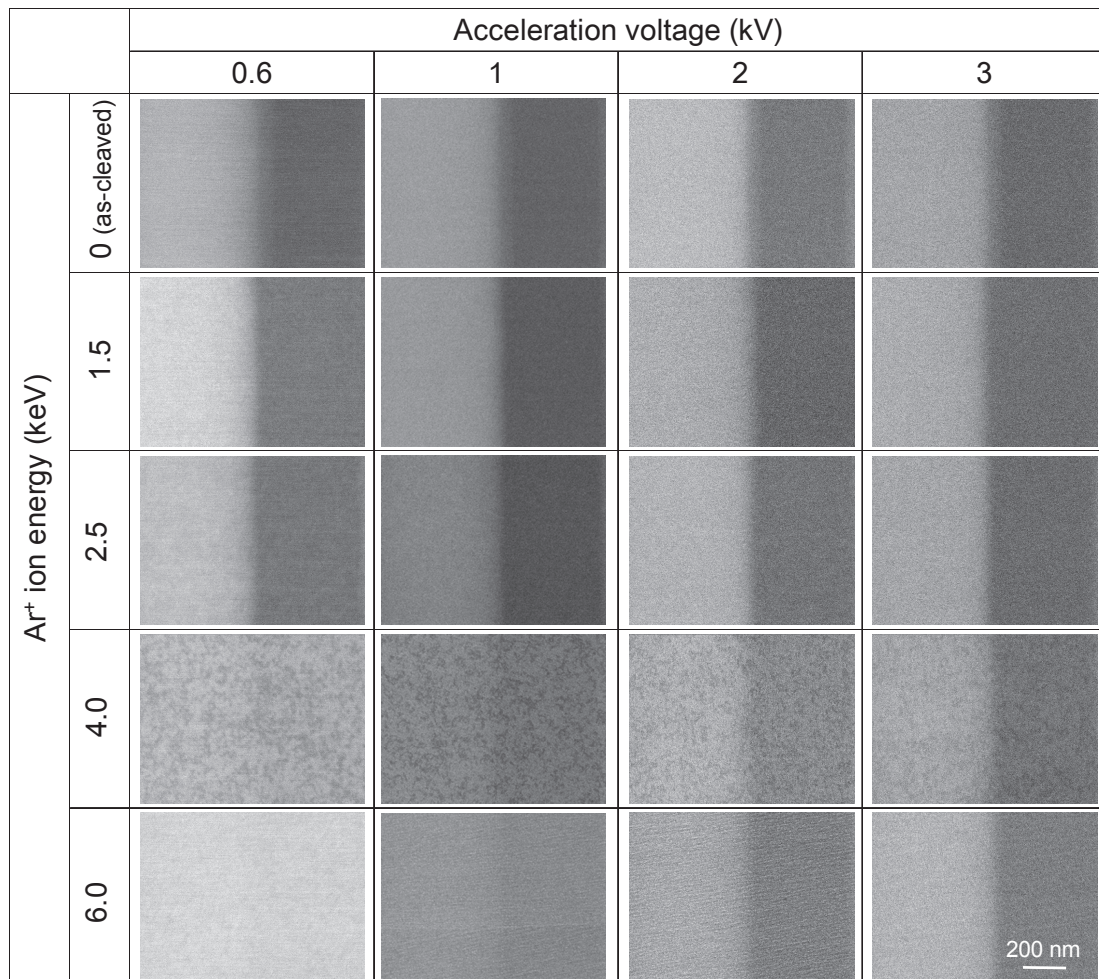


Fig. 3-7. Dopant contrast as a function of primary electron beam acceleration voltage and Ar⁺ ion milling energy.

Figure 3-7 shows that the dependence of the dopant contrast on the Ar^+ ion milling energy decreases as the primary electron beam acceleration voltage increases. Figure 3-8 shows a clarification of the relationship between the acceleration voltage and dopant contrast for each sample. In this figure, C_{pn} is normalized to the contrast from a cleaved surface. Dopant contrast corresponding to that of a cleaved surface is represented by the number 1. As the dopant contrast decreases, the normalized C_{pn} decreases, and the contrast disappearance is expressed as 0.

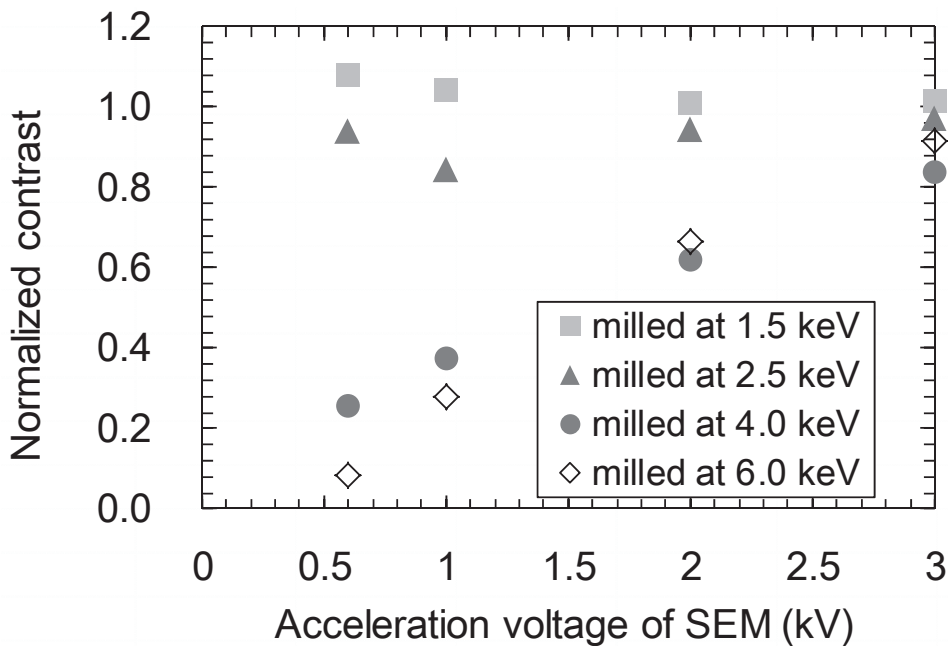


Fig. 3-8. Relationship between acceleration voltage and dopant contrast for each sample.

Figure 3-8 shows that the increasing acceleration voltage reduces the influence of the amorphous layer on dopant contrast. Although the dopant contrast was not observed from the surface milled at 6.0 keV with the acceleration voltage of 0.6 kV, it was observed with the same clarity as that of a cleaved surface at an acceleration voltage of 3.0 kV. This is because of the surface information decrease and the increased information from within the sample, due to the increase in the penetration depth of the primary electron beam. This indicates that SEM imaging with high

acceleration voltage enables dopant contrast observation even if the amorphous layer cannot be completely removed. However, increasing the acceleration voltage decreases the dopant contrast sensitivity [23], and therefore, reduction of the amorphous layer thickness is a basic requirement.

3.6 Discussion of dopant contrast mechanism

As described in Section 2.4.2, a number of dopant contrast theories have been suggested that are based on surfaces or interfaces, i.e., surface states and metal-semiconductor charging, and also external and internal electric fields. In this chapter, two experimental results were obtained. One is that the contrast values decrease as the thickness of the amorphous layer, which cancels out the built-in potential, is increased. The other is that SEM imaging with high acceleration voltage, which supplies sufficient penetration depth to the primary electron beam to generate SEs from single-crystalline InP, enables dopant contrast observation from a sample with a thick amorphous layer on the surface. These experimental results indicate that the contrast primarily arises from the external or internal electric field of the sample, which is the built-in potential, and that the surface and interface states do not strongly affect the contrast in this case.

3.7 Conclusions

In conclusion, highly sensitive 2D dopant profiling has been demonstrated in the secondary electron imaging of an InP sample prepared using low energy Ar⁺ ion milling for site-specific analysis.

For the cross-section preparation of the device analysis, a positional precision of less than 1 μm is required. The only technique that offers positional precision of less than 1 μm is ion milling. However, ion milling for the 2D dopant profiling of a compound semiconductor has two serious problems, namely, surface roughness and a decrease in dopant contrast.

The surface roughness problem was solved by cooling the sample. While surface roughness was observed on surfaces prepared using high-energy ion milling, smooth mirror-like surfaces were observed for the samples prepared using low-energy ion milling. The results indicate that the samples were cooled sufficiently to prevent In atom diffusion at the sample surfaces when low-energy ions were used.

The other problem was the decrease in dopant contrast. Attempts to reduce the thickness of the amorphous layer were made and a low-energy ion milling process was employed. As a result, it was demonstrated that the decrease in dopant contrast is caused by the generated amorphous layer, and dopant contrast as high as that of a cleaved surface was observed from a surface prepared using 1.5-keV milling; the amorphous layer thickness was calculated as 1.3 nm in this case. The results indicate that the amorphous layer thickness can be controlled to approximately 1 nm using low-energy Ar⁺ ion milling, and such a thin amorphous layer leads to contrast that is comparable to that obtained for cleaved surfaces, despite the fact that the surface is prepared using ion beam milling. In addition, it is indicated that SEM imaging with high acceleration voltage enables dopant contrast observation even if the amorphous layer cannot be removed completely. However, as the acceleration voltage increases, the dopant contrast sensitivity decreases and therefore, the amorphous layer must be removed.

Because the contrast is clearly seen in the case of InP, which is the most damage-labile material, it is expected that this technique can be widely applied to the other compound semiconductors (GaAs, GaN, SiC, etc.). Thus, the production of semiconductor cross-sections using low-energy Ar⁺ ion milling can provide sensitive site-specific 2D dopant profiling of compound semiconductors, and extend the application of SEM 2D dopant profiling to the examination of compound semiconductor device structures, for which site selection is essential.

At the end of this chapter, the dopant contrast mechanism was discussed. It was indicated that the contrast primarily arises from the external or internal electric field of the sample, and the surface and the interface states did not strongly affect the contrast in this case.

3.8 References

- [1] D. Tsurumi and K. Hamada, "Sensitive Site-Specific Dopant Mapping in Scanning Electron Microscopy on Specimens Prepared by Low Energy Ar⁺ Ion Milling," *Appl. Phys. Express*, vol. 6, no. 12, 126601, 2013.
- [2] K. Nikawa, C. Matsumoto, and S. Inoue, "Novel Method for Defect Detection in Al Stripes by Means of Laser Beam Heating and Detection of Changes in Electrical Resistance," *Jpn. J. Appl. Phys.*, vol. 34, no. Part 1, No. 5A, pp. 2260–2265, 1995.
- [3] B. Lambert, N. Labat, D. Carisetti, S. Karboyan, J. G. Tartarin, J. Thorpe, L. Brunel, A. Curutchet, N. Malbert, E. Latu-Romain, and M. Mermoux, "Evidence of relationship between mechanical stress and leakage current in AlGa_N/Ga_N transistor after storage test," *Microelectron. Reliab.*, vol. 52, no. 9–10, pp. 2184–2187, 2012.
- [4] E. Inuzuka and H. Suzuki, "Emission microscopy in semiconductor failure," in *Instrumentation and Measurement Technology Conference, 1994. IMTC/94. Conference Proceedings. 10th Anniversary. Advanced Technologies in I & M., 1994 IEEE*, 1994, pp. 1492–1496.
- [5] N. Thierry-Jebali, J. Hassan, M. Lazar, D. Planson, E. Bano, A. Henry, E. Janzén, and P. Brosselard, "Observation of the generation of stacking faults and active degradation measurements on off-axis and on-axis 4H-SiC PiN diodes," *Appl. Phys. Lett.*, vol. 101, no. 22, 222111, 2012.
- [6] C. Zeng, Y. Wang, X. Hong, P. Lai, Y. Huang, and Y. En, "Degradation characteristics and analysis of AlGa_N/Ga_N high electron mobility transistors under reverse gate bias step stress," in *Proceedings of the 20th IEEE International Symposium on the Physical and Failure Analysis of Integrated Circuits (IPFA)*, 2013, pp. 741–744.

- [7] P. Kazemian, A. C. Twitchett, C. J. Humphreys, and C. Rodenburg, "Site-specific dopant profiling in a scanning electron microscope using focused ion beam prepared specimens," *Appl. Phys. Lett.*, vol. 88, no. 21, 212110, 2006.
- [8] K. W. A. Chee, R. Beanland, P. A. Midgley, and C. J. Humphreys, "Site-selective dopant profiling of p-n junction specimens in the dual-beam FIB/SEM system," *J. Phys. Conf. Ser.*, vol. 209, 012069, 2010.
- [9] R. M. Langford and a. K. Petford-Long, "Broad ion beam milling of focused ion beam prepared transmission electron microscopy cross sections for high resolution electron microscopy," *J. Vac. Sci. Technol. A Vacuum, Surfaces, Film.*, vol. 19, no. 3, pp. 982, 2001.
- [10] M. A. E. Jepson, B. J. Inkson, R. Beanland, A. K. W. Chee, C. J. Humphreys, and C. Rodenburg, "Progress towards site-specific dopant profiling in the scanning electron microscope," *J. Phys. Conf. Ser.*, vol. 209, 012068, 2010.
- [11] L. A. Giannuzzi, R. Geurts, and J. Ringnalda, "2 keV Ga⁺ FIB Milling for Reducing Amorphous Damage in Silicon," *Microsc. Microanal.*, vol. 11, no. S02, pp. 828–829, 2005.
- [12] S. Rubanov and P. R. Munroe, "Damage in III – V Compounds during Focused Ion Beam Milling," *Microsc. Microanal.*, vol. 11, pp. 446–455, 2005.
- [13] O. Wada, "Ar ion-beam etching characteristics and damage production in InP," *J. Phys. D. Appl. Phys.*, vol. 17, no. 12, pp. 2429–2437, 1984.
- [14] J. Pearton, K. Chakrabarti, A. P. Perley, T. B. Laboratories, M. Hill, and K. S. Jones, "Ion milling damage in InP and GaAs," *J. Appl. Phys.*, vol. 68, no. 6, pp. 2760–2768, 1990.
- [15] Y. Homma, "Formation mechanism of indium microcrystals on ion-bombarded InP surfaces," *J. Surf. Anal.*, vol. 3, no. 3, pp. 641–645, 1997.

- [16] T. Ogiwara and Y. Homma, “Surface Damage of Compound Semiconductors by Ion Sputtering (in Japanese),” *表面科学*, vol. 25, no. 4, pp. 205–211, 2004.
- [17] T. Ogiwara and S. Tanuma, “InP/GaInAsP 多層膜における AES 深さ分解能の温度依存性 (in Japanese),” *J. Surf. Anal.*, vol. 1, pp. 227–232, 1995.
- [18] N. Bouadma, P. Devoldere, B. Jusserand, and P. Ossart, “Ion beam etching and surface characterization of indium phosphide,” *Appl. Phys. Lett.*, vol. 48, no. 19, pp. 1285–1287, 1986.
- [19] J. Kato, M. Nozu, Y. Fujimoto, M. Tanemura, and F. Okuyama, “Structure and morphology of microprotrusions grown on Ar⁺-sputtered InP,” *J. Vac. Sci. Technol. A*, vol. 13, no. 2, pp. 207–215, 1995.
- [20] D. Paramanik, T. T. Suzuki, N. Ikeda, Y. Sugimoto, T. Nagai, M. Takeguchi, and C. Van Haesendonck, “Fabrication of InP nano pillars by ECR Ar ion irradiation,” *arXiv*, 1104.1912, 2011.
- [21] D. Tsurumi, K. Hamada, and Y. Kawasaki, “Energy-filtered imaging in a scanning electron microscope for dopant contrast in InP.,” *J. Electron Microsc. (Tokyo)*, vol. 59 Suppl 1, pp. S183–S187, 2010.
- [22] D. Tsurumi, K. Hamada, and Y. Kawasaki, “Highly Reproducible Secondary Electron Imaging under Electron Irradiation Using High-Pass Energy Filtering in Low-Voltage Scanning Electron Microscopy,” *Microsc. Microanal.*, vol. 18, no. 02, pp. 385–389, 2012.
- [23] C. Sealy, M. Castell, and P. Wilshaw, “Mechanism for secondary electron dopant contrast in the SEM,” *J. Electron Microsc. (Tokyo)*, vol. 49, no. 2, pp. 311–321, 2000.
- [24] R. Turan and D. D. Perovic, “Mapping electrically active dopant profiles by field-emission scanning electron microscopy,” *Appl. Phys. Lett.*, vol. 69, no. 11, pp. 1593–1595, 1996.

- [25] M. R. Castell, D. a Muller, and P. M. Voyles, “Dopant mapping for the nanotechnology age.,” *Nat. Mater.*, vol. 2, no. 3, pp. 129–131, 2003.
- [26] J. Ziegler:, *SRIM - The Stopping and Range of Ions in Matter*. North Carolina, 2008.
- [27] K. Yabusaki and H. Sasaki, “Specimen Preparation Technique for a Microstructure Analysis Using the Focused Ion Beam Process,” *Furukawa Rev.*, vol. 22, pp. 1–6, 2002.
- [28] S. Okayama and K. Kanaya, “Penetration and energy-loss theory of electrons in solid targets,” *J. Phys. D Appl. Phys*, vol. 5, pp. 43–58, 1972.
- [29] H. Seiler, “Secondary electron emission in the scanning electron microscope,” *J. Appl. Phys.*, vol. 54, no. 11, pp. R1–R18, 1983.

Chapter 4

Development of Observation Technique

This chapter presents the development of an observation technique using energy-filtered imaging [1-3] which is an effective and reproducible method. Thus, this technique addresses the second problem faced by 2D dopant profiling introduced in Chapter 1: poor reproducibility.

4.1 Introduction

The 2D dopant profiling of semiconductor devices is an essential analysis technique for R&D and production, as explained in Chapter 1. Reproducibility is an important factor for any analysis technique, and particularly so in the case of 2D dopant profiling. This is because only a few samples exist for analysis and, therefore, no unnecessary errors can be tolerated. In addition, both reliability and a large number of data

measurements (including at the sample preparation stage) are required for the process characterization.

2D dopant profiling using SEM, which is rapid and therefore suitable for industrial use [4,5], is more reproducible compared to scanning probe microscopy (SPM), which makes contact with and damages the sample surface. However, some problems with SEM have been reported, including a reversal of contrast for Si samples with a thick oxide layer when different primary beam energies are used [6,7], and a decrease in contrast caused by the electron beam irradiation used in the SEM observation [8]. In particular, the problem of the decreased contrast due to the irradiation is a consistent difficulty and is, therefore, a major issue that must be overcome.

Typically, electron beam irradiation induces a contamination layer composed of hydrocarbon that is formed on the sample surface during SEM observation. According to Reimer [9], contamination is caused by the damage and polymerization of organic molecules in the irradiated area. The radiation damage of organic substances by ionization and excitation cannot be avoided and results in bond breakage and a loss of mass. Free bonds in neighboring molecules can react by cross-linking. Finally, an electron-irradiated organic sample consists of a polymerized carbon-enriched conglomerate. Irradiation using a stationary beam results in the build-up of a contamination cone at the irradiated spot [10,11], because organic molecules move on the sample surface by thermal diffusion and are pinned by radiation damage when the irradiation area is reached [9]. Normally, the sources of this contamination are the atmosphere, including grease and pumping oil in an SEM chamber.

Thus, the electron beam irradiation necessary for SEM observation generates a contamination layer, and this results in a darkening of the irradiated area and a decrease in the dopant contrast, as shown in Fig. 4-1. The reproducibility of the 2D dopant profiling method is then decreased and hence, this technique has not yet become widely employed in the semiconductor industry as a useful analytical method. In order for advanced analysis to be conducted using this technique, it is therefore essential that this problem be solved.

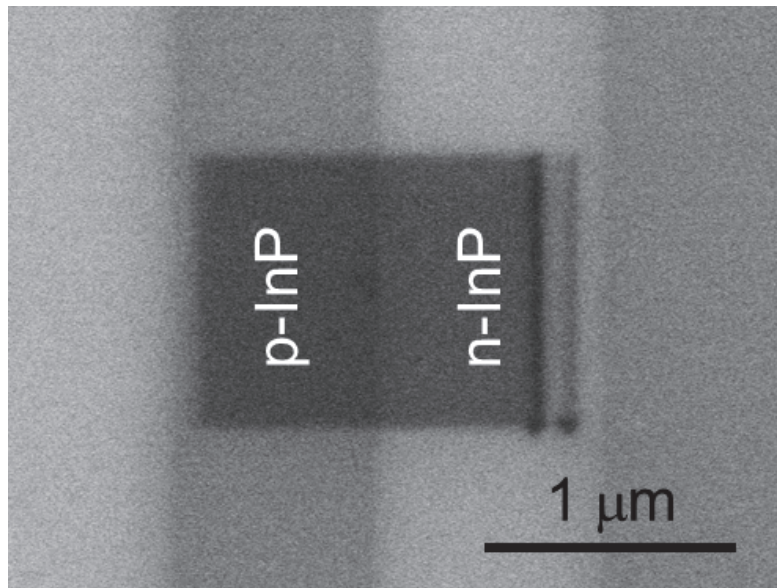


Fig. 4-1. SEM image of InP p-n junction. One scanned area is darker than the surrounding areas because of electron beam irradiation. As a result, the dopant contrast in the region is almost invisible.

4.2 Purpose

As indicated in the introduction above, the purpose of this part of the thesis is to investigate the 2D dopant profiling method so as to reduce the influence of electron beam irradiation on the imaging and to increase reproducibility.

4.3 Method

This section describes the observation method used in this part of the study and a description of the differences between this approach and those used in previous studies.

4.3.1 Samples

The sample examined here was an InP test structure grown using chemical vapor deposition. It consisted of a p-type layer (1×10^{18} Zn atoms cm^{-3}) on an n-type layer (1×10^{18} Si atoms cm^{-3}), as shown in Fig. 2-1 (a). The sample was cleaved in air prior to loading into the SEM chamber.

4.3.2 Observation method

In order to remove the influence of the electron beam irradiation, the application of SE energy-filtering (as discussed in Section 2.4) and reverse-bias voltage were attempted. The rationale behind the application of these methods is given below.

The electron beam irradiation, which generates a contamination layer, reduces not only the dopant contrast but also the surface topographic contrast. Therefore, a large number of approaches to solve this issue have been developed and evaluated. Table 4-1 contains a list of the main methods. Through an evaluation of these methods from the standpoint of both efficacy and usability, it was concluded that SE energy-filtering is the method with the greatest potential.

First, the method that aims to reduce the contamination layer formation by decreasing the irradiation current could not be used practically, because of the resultant decrease in the signal to noise ratio. Secondly, the use of a cold trap to adsorb the hydrocarbon was not sufficiently effective. It is reported that sample cooling or heating is an effective method that can reduce the influence of the contamination layer [9]. However, this method is time-consuming and, therefore, removes the SEM advantage of rapid data measurement. In addition, the recently developed method that removes the contamination layer using a plasma cleaner [12] was not sufficiently effective.

Thus, it was determined that these conventional methods were unable to reduce the influence of the irradiation without being overly time consuming. As a result, an experiment aiming to reduce the irradiation

effect using the SE energy-filtering method was initiated. This idea is based on the recent development of the SEM energy-filtering function. The results and a sample application are shown in Sections 4.4 and 4.5.

Table 4-1. Techniques to reduce the contamination effect [9].

Method	Effect	Usability
Low irradiation current	Low (contrast decreases)	High
Cold trap	Low	High
Sample heating or cooling	Unknown	Low
Plasma cleaner	Low	High
Energy filtering	Unknown	High

Table 4-2. Approaches to increasing the contrast.

Method	Effect	Usability
Changing the detector position [13]	Low	Low
Applying a reverse-bias voltage [14]	High	Low

Table 4-2 shows methods used to increase the contrast. When the contrast is increased, there is a relative decrease in the influence of the irradiation. In this study, a reverse-bias voltage was applied to achieve this

contrast increase, because it has the most potent effect. The effect of this method on the contrast is discussed in Section 4.6.

SEM images were collected on a through-the-lens (TTL) detector in a Hitachi S-4800 FE-SEM, which enables the generation of high-pass energy-filtered images, as explained in Section 2.4. The images were taken using an acceleration voltage of 1.0 kV and a working distance of 2 mm.

4.4 Energy filtering results and discussion

In this section, the SE energy distributions from p- and n-layers of InP are obtained. It is demonstrated that low and high energy SEs are strongly and weakly influenced by the irradiation, respectively. Then, the SE energy filtered imaging's ability to reduce the irradiation effect is shown. The mechanism through which the irradiation decreases the SE intensity is also discussed.

4.4.1 Observation of SE energy distribution

In order to investigate the main factor that causes the decrease in contrast as a result of irradiation, the SE energy distributions of cleaved and irradiated surfaces were observed. The SE energy distributions were obtained using SEM intensities and as a function of V_c . The experimental SE distributions were obtained by differentiating the total signal intensity with respect to V_c , as shown in 2.4.

Figures 4-2 and 4-3 show the SEM images and the intensity profiles from the p- and n-type regions of the filtered images as a function of V_c for cleaved and irradiated surfaces, respectively. Irradiated surfaces were prepared by SEM observation in advance. The same contrast and brightness settings were used for all images.

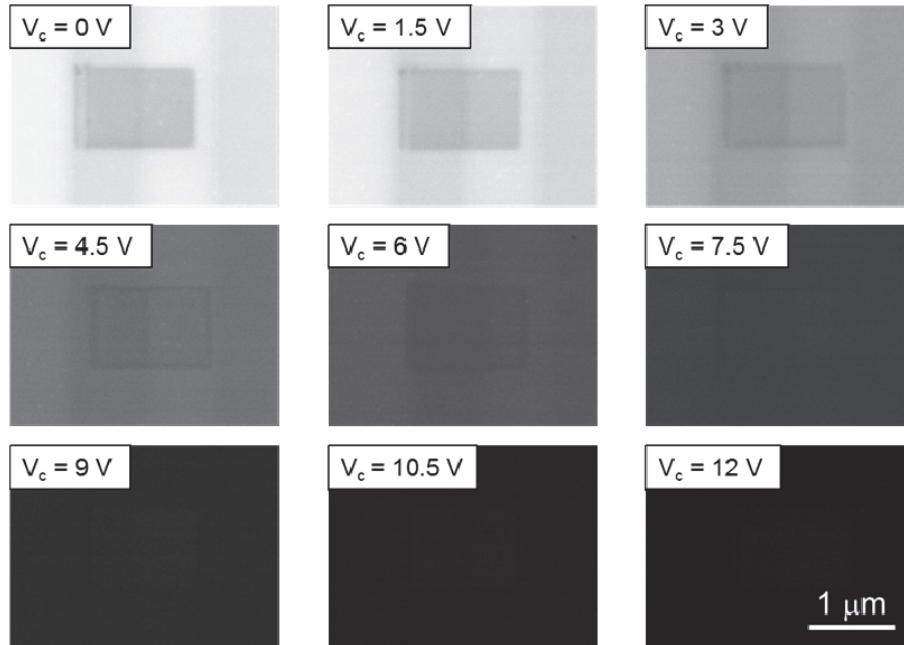


Fig. 4-2. SEM images of p- and n-type regions of filtered images at various V_c , for cleaved and irradiated (darkened region at the center) surfaces.

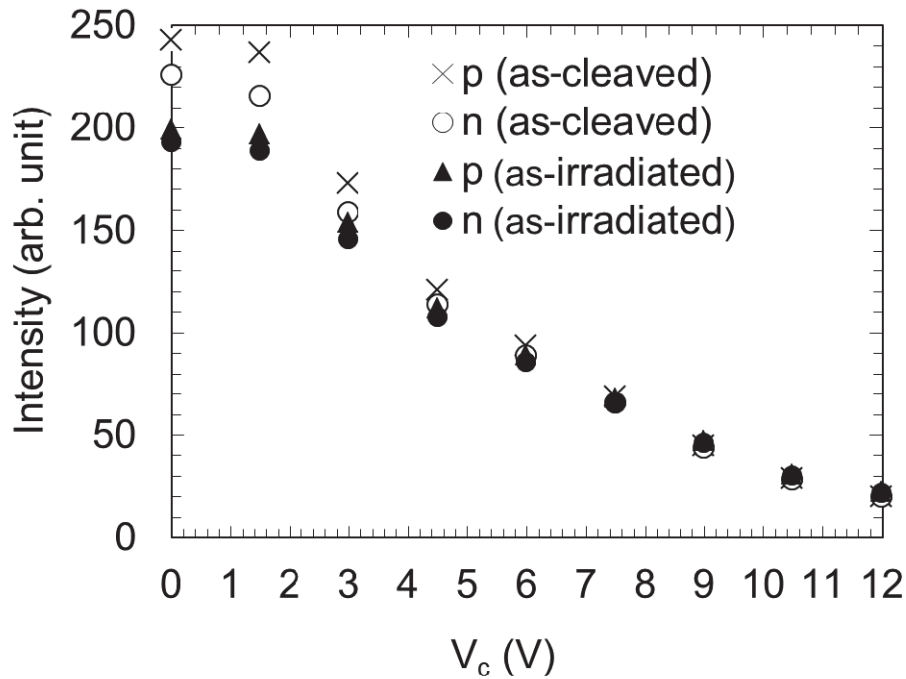


Fig. 4-3. SE intensity profiles of p- and n-type regions of filtered images (shown in Fig. 4-2) for various V_c for cleaved and irradiated surfaces [1].

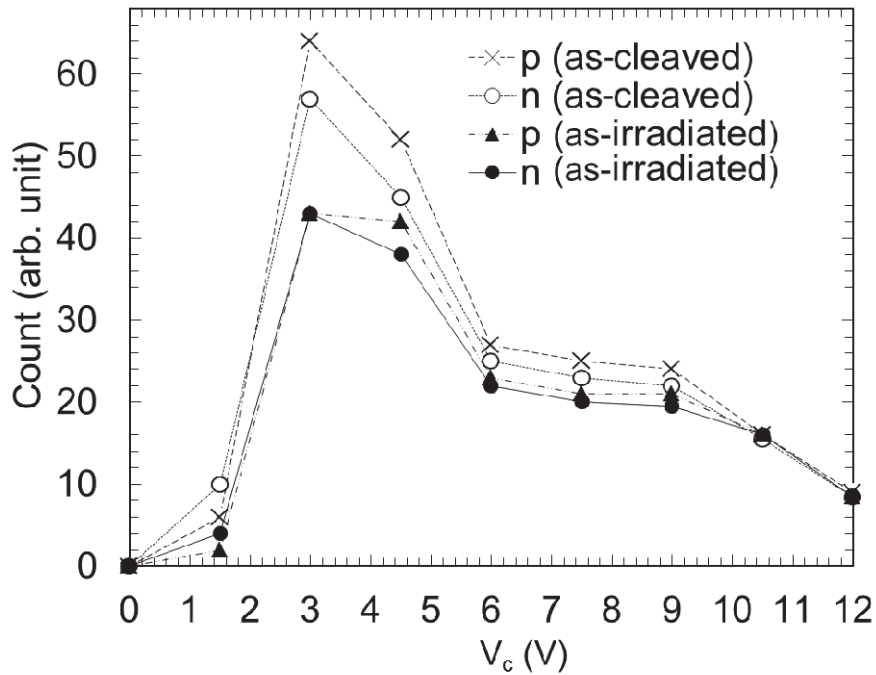


Fig. 4-4. SE energy distributions obtained by differentiating the total signal intensity with respect to V_c , for data shown in Fig. 4-3 [1,2].

Figure 4-4 shows the SE energy distribution obtained by differentiating the total signal intensity with respect to V_c for the data shown in Fig. 4-3. The results indicate that the total SE emission yield decreases due to the irradiation. In addition, it is clearly seen that the contrast (intensity difference) between the p- and n-type regions is obtained in the $3 \text{ V} \leq V_c \leq 7 \text{ V}$ range in particular.

Figure 4-5 shows the dependence of the signal change rate (C_{ir}/C_{as}) on the SE energy obtained through the SEM observation, where C_{ir} and C_{as} are experimental SE distribution counts (Fig.4-4) from the irradiated and as-cleaved surfaces, respectively.

Figure 4-5 shows that the lower energy SE emissions, especially in the $V_c = 0-3 \text{ V}$ range of the p-type region, decreased by ca. 90% after the SEM observation, while those of the n-type region decreased by ca. 30%. In contrast, the SE emissions that caused dopant contrast (in the $V_c = 3-7 \text{ V}$ range) were decreased by ca. 20% in both the p- and n-type regions.

Therefore, higher energy SEs are not significantly influenced by the irradiation caused by the SEM observation.

These results indicate that it is possible to reduce the irradiation effect through the use of SE energy filtering, while dopant contrast is expected to remain stable during SEM observation. Therefore, the effect of SE energy filtering was further investigated.

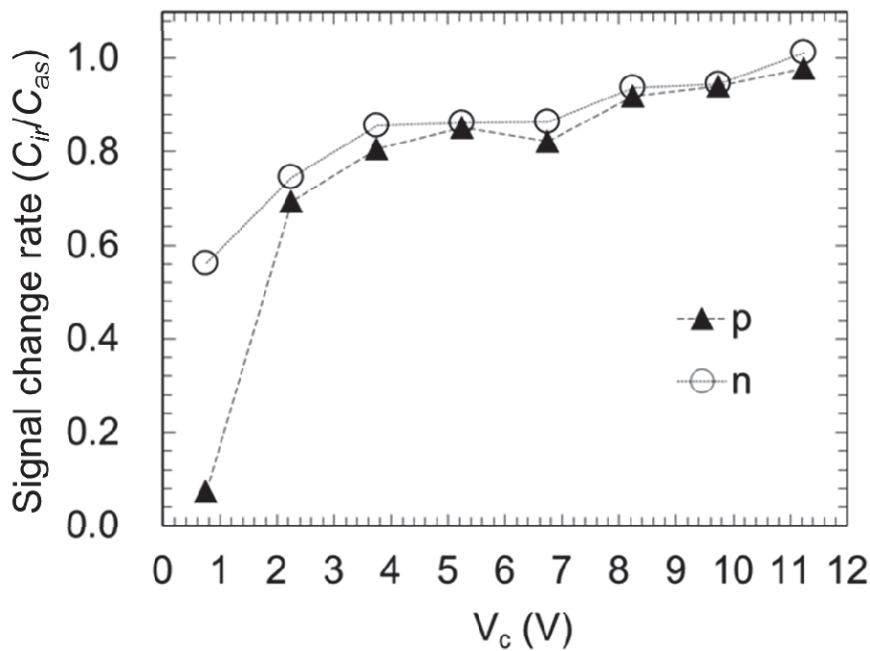


Fig. 4-5. Dependence of signal change rate (C_{ir}/C_{as}) on the SE energy due to the SEM observation [2].

4.4.2 Discussion of electron-beam-irradiation-induced SE intensity reduction mechanism

The mechanism involved in the irradiation effect can be explained on the basis of surface charging. To characterize the charge state of the

irradiated surfaces, C_{pn} was determined both before and after exposure to air.

Since air contains many free electrons, a charged sample loses its charge when exposed to air. One example of an integrated circuit (IC) package is shown in Fig. 4-6. Electron beam irradiation induces charging of the sample surface and the abnormal contrast and distortion can be seen in Fig. 4-6 (a). However, when the sample was exposed to air, these charging-induced artifacts were removed and the actual configuration could be observed, as shown in Fig. 4-6 (b). Thus, air exposure is an effective technique for removing the influence of charging on the sample and, therefore, this approach was used to examine the charge state of the irradiated surface.

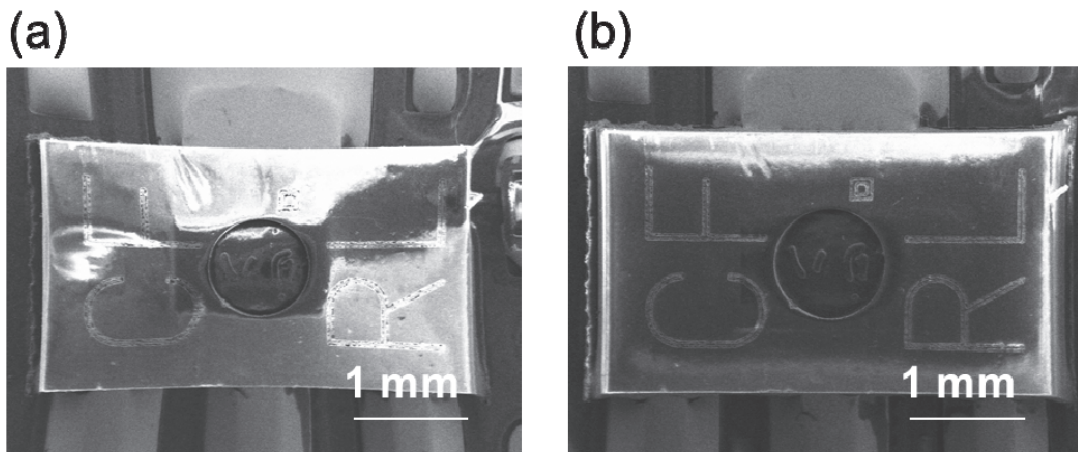


Figure 4-6. Unfiltered SEM images of an electron-beam-irradiated IC package, (a) before and (b) after exposure to air.

The p-n regions of a cleaved sample were intentionally irradiated with an electron beam, as described above. Then, the sample was exposed to air and reloaded into the SEM chamber, and an unfiltered image of the irradiated surface was obtained. A second unfiltered image of the irradiated area under the same conditions was obtained, but before exposure to air. These two images were obtained at the same contrast and brightness settings.

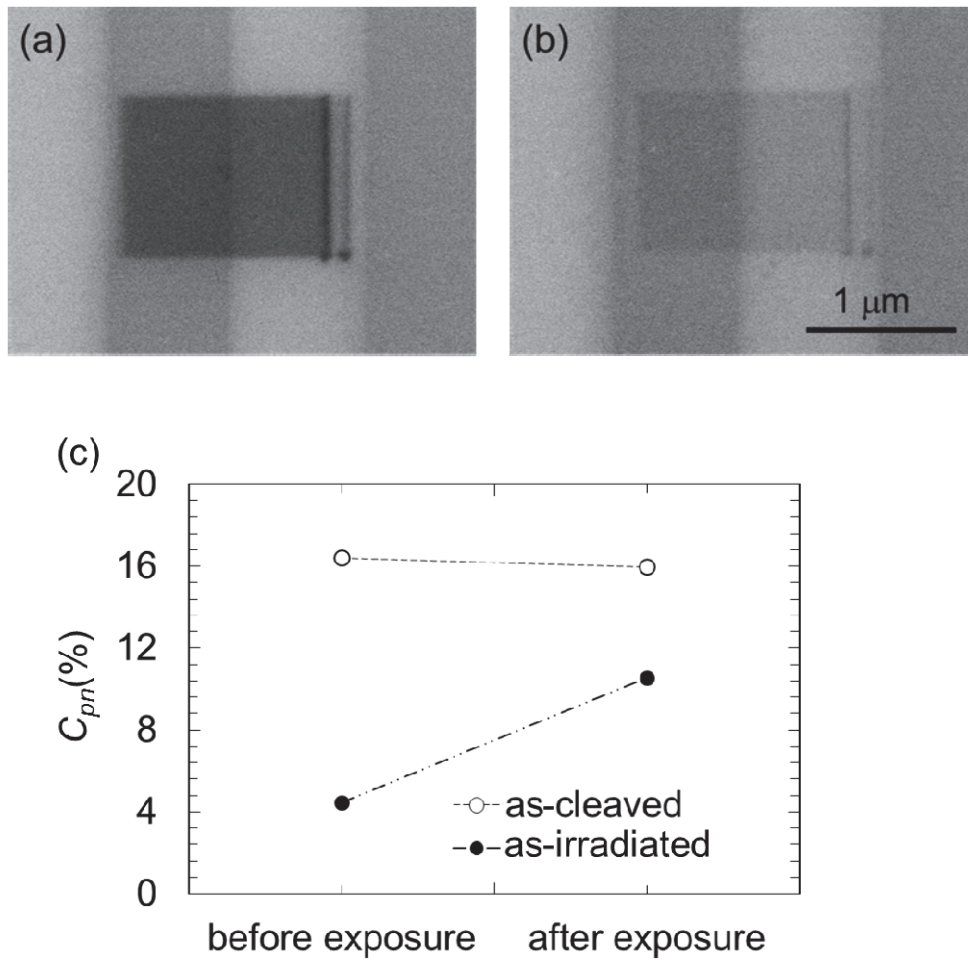


Fig. 4-7. Unfiltered SEM images of cleaved and irradiated surfaces, (a) before and (b) after exposure to air. (c) Quantified contrast (C_{pn}) of these regions [2].

Figure 4-7 shows the images and C_{pn} values, both before and after exposure to air. The C_{pn} of the irradiated surface before air exposure was less than 5% and almost no contrast was visible. In contrast, the C_{pn} after the air exposure was over 10%, and a clear contrast was observed. Therefore, the decrease in the SE emissions was due to a charging effect.

The obtained SE energy distributions in Fig. 4-8 also indicated that the decrease in contrast was due to surface charging. Figure 4-8 (a) shows an unfiltered image of an insulating dust particle on a silicon substrate. The

primary beam voltage was 15 kV with 2,000X magnification at a working distance of 15.0 mm. In this case, the dust particle was negatively charged, which induced a positive surface charge around the particle, as shown in Fig 4-8 (b) [9].

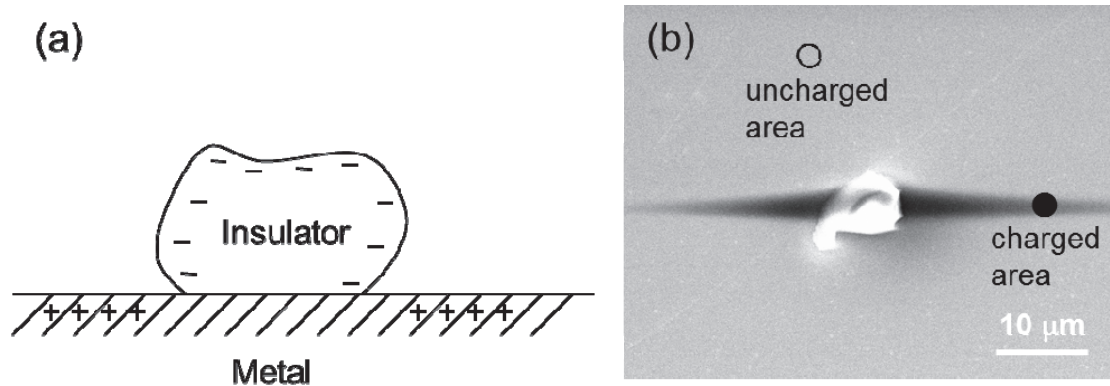


Fig. 4-8. (a) Negative charging of dust particle on silicon substrate and induced surrounding positive charge [9]. This results in (b) a dark area in a SE-unfiltered image [1,2].

SE distributions of the charged and uncharged areas were experimentally obtained using the intensity profiles of high-pass energy-filtered images, as shown in Fig. 4-9. These distributions indicated that the low-energy SE emissions from the positively charged surface were strongly reduced compared to those from the uncharged surface. This was because the positively charged layer trapped some of the low-energy SE emissions, but high-energy SEs were unaffected by the charge. Similarly, the SE distribution over an electron-beam-irradiated surface, shown in Fig. 4-4, indicated reduced low-energy SE emissions. Therefore, it was determined that the irradiated surface, which includes a contamination layer, a native oxide layer, and/or these interfaces, was positively charged.

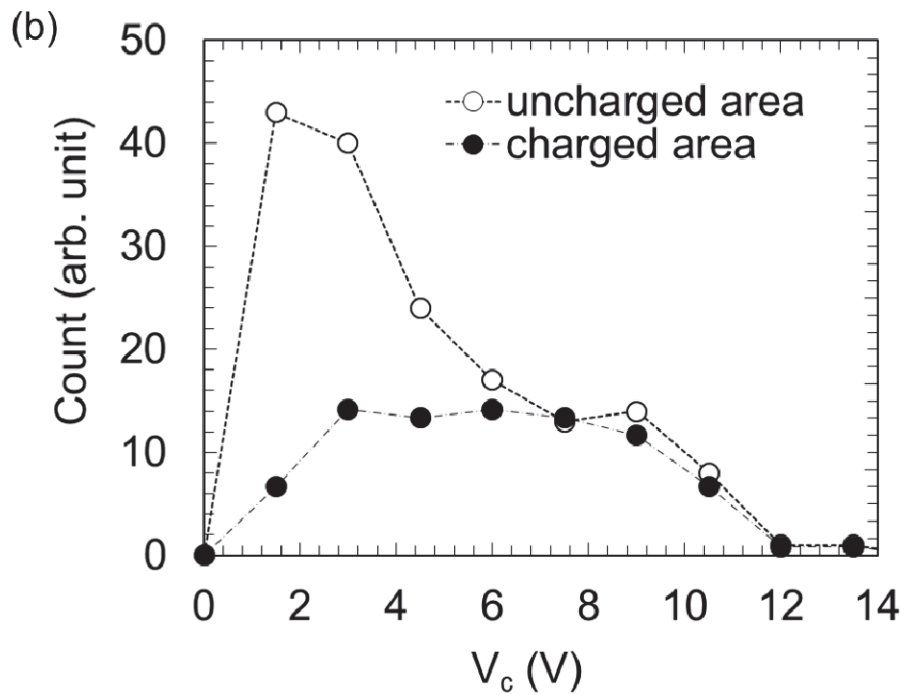
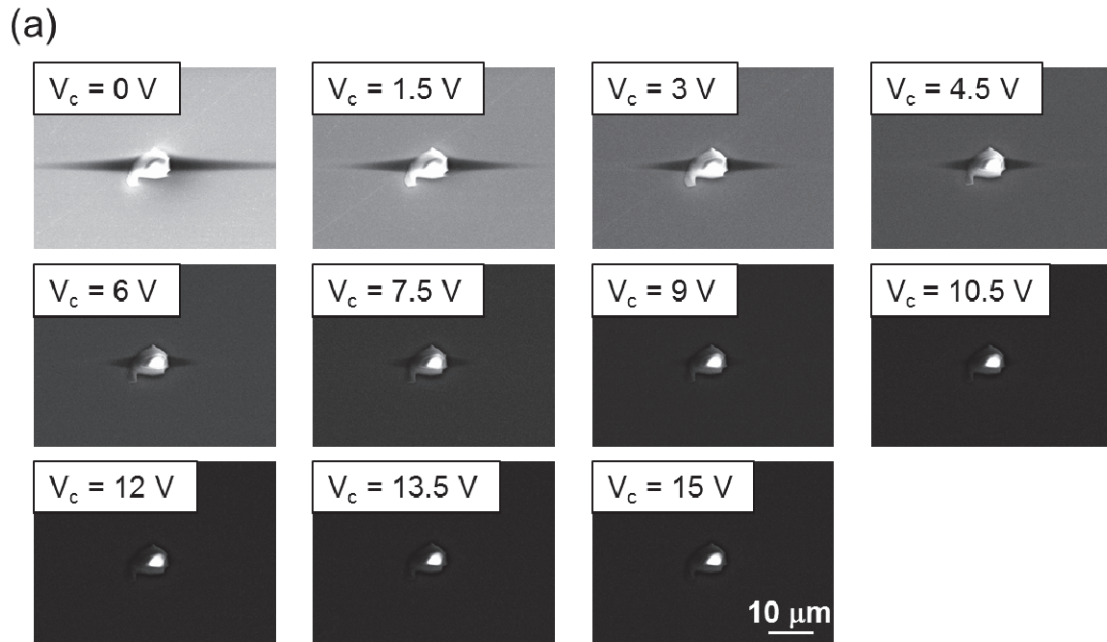


Fig. 4-9. (a) High-pass energy-filtered images of dust particle on silicon substrate in $0\text{ V} \leq V_c \leq 15\text{ V}$ range, and (b) SE energy distribution obtained from these SE images [9].

However, the C_{pn} after exposure to air was still 10%, which was 6% less than the C_{pn} of the cleaved surface, as shown in Fig. 4-7. This difference in contrast may be explained by two models.

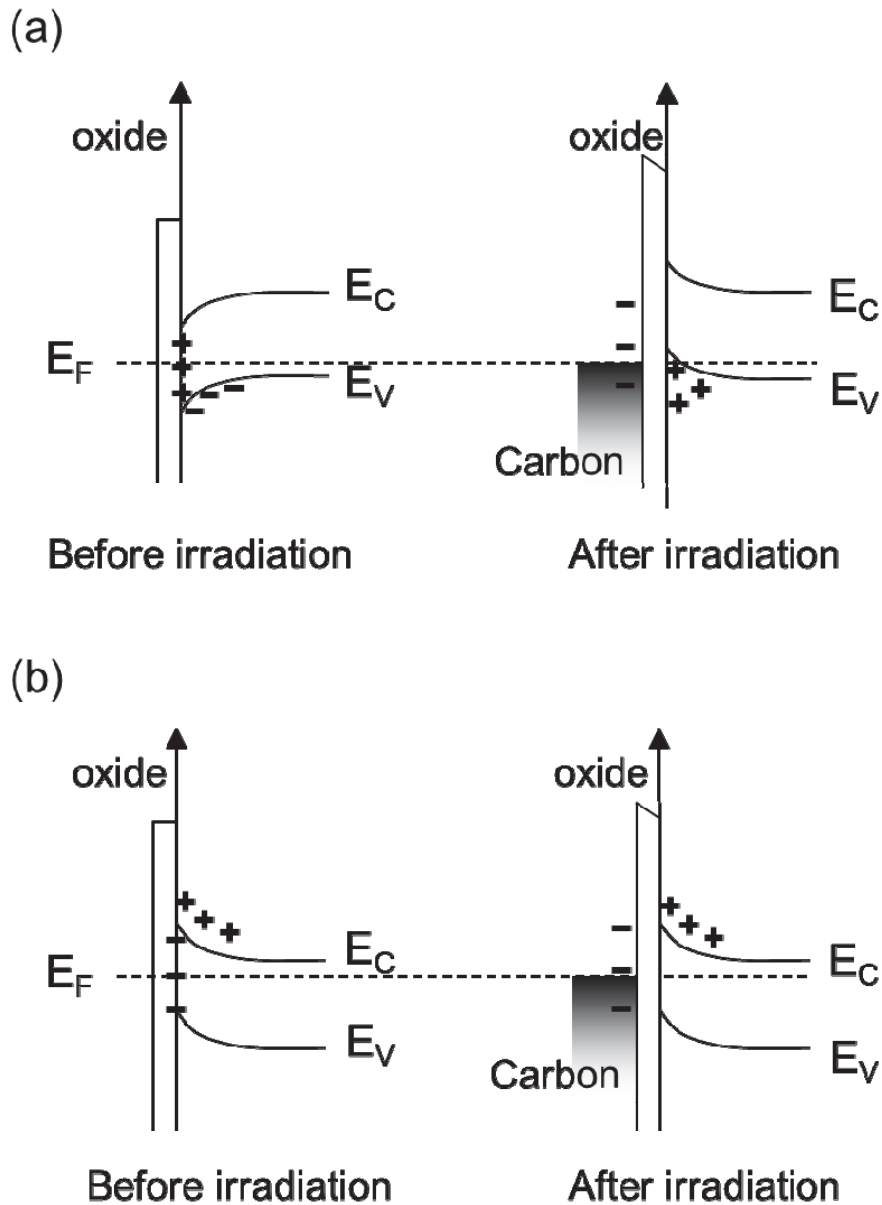


Fig. 4-10. Energy band diagram of metal to semiconductor, for a metal with a work function greater than that of the semiconductor. (a) p-type and (b) n-type regions [1].

The first model is based on the decrease in SE emission from an InP sample due to a surface contamination layer. Because the surface is covered by a contamination layer, the amount of primary electron beam energy that is irradiated into the InP sample decreases. This leads to a decrease in the SE generation and emission from the sample, and the dopant contrast is therefore decreased.

The other model focuses on a metal–semiconductor charge (the so-called Schottky barrier) [8,15–17], which is not neutralized when exposed to air. This metal-semiconductor charging model assumes that the contamination layer is a graphitic carbon. Since graphite is metallic, this suggests that the resulting contrast is due to a metal-semiconductor contact. The work function of graphite is approximately 5.1 eV [18], while that of InP is in the region of 4.6 eV [19]. Here, a thin native oxide layer is considered to exist between the contamination layer and the InP surface [20]. The Fermi levels are aligned in both metals and semiconductors, and the bands bend upwards. Therefore, positively charged surface states appear on the semiconductor side for both p-type and n-type regions, as shown in Fig. 4-10. This layer acts to recollect some of the emitted low energy SEs and also functions as a potential barrier for the SE emission from the InP sample, although high-energy SEs can pass through this layer. This leads to a decrease in the low-energy SE yield and in the dopant contrast in the $V_c = 0\text{--}4.5$ V range. Since energy-filtered imaging does not collect low-energy SEs, it can substantially reduce the effect of the charged layer, especially in the p-type region.

The charging models described above may be one of the factors that give rise to the reversal of the SE contrast, as a result of different electron beam currents and voltages used, along with the effect of the scan rate as discussed by El-Gomati *et al.*[5]. Further work should be being conducted to confirm this interpretation.

4.4.3 Energy-filtering effect on electron beam irradiation

Figure 4-11 shows unfiltered ($V_c = 0$ V) and filtered ($V_c = 1.5$, 3.0, and 4.5 V) SE images of a p-n junction at 20,000X magnification. To investigate the filtering effect, the dopant contrast was observed as a function of the SEM observation time, t . The contrast and brightness settings in each detection mode were adjusted so that the contrast was clearly observed at $t = 1$ s, and images at $t = 2-80$ s were acquired at the same settings.

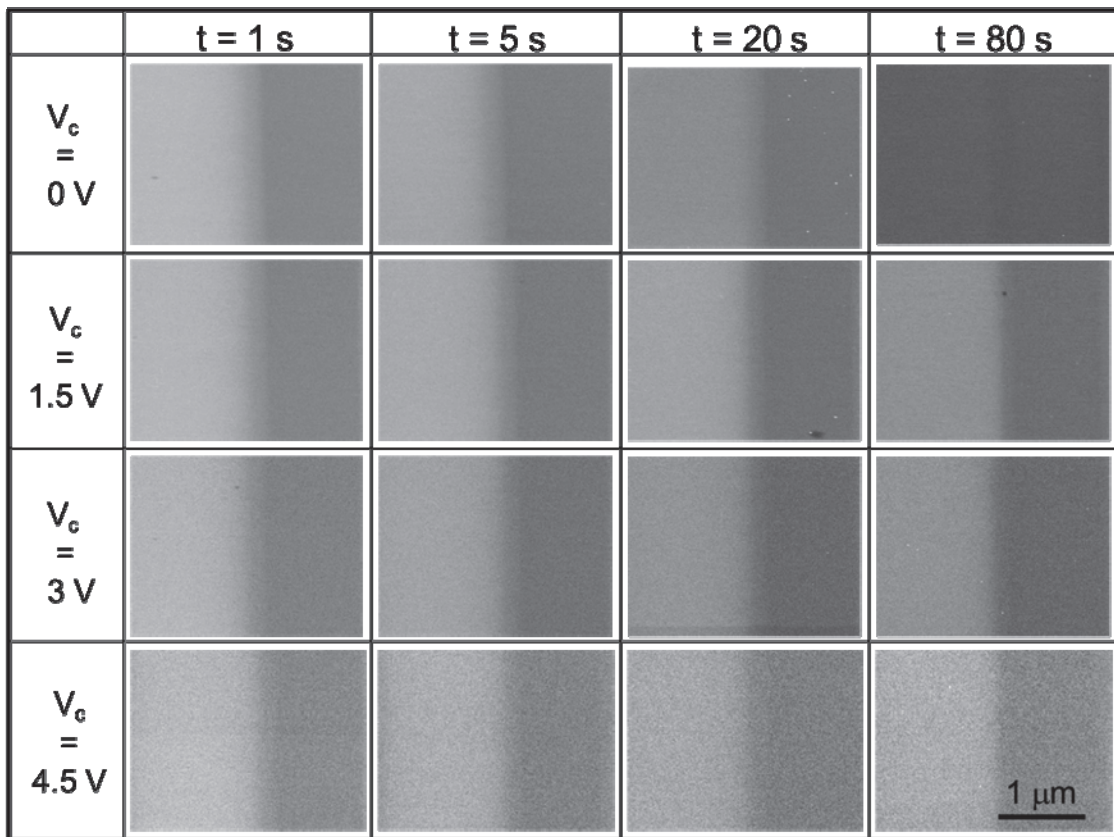


Fig. 4-11. Unfiltered ($V_c = 0$ V) and filtered ($V_c = 1.5$, 3.0, and 4.5 V) SE images of a p-n junction at 20,000X magnification as a function of SEM observation time, t .

Figure 4-12 shows the normalized C_{pn} as a function of SEM observation time. The data were normalized to $t = 1$ s in order to clarify the change in C_{pn} . Figures 4-11 and 4-12 show that the contrast after 1-s SEM observation was clearly observable in all the detection modes. However, in the unfiltered image, the contrast decreased with increased observation time. Finally, after 80 s, the value of C_{pn} fell below 0.1, and no contrast was observed. This decrease in contrast was caused by the irradiation that occurs during SEM observation.

However, the C_{pn} for energy-filtered images at $V_c = 1.5$ V fluctuated between 1.15 ($t = 10$ s) and 0.89 ($t = 80$ s). This was because the lower the SE energy, the stronger the influence of the irradiation as shown in Section 4.4.1. The filtered image at $V_c = 1.5$ V indicated lower SEs and, therefore, the contrast became unstable.

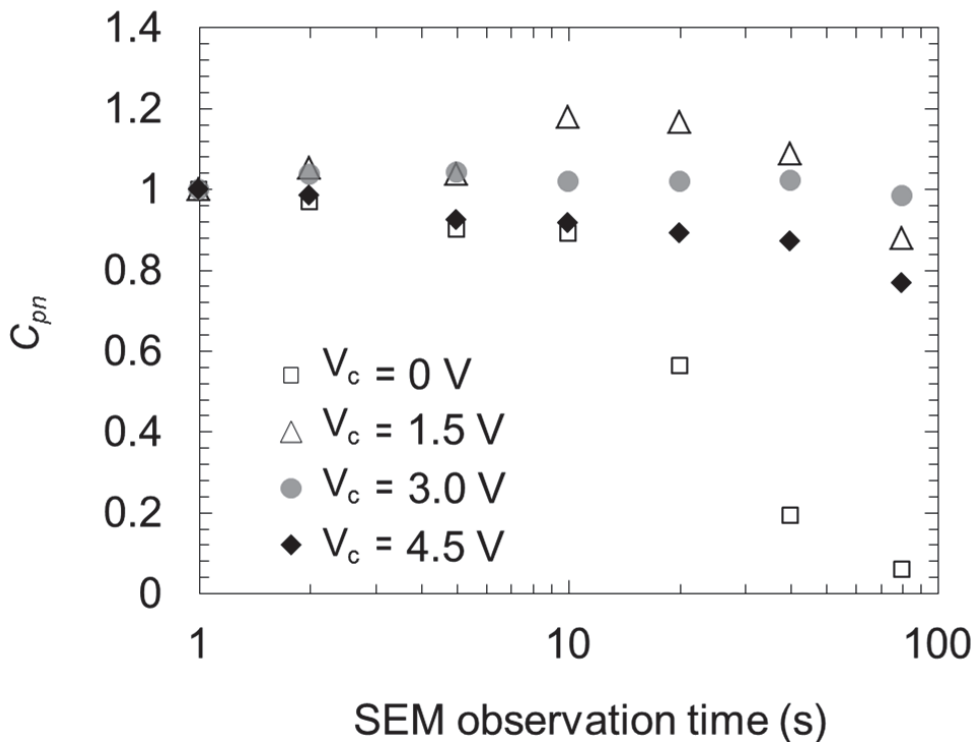


Fig. 4-12. Normalized contrast profiles (C_{pn}) as a function of SEM observation time [2].

In addition, there was a gradual decrease to 0.79 ($t = 80$ s) when $V_c = 4.5$ V. This is because the SE energy causing the dopant contrast was in the $V_c = 3\text{--}6$ V range, as discussed in Section 4.4.1. The filtered image at $V_c = 4.5$ V provided less dopant contrast information and, therefore, a higher contrast setting was required for energy-filtered images at $V_c = 4.5$ V compared to that for images recorded at $V_c = 3$ V to obtain the same contrast images. As a result, the energy-filtered imaging conducted at $V_c = 4.5$ V was more sensitive to noise, such as from the contamination layer, and a gradual decrease in C_{pn} was observed.

Thus, filtered imaging, especially at $V_c = 3$ V, can reduce the decrease in dopant contrast that occurs during SEM observation, by removing low-energy SEs that are strongly affected by surface contamination.

4.5 Application of energy-filtered imaging to reduce effects of electron beam irradiation

This energy-filtered imaging method can be widely used for samples in which the SE intensities decrease under continuous electron beam irradiation in the case of unfiltered SE images.

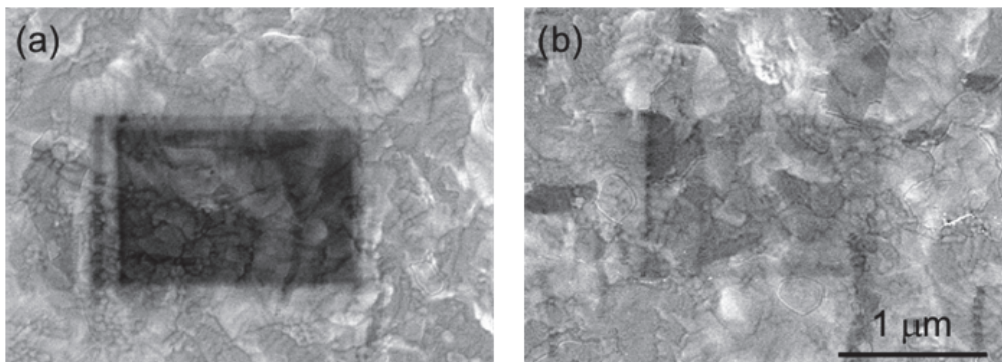


Fig. 4-13. SE images of gold surface: (a) unfiltered SE image at $V_c = 0$ V and (b) energy-filtered SE image at $V_c = 3$ V [2].

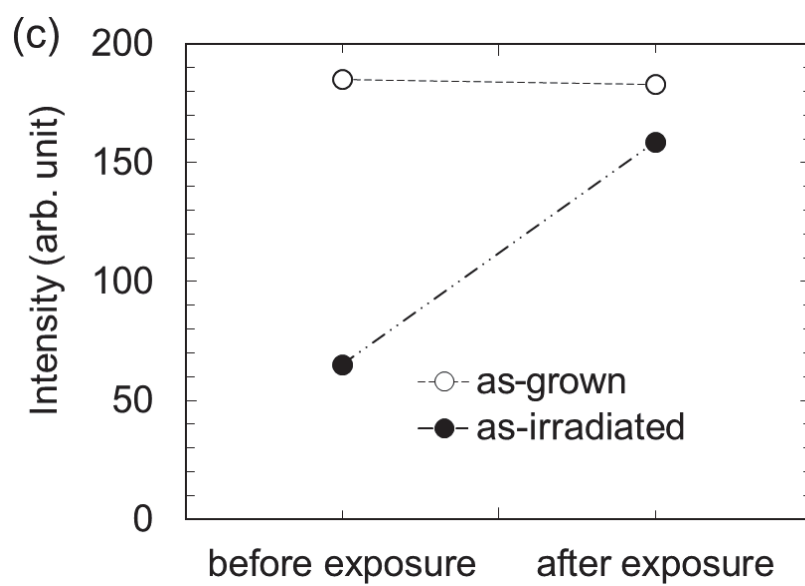
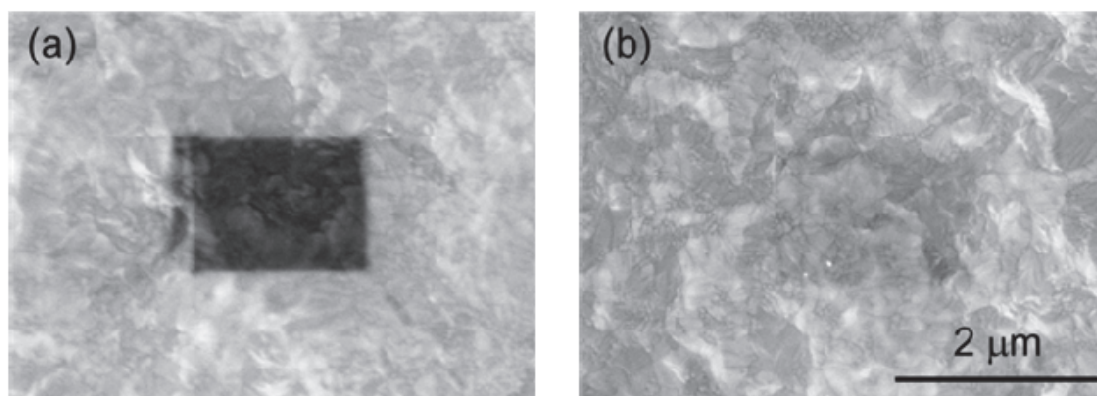


Figure 4-14 (a) Unfiltered SEM image, (b) filtered SEM image, and (c) intensities of as-grown and electron-beam-irradiated surfaces before and after exposure to air [2].

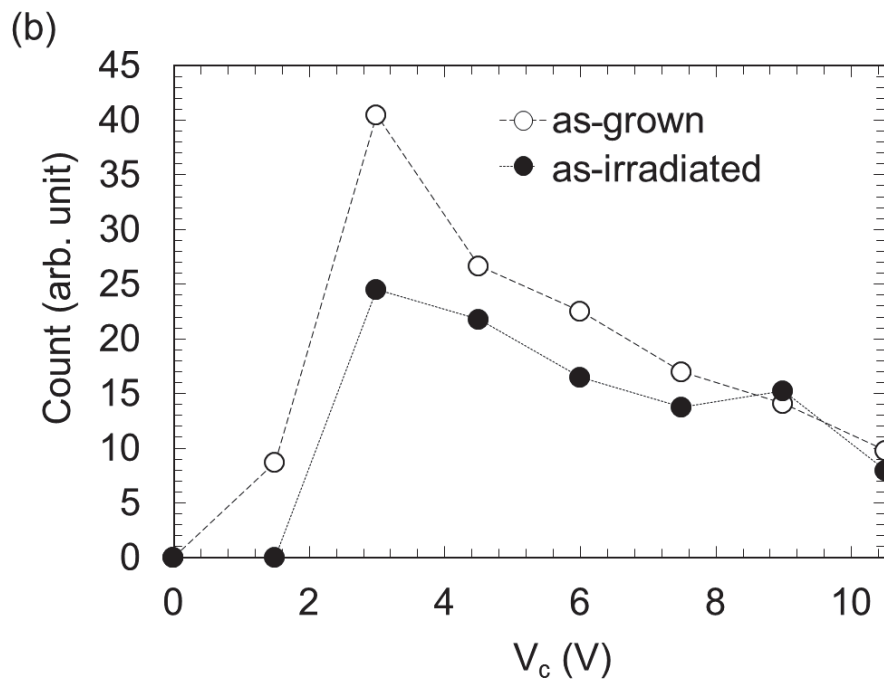
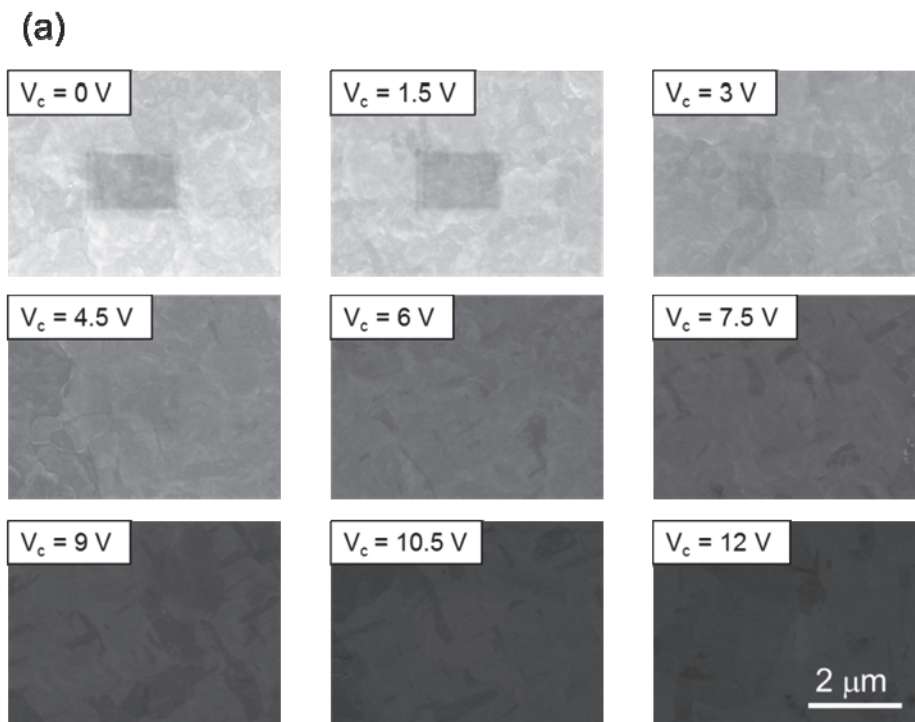


Figure 4-15 (a) High-pass energy-filtered images of gold surface in $0 \text{ V} \leq V_c \leq 15 \text{ V}$ range and (b) the SE energy distribution obtained from these SE images [2].

As an example, contrast retention was also observed in high-pass energy-filtered images of a gold surface, while the contrast decreased rapidly in the unfiltered images. Figure 4-13 shows these unfiltered and energy-filtered SE images of the gold surface. The gold surface was intentionally irradiated by the electron beam at 80,000X magnification, using the same method as that for the p-n junction described above. As shown in Fig. 4-13, it was obvious that the effect of the irradiation on the observed SE intensity was dramatically reduced through the application of SE energy-filtered imaging.

Charge neutralization (Fig. 4-14) and the SE energy distributions (Fig. 4-15) also indicated that the electron beam irradiation induces a positive charge.

Figure 4-14 shows SEM images of the gold surface and the intensities before and after air exposure. The intensity of the irradiated surface before exposure to air was 65, and was significantly darker than the other area. In contrast, the intensity after air exposure was over 150, and the surface configuration could be clearly observed.

Figure 4-15(b) shows the experimental SE distributions of the irradiated and clean gold surfaces obtained using the intensity profiles of the high-pass energy-filtered images shown in Fig.4-15(a). These distributions indicated that the low-energy SE emissions from the irradiated surface were strongly reduced, compared to those from the clean surface. This SE distribution is also similar to that of the positively charged area, as shown in Fig. 4-11, and the intensity after air exposure, as shown in Fig. 4-14. Therefore, it is deemed that the electron beam irradiation also induces a positive charge and the energy-filtered imaging can reduce the influence.

Thus, contrast retention was also observed in high-pass energy-filtered images of a gold surface. Therefore, these results suggest that this imaging method can be widely used for samples when the SE intensities decrease under continuous electron irradiation in unfiltered SE images.

Here, the electric state of the contamination layer becomes a problem. In Section 4.4.2, this layer was assumed to be graphite, following previous studies [15–17]. However, these experimental results imply that the contamination layer is insulating, as charging occurs for insulating

materials only. Therefore, reconsideration of the metal-semiconductor charging model may be required.

4.6 Effect of reverse-bias voltage application

In this section, the effect of applying a reverse-bias voltage, as discussed in Section 4.1 (Table 4-2), is considered. First, the importance of high magnification imaging of over 50,000X (scanned field area: $2.6 \times 2 \mu\text{m}^2$) for compound semiconductor devices is shown. Then, it is demonstrated that the contrast can be observed clearly, even under high-magnification conditions at which the electron-beam-irradiation effect is typically increased, by simultaneously applying SE energy filtering and a reverse-bias voltage.

4.6.1 Imaging demands at high magnification

As described above, SE energy filtering has been demonstrated as an effective method for reducing the decrease in dopant contrast during continuous SEM observation. The use of energy-filtered SEM to determine dopant distribution is an attractive approach that can meet the demand for an accurate and reproducible 2D dopant profiling technique.

In addition, nano-scale observation can be achieved using SEM. For example, Venables *et al.* reported that the spatial resolution of this method is $\sim 19 \text{ nm}$ [22], and Kazemian *et al.* indicated that a resolution of $< 6 \text{ nm}$ can be expected for favorable specimens [23]. However, the magnification of these images was approximately 50,000X (the scanned field area is approximately $2.6 \times 2 \mu\text{m}^2$), since the SE contrast deteriorated rapidly with increasing magnification [6]. This is because the irradiation dose per unit area increases at high magnification, which leads to a significant irradiation effect. This magnification (the scanned field area is approximately $2.6 \times 2 \mu\text{m}^2$, 2 nm/1 pixel) is often sufficiently high for the compound semiconductor to be analyzed. However, higher magnification

observation is sometimes required in order to investigate the dopant distribution in the multi quantum well, etc., although the SE contrast deteriorates rapidly with increasing magnification [6]. As a result, the brightness of energy-filtered images is decreased and the image quality is degraded, because of the decrease in the signal to noise ratio, as can be seen in Fig.4-16.

Based on the understanding given above, the method used to obtain clear contrast with high magnification is investigated.

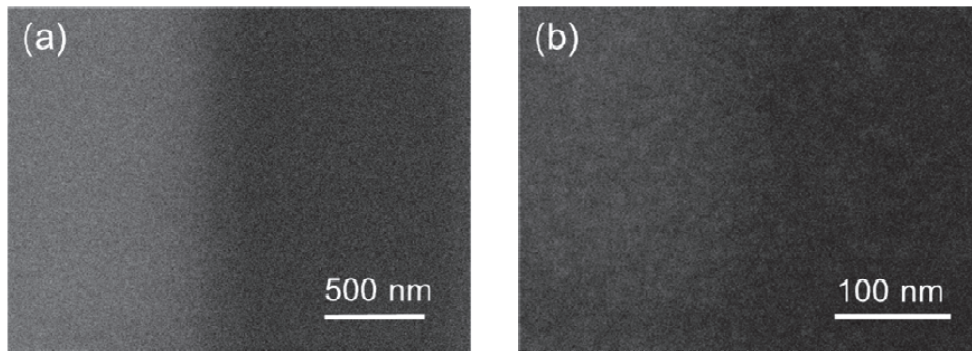


Fig. 4-16. Energy-filtered images of InP p-n junction at (a) 20,000X and (b) 250,000X magnification.

4.6.2 Image quality improvement method

In order to increase the signal to noise ratio of the SEM images, increasing the signal (dopant contrast) and/or decreasing the noise (irradiation influence) is required. Table 4-2 shows the methods that decrease the irradiation effect. Because dramatic effects could not be expected for these methods, apart from in the case of energy-filtering, the methods for increasing contrast shown in Table 4-2 were investigated.

Methods that involve changing the detector position [13] and applying a reverse-bias voltage [14] have also been reported. In this study, the reverse-bias voltage application approach was adopted because it has a more potent effect. Thus, a reverse-bias voltage (V_r) was applied across the

p-n junction of InP in situ during SEM observation, as shown schematically in Fig. 4-17.

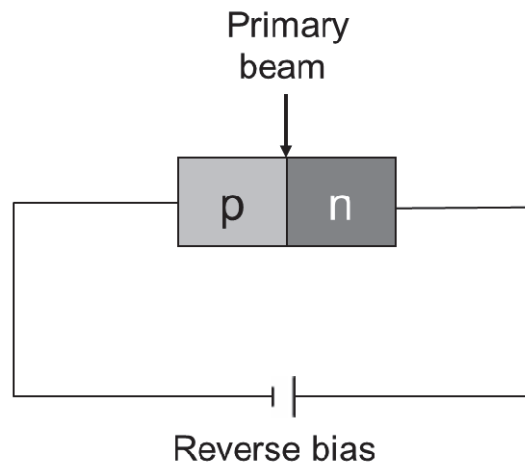


Fig. 4-17. Schematic diagram of reverse-bias voltage application.

In order to confirm the effect of V_r on the SEM contrast, the SE intensities from the p- and n-type regions were obtained using an unfiltered imaging method. The same contrast and brightness settings were used for all measurements. Figure 4-18 shows the SEM images and the SE intensities as a function of V_r . The contrast increased with increasing reverse biasing of the junction, because the reverse-bias voltage increases the potential barrier and leads to an increase in the contrast, as previously reported in ref. [14]. When the contrast is increased through application of a reverse-bias voltage, a relative decrease in the effect of the electron beam irradiation occurs. Therefore, this method was applied to the high-magnification SEM observation of a p-n junction.

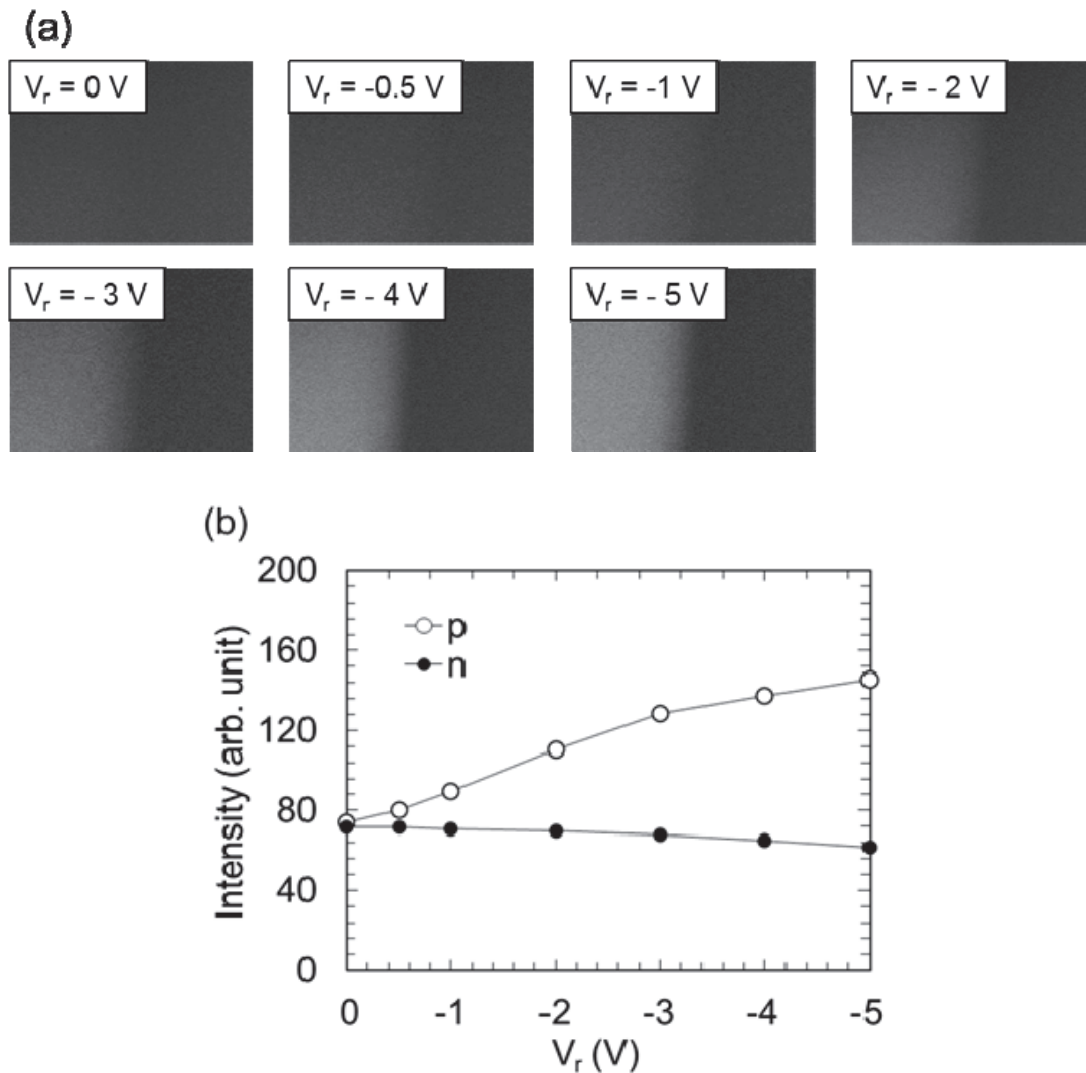


Fig. 4-18. (a) SE images and (b) intensities of both p- and n-type layers as a function of the reverse-bias voltage [3].

4.6.3 Reverse-bias voltage application results

SEM images of the p-n junction in InP, as shown in Fig. 4-19, were obtained at magnifications ranging from 10,000 to 250,000X, which was the highest possible magnification at an accelerating voltage of 1.0 kV using the Hitachi S-4800 FE-SEM, for detection modes (a) –(d). At 10,000X magnification, the contrast was clearly observed in all detection modes. In

order to investigate which detection mode was appropriate for practical high-magnification visual observation of the contrast, the intensities from the p-type and n-type layers in each detection mode were adjusted to approximately 150 and 100, respectively, at 10,000X magnification, by changing the contrast and brightness settings. The images for magnifications above 10,000X were acquired using the same settings in each detection mode. Thus, these experiments can indicate the appropriate detection mode in which SE intensities from p-type and n-type layers remain stable, even at a high magnification, for practical use.

The p-n junction contrast was clearly observed using detection mode (d), even at 250,000X magnification, while it was decreased with increasing magnification for detection modes (a)–(c) and no contrast was observed at 250,000X magnification.

Figure 4-20 shows the intensity profiles as a function of magnification. For detection mode (a), the intensities from the p- and n-type layers decreased rapidly with increasing magnification, falling to almost 0 at 100,000X magnification. The contrast was invisible at 50,000X magnification.

For detection mode (b), the intensity from the n-type layer fell slightly, from 95 at 10,000X magnification to 71 at 250,000X magnification. In contrast, the intensity from the p-type layer decreased from 155 at 10,000X magnification to 73 at 250,000X magnification, which was almost identical to the intensity from the n-type layer. The dopant contrast was invisible at 250,000X magnification, but visible at 50,000X magnification.

For detection mode (c), the intensity difference between the p- and n-type regions was retained even at high magnification. However, the intensities decreased with increasing magnification, falling to approximately 30 and 65 for the n-type and p-type layers, respectively, at 250,000X magnification, and little dopant contrast was observed. This indicates that high-energy SEs are also affected by electron beam irradiation during high-magnification observation.

	(a) $V_r = 0\text{ V}$ $V_c = 0\text{ V}$	(b) $V_r = -3\text{ V}$ $V_c = 0\text{ V}$	(c) $V_r = 0\text{ V}$ $V_c = 3\text{ V}$	(d) $V_r = -3\text{ V}$ $V_c = 6\text{ V}$
10,000X				
20,000X				
30,000X				
50,000X				
100,000X				
150,000X				
200,000X				
250,000X				

Fig. 4-19. SEM images obtained using various detection modes: (a) unfiltered without reverse-bias voltage, (b) unfiltered with reverse-bias voltage, (c) filtered without reverse-bias voltage, and (d) filtered with reverse-bias voltage [3].

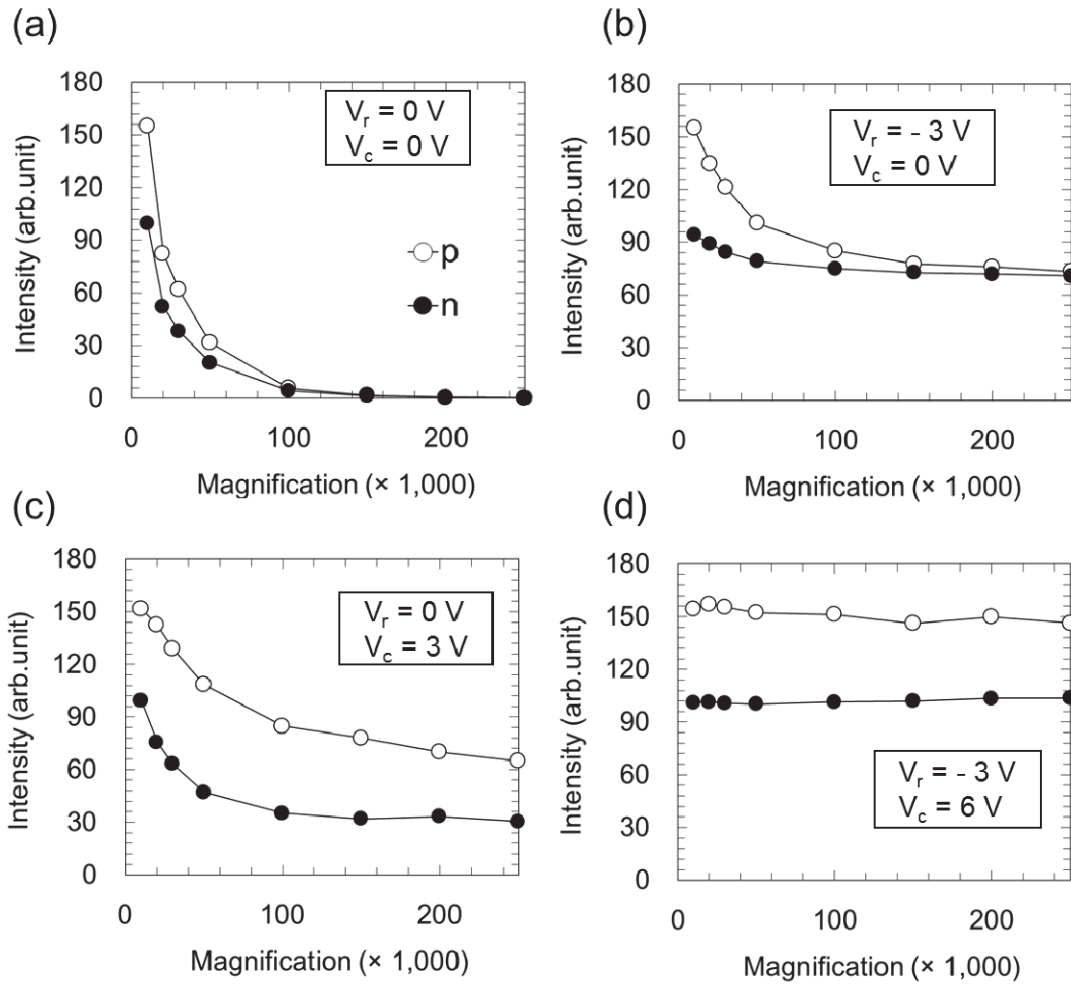


Fig. 4-20. Intensity profiles for each detection mode as a function of magnification (x-axis values are multiplied by 1,000) [3].

For detection mode (d), the intensities from both the p- and n-type layers remained constant at magnifications ranging from 10,000X to 250,000X, because of the effects of both the SE energy filtering and reverse-bias voltage. Therefore, the contrast could be clearly observed even in the image obtained at 250,000X magnification.

Thus, when both energy-filtering and reverse-bias voltage application are employed, the effect of the electron beam irradiation on the imaging can be reduced substantially and contrast can be observed at high magnification.

4.6.4 Discussion using SE energy distribution

observation

As discussed above, the imaging method using both energy-filtering and an applied bias voltage is effective for observing the contrast at high magnification. This is because both energy-filtered imaging and reverse-bias voltage work well in reducing the effect of the electron beam irradiation. Figure 4-21 shows the SE energy distributions of cleaved and irradiated surfaces under $V_r = -3$ V. The electron beam was intentionally irradiated on the cleaved p-n regions by taking a single slow-scan image at 80,000X magnification at a scan rate of 20 s per frame. The figure shows that low-energy SE emissions ($V_c \sim 6$ V), especially from the p-type layers, decreased dramatically once the electron beam was irradiated. Because high-pass energy-filtered imaging at $V_c = 6$ V does not detect low-energy SEs ($V_c < 6$ V), the imaging method can significantly reduce the effect of the irradiation. In addition, the reverse-bias voltage increases the contrast, and results in a relative decrease in the influence. As a result, the SE intensities remained stable, as shown in Fig. 4-19.

In Fig. 4-21, the SE counts were negative at $V_c = 1.5$ and 3 V. This phenomenon was reproducibly observed in every experiment with reverse-bias voltage application. In addition, the SE counts at $V_c = 1.5$ to 6 V became negative when $V_r = -6$ V. This indicates the phenomenon is caused by applied bias voltage. However, the mechanism is still not well understood although it has been examined. The influence of reverse-bias voltage on an energy-filtering detection system must be more fully explored through many additional experiments and analyses.

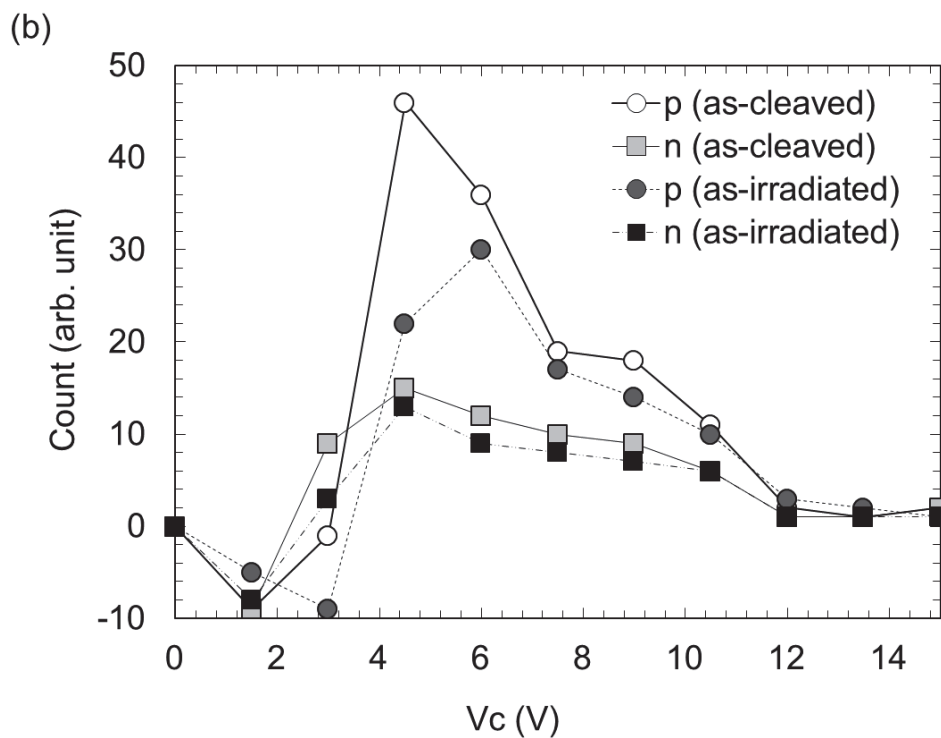
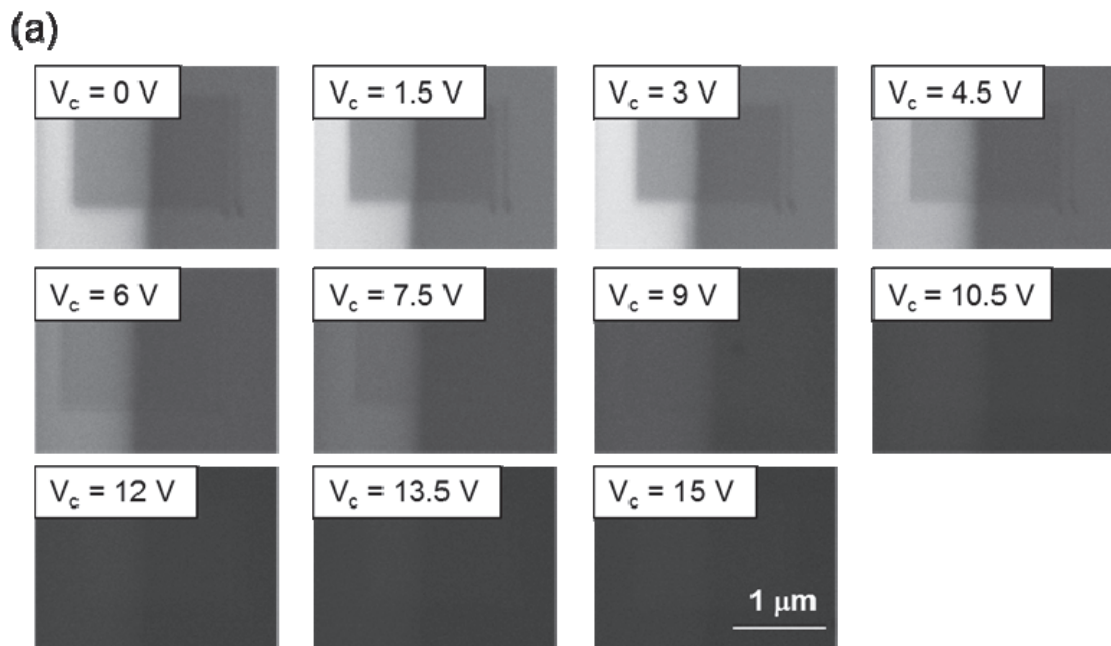


Fig. 4-21. (a) High-pass energy-filtered images of cleaved and irradiated surfaces under $V_r = -3 \text{ V}$ in the $0 \text{ V} \leq V_c \leq 15 \text{ V}$ range, and (b) the SE energy distribution obtained from these SE images [3].

Thus, the contrast of an InP semiconductor can be visually observed even at 250,000X magnification using both energy-filtering and an applied bias voltage. This is because energy-filtered imaging reduces the effect of the irradiation, even when reverse biasing is applied to increase the contrast and relatively decrease the sensitivity to the irradiation influence. This imaging method can be widely used for semiconductor devices and, therefore, provides a high magnification 2D dopant profiling method with a high data acquisition rate and rapid sample preparation for industrial use.

4.7 Discussion of dopant contrast mechanism

In this chapter, it was confirmed that the surface charging strongly affects dopant contrast, and the dominant factor of the contrast is sometimes the surface and/or the interface states. This indicates the surface and/or the interface model must be taken into account in the dopant contrast mechanism. In contrast, it is also confirmed that the contrast dramatically increases when the potential barrier of a p-n junction is increased through the application of a reverse-bias voltage. The results indicate that that built-in potential, which produces external and internal electric field of the sample, gives rise to dopant contrast as indicated in the discussion in Section 3.6. Thus, both surface charging and the built-in potential should be considered when investigating the dopant contrast.

4.8 Conclusions

This work highlights the problem of decreased dopant contrast due to the electron beam irradiation used in SEM observation, which was one of the problems preventing the practical use of SEM dopant profiling.

Although reproducibility is an important factor for analysis techniques, SEM dopant profiling encounters a contrast reduction problem due to the electron beam irradiation, which occurs in every case and is,

therefore, a major issue that must be overcome. Thus, the purpose of this part of the study was to reduce the influence of the irradiation on the contrast and increase reproducibility. In order to increase the reproducibility SE energy-filtering and the application of a reverse-bias voltage were attempted in this study.

First, the effect of the irradiation on the sample was investigated. The SE energy distribution indicates that the irradiation causes a decrease in the low-energy SE emissions, and reduces dopant contrast in unfiltered SE images. The mechanism through which the irradiation causes this decrease in low-energy SE emissions was discussed, and a surface charging model was suggested based on experimental results.

Then, the efficacy of SE energy-filtering was investigated. The unfavorable effects of electron beam irradiation can be reduced substantially through high-pass energy-filtered imaging, and highly reproducible dopant profiling can be achieved during continuous SEM observation. It was demonstrated that the energy-filtered imaging method can be widely used for various samples. As an example, an application to the gold surfaces was examined.

Furthermore, the effect of a reverse-bias voltage application was investigated. Even under high-magnification conditions, where the effect of the irradiation is typically increased, it was shown that the contrast was clearly observed by simultaneously applying both SE energy filtering and a reverse-bias voltage.

This imaging method can be widely employed for compound semiconductor devices in order to provide reproducible 2D dopant profiling with a high data acquisition rate and rapid sample preparation, and is therefore expected to make a significant contribution to the compound semiconductor manufacturing industry.

Finally, the dopant contrast mechanism was discussed. It was indicated that both the surface charging and built-in potential should be considered in order to discuss the dopant contrast.

4.9 References

- [1] D. Tsurumi, K. Hamada, and Y. Kawasaki, “Energy-filtered imaging in a scanning electron microscope for dopant contrast in InP.,” *J. Electron Microsc. (Tokyo)*, vol. 59 Suppl 1, pp. S183–S187, 2010.
- [2] D. Tsurumi, K. Hamada, and Y. Kawasaki, “Highly Reproducible Secondary Electron Imaging under Electron Irradiation Using High-Pass Energy Filtering in Low-Voltage Scanning Electron Microscopy,” *Microsc. Microanal.*, vol. 18, no. 02, pp. 385–389, 2012.
- [3] D. Tsurumi, K. Hamada, and Y. Kawasaki, “Energy-Filtered Secondary-Electron Imaging for Nanoscale Dopant Mapping by Applying a Reverse Bias Voltage,” *Jpn. J. Appl. Phys.*, vol. 51, no. 10R, 106503, 2012.
- [4] R. Turan and D. D. Perovic, “Mapping electrically active dopant profiles by field-emission scanning electron microscopy,” *Appl. Phys. Lett.*, vol. 69, no. 11, pp. 1593–1595, 1996.
- [5] M. R. Castell, D. a Muller, and P. M. Voyles, “Dopant mapping for the nanotechnology age.,” *Nat. Mater.*, vol. 2, no. 3, pp. 129–131, 2003.
- [6] P. Kazemian, C. Rodenburg, and C. J. Humphreys, “Effect of experimental parameters on doping contrast of Si p-n junctions in a FEG-SEM,” *Microelectron. Eng.*, vol. 73–74, pp. 948–953, 2004.
- [7] C. Rodenburg, M. A. E. Jepson, B. J. Inkson, E. Bosch, A. K. W. Chee, and C. J. Humphreys, “Energy filtered scanning electron microscopy: Applications to dopant contrast,” *J. Phys. Conf. Ser.*, vol. 209, 012053, 2010.
- [8] C. G. H. Walker, F. Zaggout, and M. M. El-Gomati, “The role of oxygen in secondary electron contrast in doped semiconductors using low voltage scanning electron microscopy,” *J. Appl. Phys.*, vol. 104, no. 12, 123713, 2008.

- [9] L. Reimer, *Image Formation in Low-voltage Scanning Electron Microscopy*. Bellingham, Washington: SPIE Press, 1993.
- [10] A. Ono, "Influence of incident electron energy on specimen contamination in SEM mode," in *Proc. XIth Int. Congr. Electr. Micr.*, pp. 417–418, 1986.
- [11] A. D. Garetto, D. D. Griffis, P. E. Russell, J. Fowlkes, and P. D. Rack, "Growth Mechanisms of Electron Beam Induced Carbon Deposition Using Hydrocarbon Contamination," *Microsc. Microanal.*, vol. 11, no. S02, pp. 850–851, 2005.
- [12] T. Isabell, P. Fischione, C. O'Keefe, M. Guruz, and V. Dravid, "Plasma Cleaning and Its Applications for Electron Microscopy.," *Microsc. Microanal.*, vol. 5, no. 2, pp. 126–135, 1999.
- [13] C. Schönjahn, R. F. Broom, C. J. Humphreys, A. Howie, and S. A. M. Mentink, "Optimizing and quantifying dopant mapping using a scanning electron microscope with a through-the-lens detector," *Appl. Phys. Lett.*, vol. 83, no. 2, pp. 293–295, 2003.
- [14] S. L. Elliott, R. F. Broom, and C. J. Humphreys, "Dopant profiling with the scanning electron microscope—A study of Si," *J. Appl. Phys.*, vol. 91, no. 11, pp. 9116–9122, 2002.
- [15] M. M. El-Gomati and T. C. R. Wells, "Very-low-energy electron microscopy of doped semiconductors," *Appl. Phys. Lett.*, vol. 79, no. 18, pp. 2931–2933, 2001.
- [16] M. El-Gomati, F. Zaggout, H. Jayacody, S. Tear, and K. Wilson, "Why is it possible to detect doped regions of semiconductors in low voltage SEM: a review and update," *Surf. Interface Anal.*, vol. 37, no. 11, pp. 901–911, 2005.
- [17] G. H. Jayakody, T. R. C. Wells, and M. M. El-Gomati, "Imaging of doped Si in low and very low voltage SEM: the contrast interpretation," *J. Electron Spectros. Relat. Phenomena*, vol. 143, no. 2–3, pp. 233–239, 2005.

- [18] S. M. Sze, *Physics of Semiconductor Devices*, 2nd ed. New York: J. Wiley & Sons, 1981.
- [19] R. K. W. A. C. Beer, *Physics of III-V Compounds, Volume 2*. New York: Academic Press, 1966.
- [20] A. Yamaguchi, "Material Characterization of Semiconductor Devices," *SEI Tech. Rev.*, vol. 70, pp. 17–27, 2010.
- [21] H. C. Card and E. H. Rhoderick, "Studies of tunnel MOS diodes I. Interface effects in silicon Schottky diodes," *J. Phys. D. Appl. Phys.*, vol. 4, no. 10, pp. 1589-1601, 1971.
- [22] D. Venables, H. Jain, and D. C. Collins, "Secondary electron imaging as a two-dimensional dopant profiling technique: Review and update," *J. Vac. Sci. Technol. B*, vol. 16, pp. 362–366, 1998.
- [23] P. Kazemian, S. a. M. Mentink, C. Rodenburg, and C. J. Humphreys, "High resolution quantitative two-dimensional dopant mapping using energy-filtered secondary electron imaging," *J. Appl. Phys.*, vol. 100, no. 5, 054901, 2006.

Chapter 5

Establishment of Contrast Interpretation Method at Heterojunction Interfaces

This chapter presents the establishment of an effective interpretation method that can be applied to the obtained SEM images [1]. This was the third problem impeding the practical use of SEM dopant profiling, as shown in Table 5-1.

5.1 Introduction

As described in Chapter 1, evaluation of the dopant distribution is essential, since this distribution plays an important role in semiconductor devices. However, the interpretation of SEM contrast in compound semiconductor devices is more complicated than for silicon devices, because of the presence of heterostructures, which are features of compound semiconductors. For example, photodiodes (PD) consist of a p-InP layer and

an i-InGaAs layer on an n-InP layer, as shown in Fig. 5-1. The dopant diffusion length from the p-InP to the i-InGaAs determines important device properties, such as detection sensitivity, response speed, etc. Thus, the device properties are strongly dependent on the diffusion length at the heterojunction and, therefore, an accurate 2D dopant profiling is required.

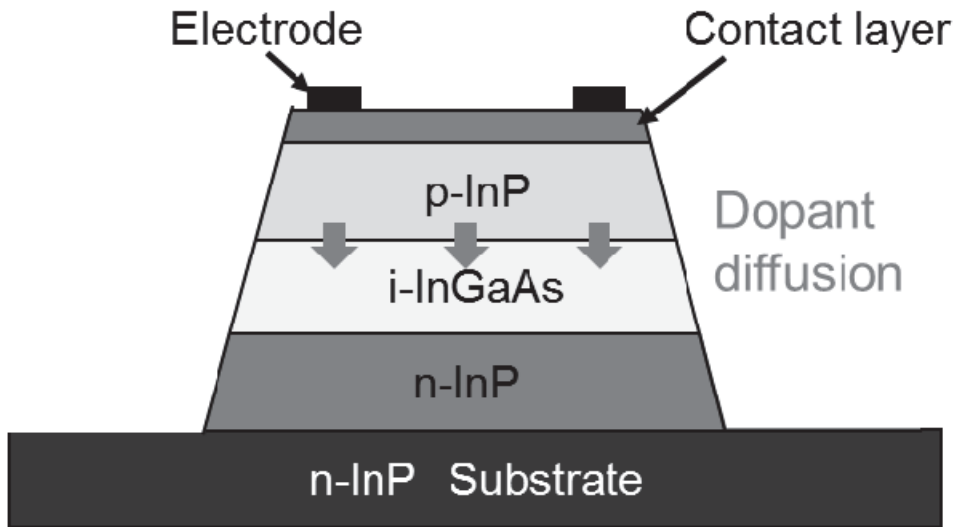


Fig. 5-1. PD structure for optical communication systems.

However, SEM contrast arises not only from the dopant concentration but also from the potential change at the heterojunctions [2]. Thus, the 2D dopant profiling of a compound semiconductor with heterojunctions is more difficult than that of a homostructure. This profiling has rarely been reported, although a large number of reports on the 2D dopant profiling of homostructures exist [3]–[9]. For accurate 2D dopant profiling of compound semiconductor devices, the establishment of a contrast interpretation method at heterojunction interfaces is required. Thus, it is essential to take the influence of the heterojunction on the SEM contrast into account, and to clearly determine the dependence of the SEM contrast on the dopant concentration at the interface.

5.2 Purpose

Motivated by the information given above, the purpose of this part of the study is to determine the SEM contrast dependence on the dopant concentration at the interface, to achieve accurate 2D dopant profiling of compound semiconductors.

5.3 Experimental method

This section describes the experimental details used in this part of the study, including the sample structure, the SEM observation method, and secondary ion mass spectrometry (SIMS) methods.

5.3.1 Sample structure and SEM observation conditions

Heterostructures composed of a p⁺-type InP layer (*ca.* 1×10^{19} Zn atoms/cm³) and an undoped InGaAs layer (n-type, 1×10^{16} atoms/cm³) on an n⁺-type InP substrate (1×10^{18} Sn atoms/cm³), as shown in Fig. 2-1 (c), were used as test specimens.

The heterostructures were grown using metal-organic vapor phase epitaxy and Zn atoms were diffused from the surface to the p⁺-InP and n⁻-InGaAs layers. Two specimens (labeled A and B) with different Zn diffusion lengths were prepared by varying the diffusion conditions. The samples were freshly cleaved in air immediately prior to loading in the SEM chamber.

SEM images were collected using a Hitachi S-4800 FE-SEM, as shown in Fig. 2.4.3. The primary electron beam energy used was 1 kV, which was chosen to increase the dopant contrast level [10]. The working distance was 2 mm. In the experiments, images with a negative control

electrode voltage, $V_c = 3$ V, were used to reduce the influence of contaminants, as discussed in Chapter 4 [11,12].

5.3.2 SIMS measurement method

Zn concentration profiles were obtained using SIMS. SIMS is measured by Evans Analytical Group (EAG) [13] through Nano Science Corporation which is its Japanese agent.

The analysis was conducted using a Cameca 4f. The Zn ion intensity was obtained using a 3.5 keV Cs⁺ beam. The data collected were positive secondary ions: $^{64}\text{Zn} + ^{133}\text{Cs}$ and $^{75}\text{As} + ^{133}\text{Cs}$. Conversion of the measured secondary ion counts for Zn to concentration was accomplished separately for InP and InGaAs, respectively, using both relative sensitive factors (RSFs) based on an EAG implant standard of ^{64}Zn in InP, and the matrix ion was $^{31}\text{P} + ^{133}\text{Cs}$.

5.3.3 Potential calculation method

Electrostatic potential profiles were calculated from Zn concentration profiles obtained by SIMS using the device simulation program LASTIP (LASer Technology Integrated Program), designed by Crosslight Software Inc [14].

5.4 Results and discussion

This section presents a comparison of SEM images and SIMS measurement results in order to confirm accurate 2D dopant profiling across the heterojunction. The sensitivity of SEM to the potential is derived from the SEM observations and from potential calculations based on the SIMS measurement results. The results are then used to investigate the

dependence of the SEM contrast on the Zn diffusion length across the p⁺-InP/undoped n⁻-InGaAs interface.

5.4.1 SEM observation and SIMS measurement

Figures 5-2 (a) and (d) show back-scattered electron (BSE) images and Figs. 5-2 (b), (c), (e) and (f) show SE images for samples A and B. The scanning direction of the electron beam is vertical in the images.

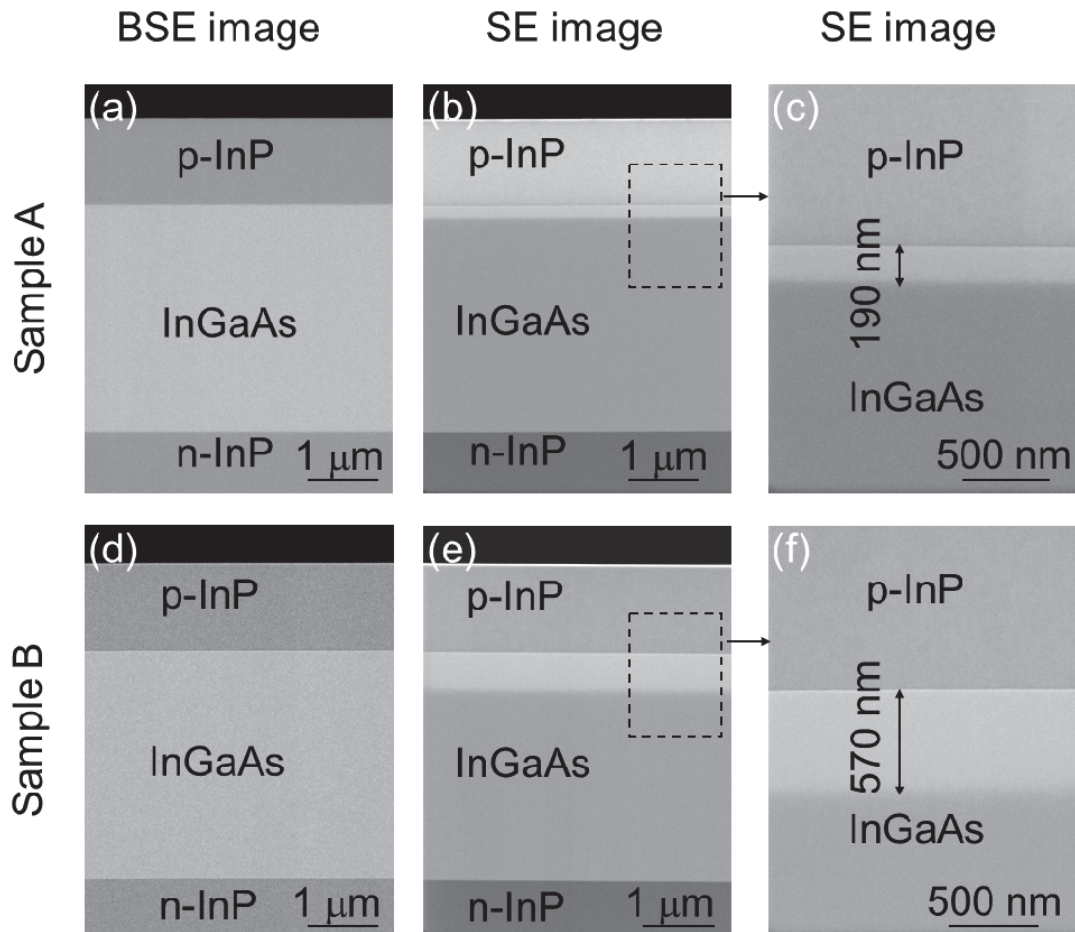


Fig. 5-2. (a,d) BSE and (b,c,e,f) SE images of p⁺-InP/n⁻-InGaAs/n⁺-InP heterostructures [1].

In the SE images of both samples, the p-InP layer is brighter than the n-InP layer, because of the dopant contrast. The p-InP layer contrast in samples A and B appear different, and this may indicate that some of the Zn atoms in sample B are electrically inactive. The contrast in the SE images for InGaAs near the interface with p-InP is brighter than that with n-InP. The widths of the brighter regions are approximately 190 and 570 nm for samples A and B, respectively.

Figure 5-3 shows SEM image intensity profiles and SIMS profiles of the Zn concentration and arsenic (As) secondary ion intensity for samples A and B. The thicknesses of the InP and InGaAs layers in the SIMS results were corrected using the layer thicknesses measured from the SEM images, because the SIMS depth scale is not accurate for multilayer samples

The SIMS depth profile is typically calibrated by measuring the crater depth with a stylus profilometer after sputtering, and a single average sputter rate is usually used for the depth scale, even though the sample is multilayered and each layer has a different sputter rate. As a result, the relative thickness of the layers in the SIMS profile is different to that of the actual structures. Therefore, to achieve an accurate depth scale, correct sputter rates for the InP and InGaAs layers are required. Here, the sputter rates were experimentally determined using a raw As secondary ion intensity profile, which functions as a layer marker for SIMS measurements, and the layer thicknesses were measured from the SEM images. The layer thicknesses from the SIMS measurements were well corrected, as shown by the As ion intensity profiles and SEM images in Fig. 5-3.

The SEM image intensity profiles shown in Fig. 5-3 correspond well with the Zn SIMS profiles of both samples. The Zn profiles suddenly decreased at 1.5 and 1.9 μm from the surface (190 and 570 nm from the interface) in samples A and B, respectively.

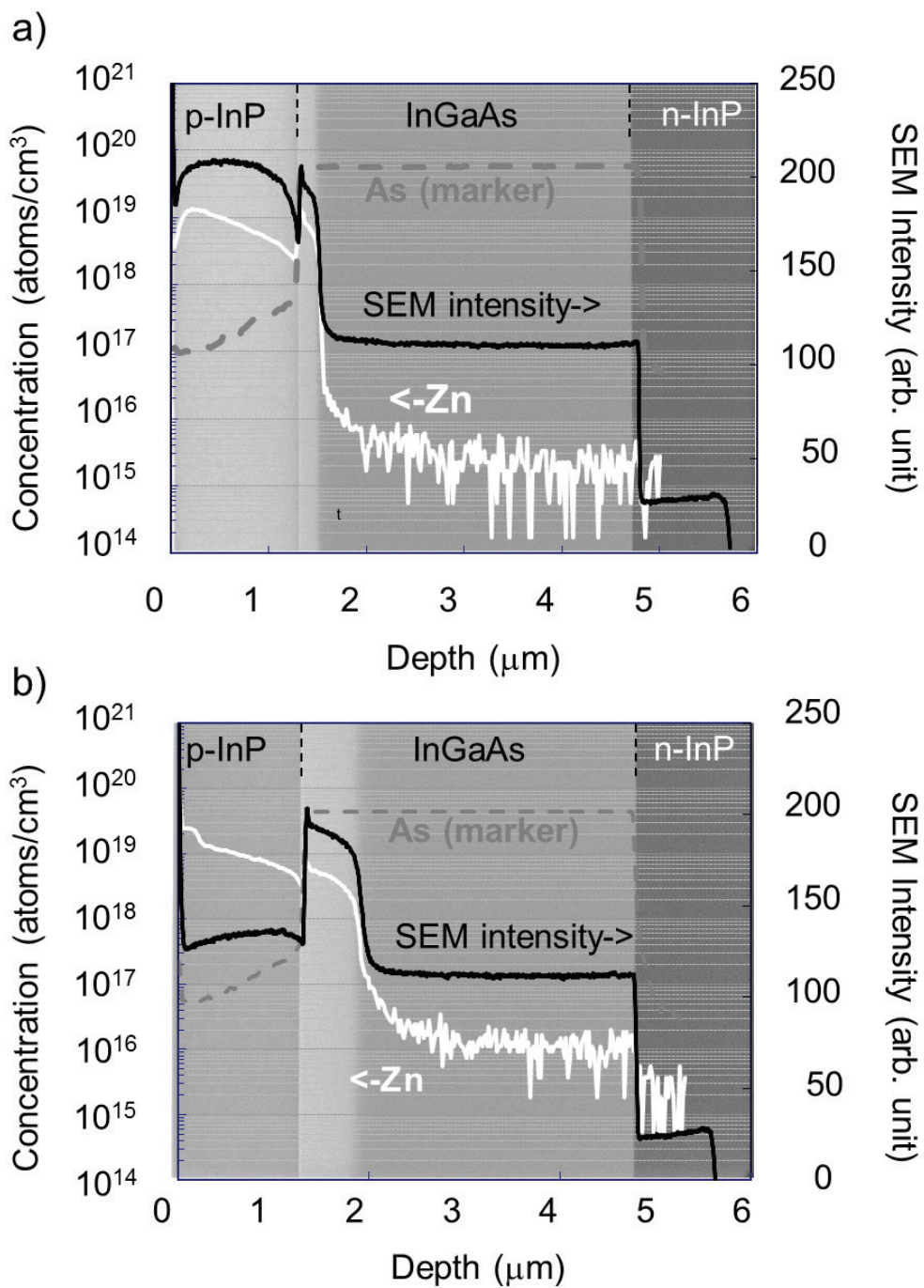


Fig. 5-3. SE images with SE intensity profiles and Zn concentration depth profiles (SIMS) for samples (a) A and (b) B. As marker profiles are shown with raw ion intensities as a layer marker [1].

5.4.2 SEM electrostatic potential sensitivity

Although these results imply that SEM can be effectively used to detect Zn diffusion, SEM contrast arises not only from Zn diffusion, but also from the heterojunction [2,9]. Therefore, accurate 2D dopant profiling requires that the dependence of the SEM contrast on the Zn diffusion length across the interface be fully determined. The SEM sensitivity for the electrostatic potential was derived using the SEM intensity profiles and electrostatic potential calculation results. The dependence of the SEM contrast on the Zn diffusion length across the interface was then investigated with respect to the derived SEM sensitivity. Here, it was confirmed that the Zn inactivation in the p-InP layer of sample B did not affect the potential calculation results of the p-n junction (1.9–2.3 μm) as shown in Fig. 5-4.

The calculated potential is compared with the SEM image intensity for both samples in Fig. 5-5. It can be seen that the potential remained stable in the high SE intensity region of the InGaAs layer (depths of 1.3–1.5 μm and 1.3–1.9 μm in samples A and B, respectively). The SE intensity decreased in the InGaAs layer at approximately 1.5 and 1.9 μm from the surface in samples A and B, respectively, while the potential increased. The SEM contrast simultaneously fell to a low level of approximately 1.7 and 2.1 μm from the surface in samples A and B, respectively; however, the potential continued to increase and plateaued at approximately 2.0 and 2.4 μm from the surface in samples A and B, respectively. These positions were approximately 0.3 μm away from the depth where the SEM contrast became constant, which indicated that SEM is not perfectly sensitive to the electrostatic potential.

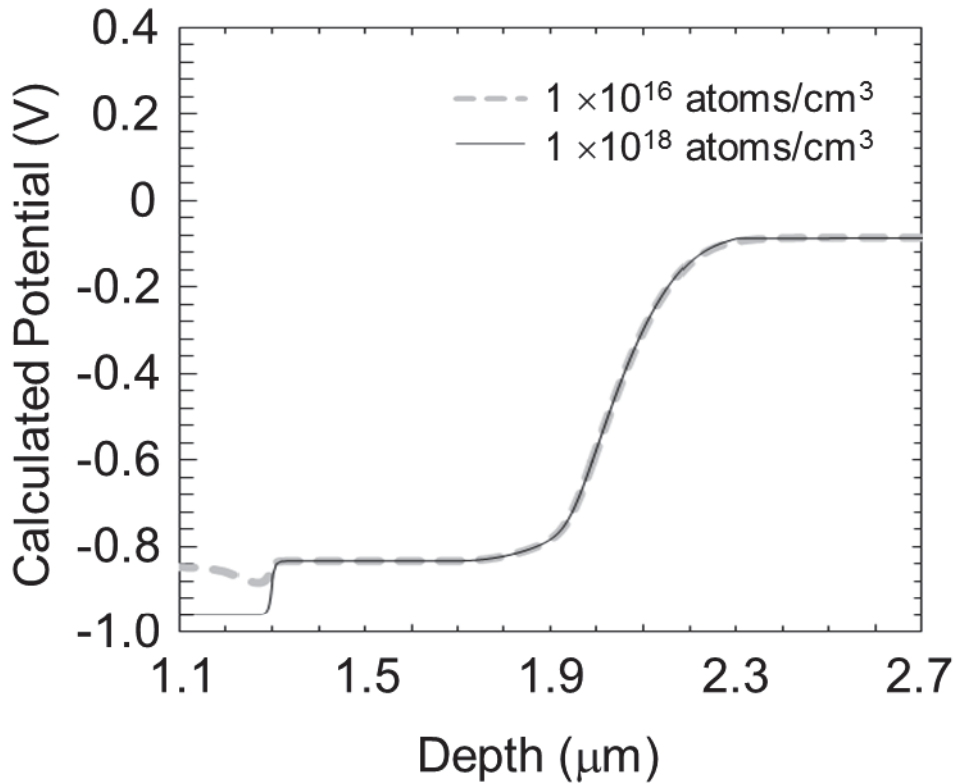


Fig. 5-4. Potential calculation results of sample B at different Zn concentrations in p-InP: 1×10^{16} atoms/cm³ (gray broken line), 1×10^{18} atoms/cm³ (black line).

Figure 5-6 shows the SEM sensitivity to the electrostatic potential obtained through comparison of the SE intensity profiles and electrostatic potentials. It was found that the SEM was sensitive to the potential from -0.9 to -0.75 V, but did not exhibit sensitivity at over -0.75 V. In these samples, the position where the potential value is -0.75 V is in the region of the p-n junction in the InGaAs layer; therefore, SEM is sensitive to the potential variation in the p-type region, but not to that in the n-type region. Thus, p-type potential profiling is available using SEM. This feature was also observed in Ref. [4,10], where SEM was also found to be suitable for the observation of p-type dopant distribution.

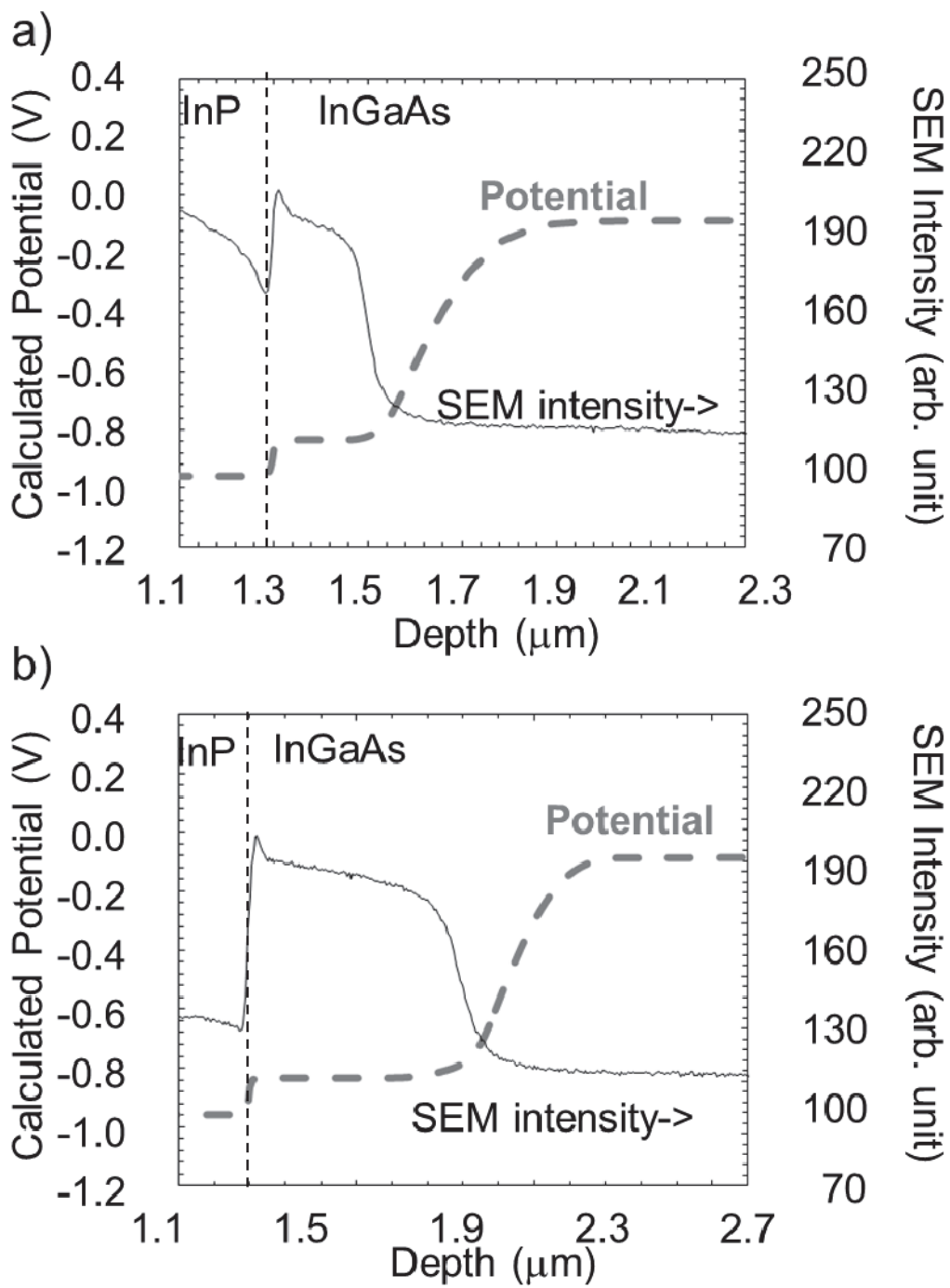


Fig. 5-5. Calculated electrostatic potentials and SE intensity profiles for samples (a) A and (b) B [1].

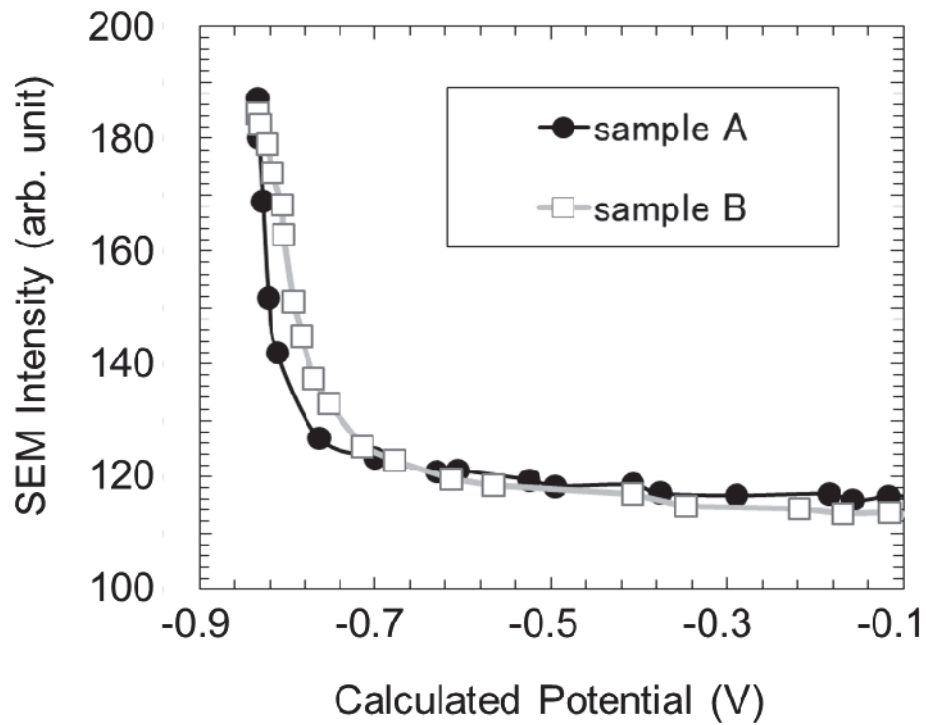


Fig. 5-6. SE intensities for samples A (circles) and B (squares) as a function of calculated electrostatic potential, which indicates the SEM sensitivity to the potential [1].

5.4.3 SEM contrast dependence on Zn diffusion length across the interface

Based on the derived SEM sensitivity and the electrostatic potential calculations, the dependence of the SEM contrast on the Zn diffusion length across the interface was estimated.

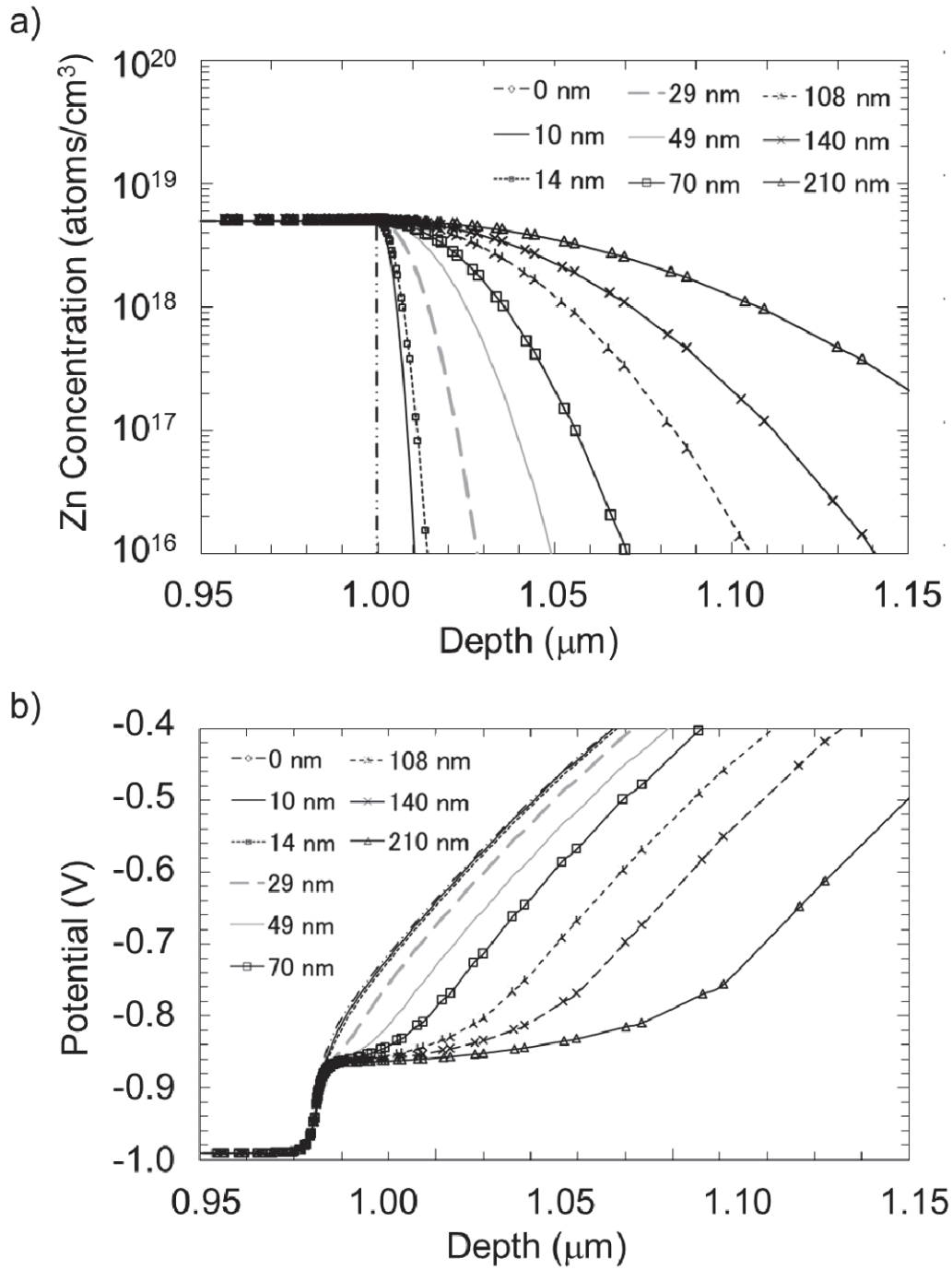


Figure 5-7. (a) Zn concentration profiles for potential calculation and (b) calculated potential. The Zn diffusion lengths were in the range of 0 (no diffusion) to 210 nm [1].

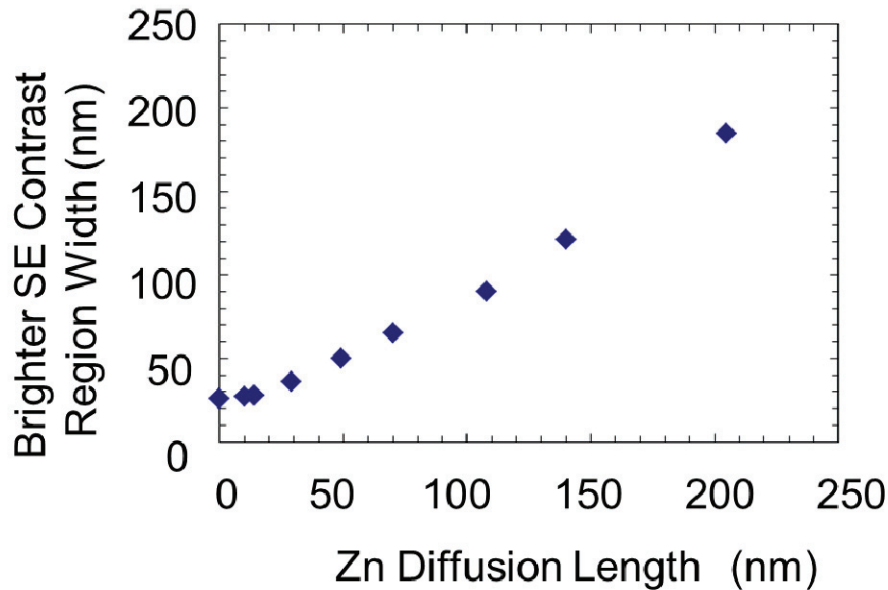


Fig. 5-8. Calculated widths of the brighter SE contrast region in the n -InGaAs layer as a function of the Zn diffusion length [1].

Figure 5-7 (a) shows the Zn concentration profiles for the potential calculation. The Zn diffusion lengths were in the range of 0 (no diffusion) to 210 nm. Here, the p^+ -InP/undoped n -InGaAs interface is 1.0 μm . The Zn distributions were assumed to be Gaussian. Figure 5-7 (b) shows the calculated potential of each case. From Fig. 5-7 (b) and the SEM sensitivity range revealed in section 5.4.2, the SEM contrast can be calculated. Thus, the SEM contrast dependence on the Zn diffusion length was estimated.

Figure 5-8 shows the width of the brighter SEM contrast region as a function of the Zn diffusion length. When the diffusion length is 0 nm, the width of the brighter SEM contrast region in the n -InGaAs layer is estimated to be 30 nm from the interface. This is caused by the potential variation due to the heterojunction. Therefore, it is difficult to profile accurate dopant distributions when the Zn diffusion length is shorter than 30 nm. In contrast, when the Zn diffusion length is longer than 30 nm, the width of the brighter SE contrast region tends to correspond to the Zn diffusion length. This is because the factor dominating the electrostatic potential variation is not the heterojunction, but rather the Zn diffusion 30

nm from the interface. This explains the surprisingly good agreement of the SEM intensity profiles with the Zn concentration profiles. Hence, Zn diffusion at a distance farther than 30 nm from the Zn-doped p⁺-InP/undoped n⁻InGaAs interface can be effectively detected by SE imaging. This confirms that SE imaging with electrostatic potential calculations can be widely used to obtain accurate dopant profiling, even at heterojunctions.

5.5 Discussion of dopant contrast mechanism

As discussed in Section 3.6 and 4.7, experimental results indicate that the built-in potential gives rise to the dopant contrast, and the surface charging strongly affects the contrast. However, the insensitivity to the n-type regions (as shown in Fig. 5-6) is not completely understood, although extensive discussions on this topic have been published [4,10]. One of the possible interpretive models is that the contrast depends on not only the potential but also the carrier concentration. When the carrier concentration increases, it is expected that the free electrons which contribute to elastic scattering of electrons increase. This results in an increase in SE generation and emission. In this case, the potential decreases when the carrier concentration increases in the p-type regions and, therefore, both potential and carrier concentration act to increase the SE emission. Then, a brighter contrast is observed. In contrast, in n-type regions, the potential also increases with increasing carrier concentration. Then, although the potential works to decrease the SE emission, it is compensated for by the carrier concentration, which acts to increase the SE generation and emission. Then, the contrast is insensitive to the dopant concentration in the n-type regions. This suggested carrier concentration model should be examined further and the n-type insensitivity mechanism must be more fully explored. Complete potential profiling using SEM should also be discussed further.

5.6 Conclusions

This work highlights the application of SEM to Zn diffusion detection across a p^+ -InP/ n^- -InGaAs interface. The SEM contrast arises not only from the dopant concentration, but also from the potential change at the heterojunctions. Therefore, the interpretation of SEM contrast in compound semiconductor devices is more complicated than for silicon devices because of the heterojunctions, which are features of compound semiconductors. To develop an accurate 2D dopant profiling approach, it was therefore essential to clearly determine the SEM contrast dependence on the dopant concentration at the interface in this study.

In order to investigate the ability of SEM to detect dopant profiles at an interface, a p^+ -InP/ n^- -InGaAs interface was used as an example in this chapter. SEM imaging revealed that the InGaAs contrast near the interface with p^+ -InP was brighter than that near the interface with n^+ -InP. The Zn concentration profiles obtained using SIMS corresponded well with the SEM intensity profiles in the InGaAs layer. Considering both the SEM observations and potential calculation results, the dependence of the SEM contrast on the Zn diffusion length across the p^+ -InP/undoped n^- -InGaAs interface was investigated. Accurate dopant profiling was difficult when the Zn diffusion length was shorter than 30 nm, because of the influence of the heterojunction. In contrast, accurate dopant profiling was possible when the Zn diffusion length was longer than 30 nm, because the dominant factor of the variation in the electrostatic potential was not the heterojunction, but rather the Zn diffusion 30 nm from the interface. Consequently, Zn diffusion at over 30 nm from the surface of a Zn-doped p^+ -InP/undoped n^- -InGaAs interface can be effectively detected by SE imaging. Thus, SE imaging with potential calculations can be widely used for accurate dopant profiling, even at heterojunctions, and is therefore expected to make a significant contribution to the compound semiconductor industry.

Finally, the insensitivity of SEM to n -type regions was discussed. In order to explain these experimental results, a new model was proposed in which the contrast depends on not only the potential, but also the carrier concentration.

5.7 References

- [1] D. Tsurumi, K. Hamada, and Y. Kawasaki, “Observation of two-dimensional p-type dopant diffusion across a p⁺-InP/n⁻-InGaAs interface using scanning electron microscopy,” *J. Appl. Phys.*, vol. 113, no. 14, 144901, 2013.
- [2] B. Kaestner, C. Schönjahn, and C. J. Humphreys, “Mapping the potential within a nanoscale undoped GaAs region using a scanning electron microscope,” *Appl. Phys. Lett.*, vol. 84, no. 12, pp. 2109–2111, 2004.
- [3] R. Turan and D. D. Perovic, “Mapping electrically active dopant profiles by field-emission scanning electron microscopy,” *Appl. Phys. Lett.*, vol. 69, no. 11, pp. 1593–1595, 1996.
- [4] S. L. Elliott, R. F. Broom, and C. J. Humphreys, “Dopant profiling with the scanning electron microscope—A study of Si,” *J. Appl. Phys.*, vol. 91, no. 11, pp. 9116–9122, 2002.
- [5] S. Mil’shtein, “Semiconductor Devices ‘from Inside,’” *Scanning*, vol. 22, pp. 227–233, 2000.
- [6] M. R. Castell, D. a Muller, and P. M. Voyles, “Dopant mapping for the nanotechnology age.,” *Nat. Mater.*, vol. 2, no. 3, pp. 129–131, 2003.
- [7] W.-C. Hsiao, C.-P. Liu, and Y.-L. Wang, “Secondary emission of strain-induced dopant contrast in the source/drain regions of metal-oxide-semiconductor devices,” *Appl. Phys. Lett.*, vol. 88, no. 21, 212104, 2006.
- [8] P. Kazemian, S. a. M. Mentink, C. Rodenburg, and C. J. Humphreys, “High resolution quantitative two-dimensional dopant mapping using energy-filtered secondary electron imaging,” *J. Appl. Phys.*, vol. 100, no. 5, 054901, 2006.

- [9] A. A. Suvorova and S. Samarin, "Secondary electron imaging of SiC-based structures in secondary electron microscope," *Surf. Sci.*, vol. 601, no. 18, pp. 4428–4432, 2007.
- [10] C. Sealy, M. Castell, and P. Wilshaw, "Mechanism for secondary electron dopant contrast in the SEM," *J. Electron Microsc. (Tokyo)*, vol. 49, no. 2, pp. 311–321, 2000.
- [11] D. Tsurumi, K. Hamada, and Y. Kawasaki, "Energy-filtered imaging in a scanning electron microscope for dopant contrast in InP.," *J. Electron Microsc. (Tokyo)*, vol. 59 Suppl 1, pp. S183–S187, 2010.
- [12] D. Tsurumi, K. Hamada, and Y. Kawasaki, "Highly Reproducible Secondary Electron Imaging under Electron Irradiation Using High-Pass Energy Filtering in Low-Voltage Scanning Electron Microscopy," *Microsc. Microanal.*, vol. 18, no. 02, pp. 385–389, 2012.
- [13] "EAG | Evans Analytical Group, Analytical Testing Expertise | Laboratory Network." [Online]. Available: <http://www.eag.com/>. [Accessed: 20-Apr-2014].
- [14] "Crosslight Software | LASTIP." [Online]. Available: <http://crosslight.com/products/lastip/>. [Accessed: 20-Apr-2014].
- [15] J. T. Heath, C.-S. Jiang, and M. M. Al-Jassim, "Measurement of semiconductor surface potential using the scanning electron microscope," *J. Appl. Phys.*, vol. 111, no. 4, 046103, 2012.

Chapter 6

Conclusions

This thesis argues that a SEM-based 2D dopant profiling technique that meets the requirements of the compound semiconductor industry has been established. This has been achieved by overcoming the three major problems with sensitivity, reproducibility, and image interpretation impeding this technique using InP. This chapter summarizes the research results and describes the remaining issues.

6.1 Conclusions

In the last half-century, improvements in semiconductor device technology have made a significant contribution to the development of modern society. In particular, because compound semiconductor devices have higher speed, power, and luminance efficiency than silicon-based devices, these devices meet the demands of information and communication technology, energy-saving technology, etc. Thus, compound semiconductor devices with higher performance and lower cost are strongly required. For further development of these devices, progress in many areas of technology is essential, including analysis technology. One of the most important techniques in this field is 2D dopant profiling, because dopant distribution

in devices strongly affects their performance and reliability. Thus, a large number of dopant profiling techniques have been developed. Among these methods, SEM is the most attractive technique in terms of industrial use because of its rapid data measurement capability, high spatial resolution, and high sensitivity. However, if the history of 2D dopant profiling using SEM is reviewed, it becomes apparent that this method has encountered three major problems: an ineffective sample preparation technique for practical use and high-sensitivity measurements, the lack of a highly reproducible observation technique, and the lack of an interpretation technique for the heterojunction interfaces. Thus, the purpose of this study was to address these three major issues and establish a 2D dopant profiling technique that achieves the performance level required for compound semiconductor R&D and production. In addition, the dopant contrast mechanism, which is still unclear, was discussed using the data obtained through these experiments.

In this research, InP-based materials were used. This was because InP-based materials are some of the most difficult compound semiconductor materials to observe, and this technique's ability to overcome major issues using InP-based materials indicated that it can be widely applied to other compound semiconductor materials (GaAs, GaN, SiC, etc.).

The first problem was a decrease in dopant contrast due to sample preparation using ion milling. The mechanism causing the contrast reduction was identified and an ion-milling method was developed that yielded sensitivity on the same level as that of a cleaved surface. We focused on the thickness of the amorphous layer generated by the ion milling process, and the influence of this layer on dopant contrast was investigated. It was determined that, as the thickness of the amorphous layer increased, the dopant contrast decreased. An observation of dopant contrast equal to that of a cleaved surface from a surface prepared using 1.5-keV milling was demonstrated. These results indicate that such a thin amorphous layer leads to a sufficiently high dopant contrast for measurement, despite the fact that the surface is prepared using ion milling. Because this contrast was clearly observed in an InP sample, which is the most liable compound semiconductor material to be damaged, it is expected that this technique can be widely applied to the other compound semiconductors (GaAs, GaN, SiC, etc).

The second problem was reproducibility of the contrast. Dopant contrast decreases as a result of electron beam irradiation during SEM observation. In order to increase the reproducibility, the contrast reduction mechanism was identified and an observation technique was developed. In this study, we investigated the effect of SE energy selection using energy-filtered imaging. First, the SE energy distribution was observed in order to analyze the mechanism. The obtained distributions indicated that the dopant contrast was obtained in the SE energy range of 2–7 eV in particular. In addition, it was revealed that the irradiation caused a decrease in the number of low-energy SE (~ 3 eV) emissions, and reduced the contrast in unfiltered SE images. Consequently, the irradiation-induced mechanism causing a decrease in the low-energy SE emissions was discussed, and a surface charging model was suggested. This model was confirmed by analysis of the SE energy distributions and experiments on the charge neutralization. Thus, it was expected that high-pass energy-filtered imaging that detected SEs with energies of over 3 eV was effective in reducing the influence of the electron beam irradiation. In fact, we applied this energy-filtering and confirmed that the unfavorable influence of the electron beam irradiation was reduced substantially. We also confirmed that the dopant contrast was clearly observed even after continuous SEM observation. Thus, highly reproducible dopant profiling was achieved.

The third problem was contrast interpretation of the heterojunction interfaces. SEM contrast arises not only from the dopant concentration, but also from the potential change at the heterojunctions. Therefore, the interpretation of SEM contrast in compound semiconductor devices is more complicated than for silicon devices. For accurate 2D dopant profiling of compound devices, it is essential that the influence of the heterojunction on the SEM contrast be taken into account, and that the dependence of the SEM contrast on the dopant concentration at the interface is clearly determined. Based on SEM observations and potential calculation results using SIMS measurements, the dependence of the SEM contrast on the Zn diffusion length across the p^+ -InP/undoped n^- -InGaAs interface was investigated. It was revealed that accurate dopant profiling was difficult when the Zn diffusion length was less than 30 nm, due to the influence of the heterojunction. In contrast, accurate dopant profiling was possible when

the Zn diffusion length was greater than 30 nm, because the dominant factor of the electrostatic potential variation was not the heterojunction, but rather Zn diffusion 30 nm from the interface. Although we analyzed a p⁺-InP/n⁻-InGaAs interface in this study, this method that incorporates the influence of the heterojunction on the SEM contrast can be applied to any interface. Thus, SE imaging with potential calculations can be widely used for accurate dopant profiling, even at heterojunctions.

The dopant contrast mechanism, which remains unclear, was discussed using the obtained experimental results. The ion-milling experiments conducted in this study yielded two results. One was that dopant contrast decreased as the thickness of the amorphous layer, which canceled out the built-in potential, was increased. The other was that, as the penetration depth of the primary electron beam increased, the dopant contrast was also increased in a sample with a thick amorphous layer. These results indicate that the contrast primarily arises from the external or internal electric field of the sample. Experiments on energy-filtered imaging showed that positive charging of the surface decreased dopant contrast. These results indicate that surface charging strongly affects the contrast. Further, a comparison of the SEM observation, SIMS, and potential calculation revealed the insensitivity of SEM to the n-type region. In order to explain this result, a new model was suggested in which the contrast depends on not only the potential, but also the carrier concentration.

In conclusion, this thesis examined the three major problems impeding the application of the 2D dopant profiling technique using SEM. It was demonstrated that the decrease in dopant contrast was caused by the generation of an amorphous layer due to the sample preparation method. This problem was solved using low-energy Ar⁺ ion milling. It was also determined that the low reproducibility induced by the electron beam irradiation for the SEM imaging was caused by surface charging. This issue was addressed using energy-filtered imaging. Finally, the SEM contrast interpretation problem across an interface was clearly understood using potential calculations.

Thus, the three major problems hindering the practical use of 2D dopant profiling using SEM were addressed. The successfully established

profiling technique is expected to be practically used, making a significant contribution to the compound semiconductor device industry.

6.2 Remaining issues

As described above, 2D dopant profiling of compound semiconductor devices using SEM has reached the level required for industrial use. However, there are two remaining issues.

The first is that the dopant contrast mechanism has not yet been completely determined. As described in this thesis, the fundamental mechanism has been only partially identified, and a detailed mechanism involving the insensitivity to the n-type regions, the contrast reversal due to a thick oxide layer, etc., must be fully explored both experimentally and theoretically.

The second issue is that the sensitivity and spatial resolution must be improved in order to prepare for future demand. The sensitivity and spatial resolution of SEM are now approximately 10^{16} atoms/cm³ and 10 nm respectively, and this is currently regarded as sufficient. However, high sensitivity and resolution, for example 10^{15} atoms/cm³ and 1 nm, will be required for higher device performance and reliability in the near future. In these cases, CL, SSRM, or electron holography should be used, although these methods have not been established as techniques for compound semiconductor device measurement for industrial use. It is therefore difficult to evaluate their efficacy.

Thus, the development of a 2D dopant profiling method with high sensitivity and spatial resolution will be required. As mentioned above, the mechanism behind 2D dopant profiling using SEM is still unclear. Determining the profiling mechanism may provide an appropriate measurement method and, therefore, may improve the sensitivity and spatial resolution. The development of such a 2D dopant profiling method would contribute to the compound semiconductor industry.

List of symbols and abbreviations

This list does not cover all the symbols and abbreviations that appear in the thesis, but is limited to frequently-used ones.

Symbols

E_v	valence band
E_{vac}	local vacuum level
E_{SEM}	relative energy of an electron as far as the SEM chamber walls or detector
E_p, E_n	ionization energy of a p-type or n-type region
V_c	control electrode voltage
V_r	reverse bias voltage
I_p, I_n	intensities from a p-type or n-type layer
C_{pn}	quantified dopant contrast

Abbreviations

AES	Auger Electron Spectroscopy
BSE	Back Scattered Electron
CAGR	Compound Annual Growth Rate
CIS	Cryo Ion Slicer (JEOL IB-09060CIS)
CL	Cathode Luminescence
E-T Detector	Everhart-Thornley Detector
FE-SEM	Field Emission SEM
FIB	Focused Ion Beam
InP	Indium Phosphide
IP	Ion Polishing

LD	Laser Diode
LED	Light Emitting Diode
MOVPE	Metal-Organic Vapor Phase Epitaxy
PD	Photo Diode
RF	Radio Frequency
SE	Secondary Electron
SEM	Scanning Electron Microscopy
SIMS	Secondary Ion Mass Spectrometry
SPM	Scanning Probe Microscopy
SSRM	Scanning Spread Resistance Microscopy
TEM	Transmission Electron Microscopy
TTL Detector	Through-The-Lens Detector

Publications

Publications related to this research

- [1] D. Tsurumi and K. Hamada, “Sensitive Site-Specific Dopant Mapping in Scanning Electron Microscopy on Specimens Prepared by Low Energy Ar⁺ Ion Milling,” *Appl. Phys. Express*, vol. 6, no. 12, 126601, 2013.
- [2] D. Tsurumi, K. Hamada, and Y. Kawasaki, “Observation of two-dimensional p-type dopant diffusion across a p⁺-InP/n⁻-InGaAs interface using scanning electron microscopy,” *J. Appl. Phys.*, vol. 113, no. 14, 144901, 2013.
- [3] D. Tsurumi, K. Hamada, and Y. Kawasaki, “Energy-Filtered Secondary-Electron Imaging for Nanoscale Dopant Mapping by Applying a Reverse Bias Voltage,” *Jpn. J. Appl. Phys.*, vol. 51, no. 10R, 106503, 2012.
- [4] D. Tsurumi, K. Hamada, and Y. Kawasaki, “Highly Reproducible Secondary Electron Imaging under Electron Irradiation Using High-Pass Energy Filtering in Low-Voltage Scanning Electron Microscopy,” *Microsc. Microanal.*, vol. 18, no. 02, pp. 385–389, 2012.
- [5] D. Tsurumi, K. Hamada, and Y. Kawasaki, “Energy-filtered imaging in a scanning electron microscope for dopant contrast in InP.,” *J. Electron Microsc. (Tokyo)*, vol. 59 Suppl 1, pp. S183–S187, 2010.

The other publications

- [1] D. Tsurumi and K. Hamada, "Dopant Mapping of Semiconductors with Scanning Electron Microscopy," SEI Tech. Rev., vol. 1, no. 77, pp. 141-146, 2013.
- [2] D. Tsurumi, K. M. Itoh, and H. Yamada-Kaneta, "Host-isotope effect on the localized vibrational modes of oxygen dimer in isotopically enriched silicon," Physica B Condens. Matter, vol. 376-377, pp. 959-962, 2006.

Conferences related to this research

- [1] D. Tsurumi and K. Hamada, "The effect of low energy Ar⁺ ion milling using a cold stage on InP in SEM" The 69th Annual Meeting of the Japanese Society of Microscopy, M7-A21am04, 2013. (In Japanese)
- [2] D. Tsurumi, K. Hamada, and Y. Kawasaki, "Observation of Dopant Diffusion across a p-InP/i-InGaAs Interface using SEM" The 68th Annual Meeting of the Japanese Society of Microscopy, P-I-11, 2012. (In Japanese)
- [3] D. Tsurumi, K. Hamada, and Y. Kawasaki, "Energy-Filtered Secondary-Electron Imaging for Nanoscale Dopant Mapping by Applying a Reverse Bias Voltage", The 13th Frontiers of Electron Microscopy in Materials Science, Tuesday PM ~ Poster Session 2 no.24, California, 2011.

- [4] D. Tsurumi, K. Hamada, and Y. Kawasaki, "High resolution secondary electron imaging for dopant mapping using bias voltage" The 67th Annual Meeting of the Japanese Society of Microscopy, 16Dpm_S5-8, 2011. (In Japanese)

- [5] D. Tsurumi, K. Hamada, and Y. Kawasaki, "Observation of Dopant Diffusion across a p-InP/i-MQW Interface using Secondary Electron Spectra and Scanning Electron Microscopy" The 6th International Workshop on Nano-scale Spectroscopy and Nanotechnology, Kobe, 2010.

- [6] D. Tsurumi, K. Hamada, and Y. Kawasaki, "Dopant Diffusion Observation across a p-InP/i-MQW Interface using Scanning Electron Microscopy" The 66th Annual Meeting of the Japanese Society of Microscopy, P-I20, 2010. (In Japanese)

- [7] D. Tsurumi, K. Hamada, and Y. Kawasaki, "Energy-filtered Imaging in a Scanning Electron Microscope for Dopant Contrast in InP", The 12th Frontiers of Electron Microscopy in Materials Science, Sasebo, P-113, 2009.

- [8] D. Tsurumi, K. Hamada, and Y. Kawasaki, "Dopant Contrast Observation in InP using Energy-filtered Imaging in a Scanning Electron Microscope" The 65th Annual Meeting of the Japanese Society of Microscopy, P-I25, 2009. (In Japanese)

The other conference

- [1] D. Tsurumi, K. M. Itoh, and H. Yamada-Kaneta, "Host-isotope effect on the localized vibrational modes of oxygen dimer in isotopically enriched silicon", The 23rd International Conference on Defects in Semiconductors, Hyogo, ThP.107, 2005.